Available online at www.sciencedirect.com
ScienceDirect
Comput. Methods Appl. Mech. Engrg. 341 (2018) 740–787
Computer methods in applied mechanics and engineering
www.elsevier.com/locate/cma

Multi-scale modelling of arterial tissue: Linking networks of fibres to continua

Felipe Figueredo Rocha[a,b,*], Pablo Javier Blanco[a,b], Pablo Javier Sánchez[c,d], Raúl Antonino Feijóo[a,b]

[a] *Laboratório Nacional de Computação Científica, Av. Getúlio Vargas 333, Quitandinha, 25651-075 Petrópolis, Brazil*
[b] *Instituto Nacional de Ciência e Tecnologia em Medicina Assistida por Computação Científica, Petrópolis, Brazil*
[c] *CIMEC-UNL-CONICET, Colectora RN 168, Km 472, Paraje el Pozo, CP 3000, Santa Fe, Argentina*
[d] *GIMNI-UTN-FRSF, Lavaise 610, CP 3000, Santa Fe, Argentina*

Received 20 March 2018; received in revised form 17 June 2018; accepted 18 June 2018
Available online 18 July 2018

Abstract

In this work we develop a multi-scale model to characterise the large scale constitutive behaviour of a material featuring a small scale fibrous architecture. The Method of Multi-scale Virtual Power (MMVP) is employed to construct the model. At the macro-scale, a classical continuum mechanics problem is formulated in the finite strain regime. At the micro-scale, a network of fibres, modelled as one-dimensional continua, composes the representative volume element (RVE). The MMVP provides a full characterisation of the equilibrium problem at the RVE, with consistent boundary conditions, as well as the homogenisation formula which defines the first Piola–Kirchhoff stress tensor. Particular attention is given to the fact that the macro-scale continuum could be considered incompressible. Numerical experiments are presented and model consistency is verified against well-known phenomenological constitutive equations. Scenarios departing from the hypotheses of such phenomenological material models are discussed.

Keywords: Multi-scale modelling; Fibre network; Representative volume element; Biological tissues; Virtual power; Non-affinity

1. Introduction

Constitutive modelling of arterial tissue is a core subject towards the rational modelling of complex mechanical processes related to the onset and progress of some cardiovascular diseases. For this reason, in the last decades, several constitutive models have been proposed in the attempt to improve predictive capabilities to model the material behaviour of arterial tissue [1–4].

Arterial tissue features a natural multi-scale character in which the large scale (or macro-scale) observable behaviour is the result of complex mechanical interactions occurring at the level of the material constituents. Arteries

* Corresponding author at: Laboratório Nacional de Computação Científica, Av. Getúlio Vargas 333, Quitandinha, 25651-075 Petrópolis, Brazil.
E-mail address: felipefr@lncc.br (F.F. Rocha).

https://doi.org/10.1016/j.cma.2018.06.031
0045-7825/

are generally multi-layered and multi-component materials, whose basic unit blocks are elastin, collagen fibres and smooth muscle cells. The modelling of such interactions is usually accomplished by using phenomenological models, which require large number of material parameters and internal variables to describe increasingly intricate mechanical processes. Naturally, such model parameters are difficult to characterise through experiments.

Within the characterisation of the arterial tissue, the mechanical relevance of the tunica media and adventitia is of the utmost interest. These layers feature an architecture of elastic and collagen fibres which provide them with particular functional roles [5]. The exact composition depends on the type of vessel and, also, on the size of the vessel. However, the fibrous structure is dominant for these two outer layers. From a macro-scale viewpoint, these fibres display a certain preferred material orientation around a given direction which, also, depends on the type of vessel. Thus, phenomenological models have introduced the effect of fibres through transversely isotropic constitutive functionals based on direction-dependent invariants also including the effect of fibre dispersion [2,4].

A natural approach to overcome the drawbacks inherent to phenomenological models is the explicit modelling of the mechanical interactions between basic constituents of the tissues, through a multi-scale strategy based on the Representative Volume Element (RVE) concept.

More specifically, in the context of biological materials displaying a fibrous structure, some works have addressed the importance of the mechanical interaction among fibres at the micro-scale in the overall response of the tissue. For example, as pointed in [6], the effect of stiffening is not well understood, and considering the non-affinity of deformation in those models is necessary to gain insight into such phenomenon. In [7,8], the authors attributed the nonlinear mechanical response observed in some experimental tests to two contributing factors: (i) the individual nonlinear constitutive behaviour of each single fibre, and (ii) the non-affine collective deformation of the network. Several non-affinity indexes are proposed and comparison made in [9]. In [10], the same factors are discussed, plus the recruitment of individual fibres, which is also claimed to play an important role in the nonlinear behaviour observed at the macro-scale. All these factors motivate the construction of multi-scale models, so that the internal structure of the tissue along with underlying micro-mechanical interactions are taken into account in the resulting material response.

Up to the authors' knowledge, very few works considered multi-scale methodologies to model the material response of a network of fibres in biological tissues. For instance, the work of Speirs et al. [11] aimed at fitting parameters of some classical strain energy functions by means of homogenisation and optimisation of a multi-scale model composed by a continuum matrix of material (representing the elastin content) reinforced with a set of discrete trusses elements representing the collagen fibres. However, and because of the existence of a background continuum elastin matrix, this multi-scale approach was entirely based on standard continuum mechanics methods, and no reference to the discrete nature of the fibres network was made.

In the works by Chandran and Barocas [8], Stylianopoulos and Barocas [12,13] the so-called collagen hyperelastic network approach is presented and applied in the multi-scale analysis of the arterial tissue. These works postulate the homogenisation for the stress measure based on a continuum-like homogenisation procedure, but no detailed discussion about the connection of kinematical descriptors between scales, as well as boundary conditions other than the linear boundary displacement constraint is mentioned. Following a similar approach, although relying on an infinitesimal strain model for individual collagen fibres and also suffering from the same drawbacks than works previously cited in this paragraph, the contributions by Thunes et al. [14,15] show interesting predictive capabilities, and considerable advances were achieved towards correlating experimental data of human aorta. Pursuing a different approach, Witthoft et al. [16] makes use of DFD (Dissipative Particle Dynamics) to model multi-constituent arterial tissues.

Dealing with multi-scale methods based on asymptotic analysis and generalised non-Cauchy continuum applied to fibre networks, the recent works of [17–19] present important contributions, the later being in the domain of textiles, and including inter-fibre contact. These works are based on a more general procedure published independently by Caillerie et al. [20] and Warren and Byskov [21], the so-called discrete homogenisation (in short DH). Importantly, the DH method is restricted to periodic conditions.

Concerning size-effects of the RVE, Berkache et al. [17]; Shahsavari and Picu [22] perform convergence analyses of their models and both conclude in favour of the fundamental role played by different boundary conditions in the context of fibre networks. Notwithstanding this, both methodologies fail to provide a clear derivation and interpretation of those boundary conditions. In this direction, the present contribution will considerably expand the understanding on this matter by pursuing a multi-scale approach based on the Hill–Mandel principle.

In a more general context of material modelling using computational mechanics, very few attempts have been made to couple discrete mechanical interactions with continua in a multi-scale setting. We highlight the works of Miehe

and Dettmar [23], Miehe et al. [24], which addressed the homogenisation of a granular micro-structure to retrieve standard measures of internal stresses in the material. Other works regarding the homogenisation of atomistic and molecular dynamics interactions are reported in [25–28] and in the realm of multi-scale modelling of the paper an example is [29].

Based on the above considerations, the aim of the present work is to develop a novel multi-scale model to address the macro-scale constitutive response of biological tissues featuring an underlying fibrous architecture at a smaller scale. The proposed model allows to consistently couple a classical continuum model in the finite strain regime at the macro-scale with a fully discrete model characterised by a network of trusses at micro-scale. To achieve this goal we make use of the Method of Multi-scale Virtual Power (MMVP) developed in [30,31] which provides a well-defined systematic procedure to construct multi-scale models using a minimum set of hypotheses. The MMVP, relies on three steps, namely: (i) the definition of kinematics at each scale, and the proper transfer of kinematical descriptors between scales, (ii) the use of duality arguments to introduce the stress measures as dictated by the virtual power functionals at both scales, and (iii) the formulation of the Principle of Multi-scale Virtual Power (PMVP), which ensures the physical consistency between scales.

Concerning the boundary conditions of the micro-scale problem, it is important to emphasise that its choice strongly affects the homogenised mechanical response, especially for small micro-scale domains whose representativeness may be debatable. Therefore, a proper kinematical cross-talk between micro-scale and macro-scale becomes mandatory when one looks to derive kinematical constraints that consistently yield suitable boundary conditions. Hence, in this work we also provide the minimally constrained space of admissible displacement fields for the micro-scale problem. This is a key aspect in the development and understanding of micro-scale boundary conditions in multi-scale problems, since this provides the ground for the specification of other more constrained sub-models frequently found in literature. Finally, it is also shown that the reactive generalised force caused by the kinematical restriction characterising the minimally constrained space is related to the homogenised stress, which is obtained by a homogenisation rule also (naturally) revealed by the proposed variational formulation.

The hypothesis of an incompressible macro-scale continuum, which is a standard assumption adopted in the modelling of biological tissues, is also addressed in parallel to the developments. This unified treatment naturally extends the present theory to deal with both compressible and incompressible macro-scale media.

The present work is organised as follows. In Section 2 we overview some features of the proposed multi-scale model. Section 3 presents the model considered at the macro-scale, for which a closure constitutive equation is sought using the proposed multi-scale approach. The multi-scale constitutive model is developed in three parts, presented in Section 4 (kinematics), Section 5 (duality) and Section 6 (PMVP). Some theoretical aspects of the present multi-scale model are discussed in Section 7, particularly those related to the mechanical significance of the generalised forces associated to the kinematical restrictions. Section 8 is devoted to the constitutive modelling of fibres at the micro-scale, and numerical tests are presented in Section 9. Extensions to the present model and limitations are discussed in Section 10. Final remarks are outlined in Section 11. Furthermore, the reader interested in a more detailed continuum flavour of the discrete model used at the micro-scale is directed to Appendix A. Finally, some complementary proofs and properties can be found in Appendix B. Throughout the manuscript, an informative parallel with continuum multi-scale formulations is discussed in a series of remarks termed “(Continuum Case)”. The same strategy of remarks is applied when referring to the macro-scale incompressibility hypothesis, these termed “(Incompressible Case)”.

2. Overview of the multi-scale model

In this section we introduce the main hypotheses for the micro-scale model and provide a brief review of the Method of Multiscale Virtual Power (MMVP) [30].

2.1. Main features of the model for fibres network

The present model aims to simulate the constitutive behaviour of biological tissues with an underlying fibrous architecture, with special emphasis in arterial tissues for which the network of collagen fibres is the structural element.

The fibres are very slender components, and therefore their behaviour is considered through one-dimensional structural components. The basic hypotheses about the network of fibres are the following:

- The network of fibres is an interconnected network of nonlinear rectilinear trusses. Therefore, bending, shear and torsional effects in the fibres are neglected.

- Fibres are connected through perfect joints which neither detach nor offer resistance to the relative change of direction of the fibres.
- Body forces per unit volume are neglected in the network.
- No matrix is considered as ground substance for the network, then the fibres are surrounded by "empty space".

Remark 1. For all purpose of this work, as "empty space" we consider a medium which is mechanically irrelevant. For instance, in the case of a fluid surrounding the fibres, if dissipative effects are disregarded, the contribution in stress state would be irrelevant, however it could add a kinematical constraint to the overall behaviour of the material, turning the tissue into an incompressible medium. Incompressibility is addressed in a series of remarks throughout the manuscript.

Remark 2. Other constituents of arterial tissue such as elastin fibres and smooth muscle cells could also be coupled with the present multi-scale model, but their incorporation in the present model is out of the scope of this work.

These hypotheses are physically reasonable and have been already proposed in literature (see for example [12,13]). Particularly, with respect to the interconnected network structure, in [32] it is argued that isolated fibres tend to spontaneously cross-link in order to stabilise the structure.

Networks of fibres can be artificially generated using specific algorithms. Previous works used Voronoi [33] and Delaunay [34] tessellations, as well as the so-called Mikado networks [35], which are randomly generated straight lines with cross-links identified at each crossing of lines. Another alternative algorithm for network generation, similar to Mikado networks, was presented in [12], but in such case, instead of line segments, the nodes are primarily generated randomly. One may also want to consider the segmentation of real microscopic images as in [36].

Concerning the individual fibres, we take the following assumptions:

- Each single fibre is a straight segment[1] with uniform cross-sectional area, material properties and strain.
- Fibres only support tensile stress in axial direction, or even they just may be activated after exceeding a certain stretch, called *activation stretch*.
- A fibre features a hyperelastic behaviour inspired in phenomenological models.

These hypotheses are considered for the sake of simplicity, but do not impose serious limitations to the formulation of the proposed multi-scale model, which is the main focus of our work. Again, analogous assumptions were already regarded in previous works [12,13].

For those readers interested in a more sophisticated model in terms of fibre kinematics, we refer to recent works including the geometrically exact beam theory accounting different kinds of contacts between fibres [37,38].

2.2. Method of Multiscale Virtual Power (MMVP)

The multi-scale model is constructed using the MMVP developed in [30]. This approach was adopted because it is a general methodology that, following well-defined steps, allows to construct new multi-scale models based on a minimum set of assumptions. The MMVP has been successfully applied in a number of different multi-scale problems such as the analysis of solid mechanics with micro-scale inertial effects [39]; in the connection between second order continua and classical continuum mechanics models [40], in fluid mechanics [41], thermoelasticity [42] and also to tackle multi-scale material failure [43–46].

The derivation of a multi-scale model using the MMVP is based on three fundamental concepts described next.

1. *Kinematical Admissibility*. The kinematics for both macro- and micro-scales must be first defined, which amounts to define the kinematical descriptors at each scale together with the *generalised gradient* operators. Connection between the scales is established through (i) the *insertion* of macro-scale entities into the micro-scale kinematics and (ii) the *homogenisation* of micro-scale entities to render corresponding macro-scale kinematical descriptors. The macro-scale and the micro-scale kinematics, and the connection between them in terms of insertion and homogenisation operations are developed in detail in Section 4. Moreover, the role of the homogenisation operations is to provide an unambiguous set of rules to define constraints for the kinematical descriptors at the micro-scale, avoiding thus ad-hoc considerations.

[1] The physical effect of waviness will be considered in the constitutive law for each fibre but not in its geometrical description.

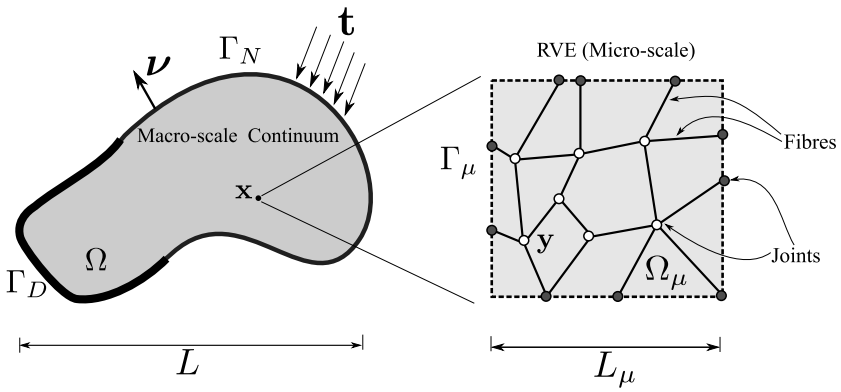

Fig. 1. Macro-scale continuum and discrete micro-scale RVE domains.

2. *Mathematical Duality*. The postulation of the virtual power functionals for each scale is the second step. This amounts to characterise, as power-conjugates to kinematical descriptors, the dual force- and stress-like entities. These entities are thus compatible with the kinematics in each scale. The macro- and micro-scale virtual power functionals, which play a key role in the multi-scale power balance, are introduced in Section 5.
3. *Principle of Multiscale Virtual Power* (PMVP). This principle consists in a variational statement and generalisation of the Hill–Mandel Principle of Macrohomogeneity [47,48], where the postulated virtual power functionals defined in the different scales are equated. From this principle, the micro-scale equilibrium problem and the homogenisation formula for the stress measure are derived using variational arguments. The PMVP is developed in Section 6.

The present contribution takes advantage of the possibility offered by the MMVP to deal with macro- and micro-mechanical models featuring different kinematics. While the macro-scale solid kinematics is modelled using a standard continuum approach in the finite strain regime, the micro-scale mechanics is modelled using a discrete kinematics. In this sense, and in the context of applications of the MMVP, the present work is also novel and can be used to drive the construction of multiscale models with similar features in other applications.

3. Macro-scale model

At the macro-scale we consider a standard model from continuum mechanics in the finite strain regime. Let $\Omega \subset \mathbb{R}^{n_d}$, $n_d = 2,3$, be an open set which represents the reference (or material) configuration of the body $\mathcal{B}$. At each material point $\mathbf{x} \in \Omega$ we introduce the displacement vector field $\mathbf{u} : \Omega \to \mathbb{R}^{n_d}$ and the associated first material gradient tensor field $\mathbf{G} := \nabla \mathbf{u} : \Omega \to \mathbb{R}^{n_d \times n_d}$. The boundary of Ω is denoted by Γ, whose outward unit normal vector is $\boldsymbol{\nu}$, and is split in Neumann (Γ_N) and Dirichlet (Γ_D) parts. This setting is depicted in Fig. 1 (left) and the mechanical equilibrium is established by the following variational formulation.

Problem 1 (*Macro-Scale Mechanical Problem*)**.** Given the traction vector $\mathbf{t}$ defined over Γ_N, find the displacement field $\mathbf{u} \in \mathscr{U}$ such that the stress tensor $\mathbf{P}$ is such that the following variational equation is satisfied

$$\int_\Omega \mathbf{P} \cdot \nabla \hat{\mathbf{u}} \, d\Omega - \int_{\Gamma_N} \mathbf{t} \cdot \hat{\mathbf{u}} \, d\Gamma_N = 0 \quad \forall \hat{\mathbf{u}} \in \mathscr{V}, \tag{1}$$

where the set of kinematically admissible displacement fields is

$$\mathscr{U} = \{\mathbf{u} \in [H^1(\Omega)]^{n_d};\ \mathbf{u}|_{\Gamma_D} = \mathbf{u}_D\}, \tag{2}$$

the corresponding space of kinematically admissible virtual displacements is

$$\mathscr{V} = \{\hat{\mathbf{u}} \in [H^1(\Omega)]^{n_d};\ \hat{\mathbf{u}}|_{\Gamma_D} = \mathbf{0}\}, \tag{3}$$

and the stress tensor, the so-called first Piola–Kirchhoff tensor, is given by $\mathbf{P} = \mathscr{F}(\mathbf{G})$,[2] with $\mathscr{F}(\cdot)$ being a known constitutive functional.

In a multi-scale approach, the constitutive functional $\mathscr{F}$ is implicitly defined by solving a micro-scale problem (in the RVE) and by applying a certain homogenisation procedure to entities defined at the micro-scale level. The full characterisation of this constitutive multi-scale functional for fibrous tissues is the main goal of the present work and is addressed in forthcoming sections.

Remark 3 (*Incompressible Case*)**.** In the case of an incompressible macro-scale model, the set of kinematically admissible displacement fields is

$$\mathscr{U}_{\mathsf{inc}} = \{\mathbf{u} \in \mathscr{U};\, \det(\mathbf{I} + \nabla\mathbf{u}) = 1 \text{ in } \Omega\}, \tag{4}$$

and the associated space of admissible virtual displacements becomes

$$\begin{aligned}\mathscr{V}_{\mathsf{inc}} &= \{\hat{\mathbf{u}} \in \mathscr{V};\, (\mathbf{I} + \nabla\mathbf{u})^{-T} \cdot \nabla\hat{\mathbf{u}} = 0 \text{ in } \Omega\} \\ &= \{\hat{\mathbf{u}} \in \mathscr{V};\, \mathrm{tr}\left(\nabla\hat{\mathbf{u}}\,(\mathbf{I} + \nabla\mathbf{u})^{-1}\right) = 0 \text{ in } \Omega\}\end{aligned} \tag{5}$$

where $\mathrm{tr}(\cdot)$ denotes the trace of the second order tensor $(\cdot)$. Accordingly, the variational formulation in Problem 1 needs to be slightly changed by switching $\mathscr{U}$ and $\mathscr{V}$ to $\mathscr{U}_{\mathsf{inc}}$ and $\mathscr{V}_{\mathsf{inc}}$, respectively. Moreover, the constitutive law $\mathscr{F}$ only provides the isochoric (or deviatoric)[3] part of the stress, namely $\mathbf{P}^{\mathsf{iso}}$, in both the single- and multi-scale approaches.

4. Multi-scale kinematics

4.1. Preliminaries

In this section we present the micro-scale kinematical setting for the network of fibres and its connection to the macro-scale kinematics within the framework of the MMVP, which is illustrated in Fig. 1. For each macro-scale point $\mathbf{x} \in \Omega$ we associate a micro-scale domain $\Omega_\mu \subset \mathbb{R}^{\mathsf{n_d}}$ (also described in a reference configuration), which is called Representative Volume Element (RVE). It is considered that the characteristic lengths are $L_\mu/L \ll 1$, where L and L_μ are characteristic lengths related to the macro-scale and micro-scale, respectively. The RVE size L_μ is chosen such that Ω_μ is a representative piece of the material in terms of constituent elements. Coordinates in the micro-scale domain Ω_μ are denoted by $\mathbf{y}$. Entities associated to the RVE will be denoted by index μ. In turn, entities point-valued at coordinate $\mathbf{x} \in \Omega$ in the macro-scale are denoted by $(\cdot)|_{\mathbf{x}}$. Using this notation, kinematical descriptors of macro-scale are denoted by $\mathbf{u}|_{\mathbf{x}}$ and $\mathbf{G}|_{\mathbf{x}}$, which are elements from the finite-dimensional spaces $\mathbb{R}^{\mathsf{n_d}}$ and $\mathbb{R}^{\mathsf{n_d}\times\mathsf{n_d}}$, respectively. Also, admissible variations $\hat{\mathbf{u}}|_{\mathbf{x}}$ and $\hat{\mathbf{G}}|_{\mathbf{x}}$ belong to $\mathbb{R}^{\mathsf{n_d}}$ and $\mathbb{R}^{\mathsf{n_d}\times\mathsf{n_d}}$ respectively.[4] Finally, Section 4.2 is devoted to present the discrete structure that partially fills the volume Ω_μ.

4.2. Characterisation of micro-scale fibre network

Before providing the specific description of the micro-scale kinematics, in this section we introduce some basic notations. As already commented, our micro-scale network model consists of interconnected straight trusses, which models the real fibrous structure at the micro-scale. Each truss is an idealisation of a collagen bundle (a group of collagen fibres in the present context) and is geometrically represented by a line segment between two points. As an abuse of notation, when referring to a truss we simply call it *fibre*. For more considerations and its constitutive implications, see Section 8.

The other object that has to be modelled in the network is the joint that interconnects fibre segments, which represents the interaction between two or more bundle of collagen fibres crossing each other. In this work, there is no relative displacement among the fibres reaching the joint. Moreover, as the characteristic size of a joint is much smaller than that of fibres, we idealise these entities as *nodes* (or simply points), that is, geometrical entities without dimension.

[2] Equivalently this could be formulated in terms of deformation gradient $\mathbf{F} := \mathbf{I} + \mathbf{G}$.

[3] By isochoric (or deviatoric) part of the first Piola–Kirchhoff stress tensor we mean that the trace of the corresponding Cauchy stress is zero. The classical transformation between Piola–Kirchhoff and Cauchy stress tensors is recalled later in Remark 19.

[4] As seen in Remark 3 for incompressible case, $\mathbf{G}|_{\mathbf{x}}$ and $\hat{\mathbf{G}}|_{\mathbf{x}}$ are not free in $\mathbb{R}^{\mathsf{n_d}\times\mathsf{n_d}}$. We will return to this discussion in Remark 18.

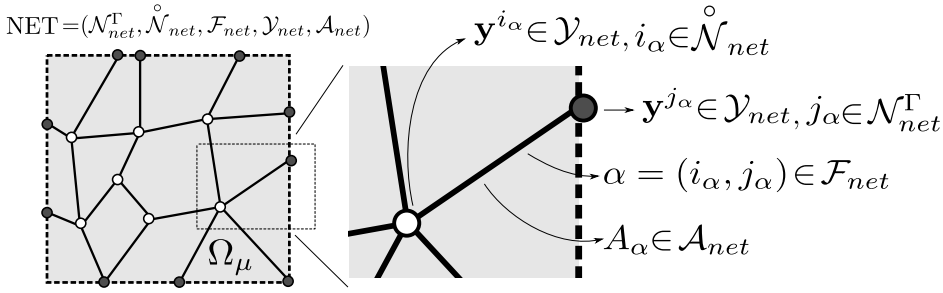

Fig. 2. Notation and basic ingredients in the geometrical/topological description of the *Network* of fibres.

Next, the kinematical framework for the components at micro-scale in a pure discrete form is presented. For the interested reader, the justifications for this model from a continuum perspective can be found in Appendix A.2.

To denote the set of fibres which are interconnected through nodes we introduce the following notation

$$\begin{aligned}\mathcal{N}_{net} &= \text{list of nodes in the network}\\ &= \{i;\ i = 1\ldots, n\},\end{aligned} \tag{6}$$

$$\begin{aligned}\mathcal{F}_{net} &= \text{list of fibres in the network}\\ &= \{\alpha = (i_\alpha, j_\alpha) \in \mathcal{N}_{net} \times \mathcal{N}_{net};\ i_\alpha \neq j_\alpha\},\end{aligned} \tag{7}$$

where i_α and j_α stand for initial and final node of fibre α, respectively.

To complement the geometrical characterisation of the oriented graph $(\mathcal{N}_{net}, \mathcal{F}_{net})$, we introduce the following sets

$$\mathcal{N}_{net}^{\Gamma} = \text{boundary nodes in the network } (\mathcal{N}_{net}^{\Gamma} \subset \mathcal{N}_{net}), \tag{8}$$

$$\mathring{\mathcal{N}}_{net} = \text{interior nodes in the network} = \mathcal{N}_{net} \setminus \mathcal{N}_{net}^{\Gamma}, \tag{9}$$

$$\mathcal{Y}_{net} = \text{node positions} = \{\mathbf{y}^i \in \Omega_\mu,\ i \in \mathcal{N}_{net}\}, \tag{10}$$

$$\mathcal{A}_{net} = \text{fibre transversal areas} = \{A_\alpha \in \mathbb{R}^+,\ \alpha \in \mathcal{F}_{net}\}. \tag{11}$$

Then, the representation of the network of fibres is fully characterised by the following object

$$\text{NET} = (\mathcal{N}_{net}^{\Gamma}, \mathring{\mathcal{N}}_{net}, \mathcal{F}_{net}, \mathcal{Y}_{net}, \mathcal{A}_{net}), \tag{12}$$

which for brevity is simply called *Network*, and whose basic elements are schematically shown in Fig. 2. Note that $\mathcal{N}_{net}$ is already implicit in (12) since $\mathcal{N}_{net} = \mathcal{N}_{net}^{\Gamma} \cup \mathring{\mathcal{N}}_{net}$.

It is worth mentioning that the property $\mathcal{A}_{net}$ equips the one-dimensional discrete model with a realistic three-dimensional structure of the continuum model, which is further complemented by the *activation stretch* that is related to the tortuosity of the real fibre. This will be taken into account later in Section 8 when addressing the constitutive behaviour of the fibres.

Consider now the length of fibre α given by

$$L_\alpha = \|\mathbf{y}^{j_\alpha} - \mathbf{y}^{i_\alpha}\|_2, \tag{13}$$

where $\|\cdot\|_2$ is the standard Euclidean norm in $\mathbb{R}^{n_d}$. Let us define the volume of the fibre V_α and the measure of the whole set of fibres $|\mathcal{F}_{net}|$ as follows

$$V_\alpha = A_\alpha L_\alpha, \quad \alpha \in \mathcal{F}_{net}, \tag{14}$$

$$|\mathcal{F}_{net}| = \sum_{\alpha \in \mathcal{F}_{net}} V_\alpha. \tag{15}$$

The difference between any generic variable related to extreme points of fibre α, that is, $(\cdot)^{j_\alpha} - (\cdot)^{i_\alpha}$, is denoted by the following operator

$$\Delta^\alpha(\cdot) := (\cdot)^{j_\alpha} - (\cdot)^{i_\alpha}. \tag{16}$$

In addition, we introduce the *fibre-node signal brackets* $[\cdot,\cdot]$ defined by

$$[\alpha, i] = \begin{cases} 1 & \text{if } j_\alpha = i, \\ -1 & \text{if } i_\alpha = i, \\ 0 & \text{otherwise.} \end{cases} \tag{17}$$

This operation contains the same information as the standard fibre (mesh) connectivity data structure, being an alternative way to describe it, but significantly simplifies the derivations in this work. Note that $[\alpha, i]$ is different from zero only when α is in the set

$$\begin{aligned} \mathcal{F}^i_{net} &= \text{fibres sharing node } i \\ &= \{\alpha = (i_\alpha, j_\alpha) \in \mathcal{F}_{net},\ i_\alpha = i \text{ or } j_\alpha = i\}. \end{aligned} \tag{18}$$

Operator Δ^α can be expressed in terms of the *fibre-node signal brackets* as follows

$$\Delta^\alpha(\cdot) = \sum_{i \in \mathcal{N}_{net}} [\alpha, i](\cdot)^i. \tag{19}$$

Also, we introduce the unit vector $\mathbf{a}^\alpha$ defined by fibre α and directed from the initial node i_α to the final node j_α, that is

$$\mathbf{a}^\alpha = \frac{1}{L_\alpha} \Delta^\alpha \mathbf{y}. \tag{20}$$

Associated to each node $i \in \mathcal{N}^\Gamma_{net}$, lying over the boundary of the RVE, we have the *node boundary area(s)* $\bar{A}_{i,k}$ and the *node boundary normal vector(s)* $\mathbf{n}_{i,k}$, where $k \in \{1, \ldots, k_i^{max}\}$, being k_i^{max} the number of RVE faces sharing node i. For example, for a two-dimensional squared RVE as in Fig. 2, for a node $i \in \mathcal{N}^\Gamma_{net}$ over a RVE corner corresponds $k_i^{max} = 2$, otherwise it is $k_i^{max} = 1$. In a three-dimensional cubic RVE, k_i^{max} may assume the values of 3 (at vertices), 2 (on edges) or 1 (over faces).

The area(s) $\bar{A}_{i,k}$ is(are) calculated accounting for the area A_α and direction of fibres $\mathbf{a}^\alpha$ that reach the boundary at a node $i \in \mathcal{N}^\Gamma_{net}$ and its/their respective normal(s) $\mathbf{n}_{i,k}$, which is(are) the corresponding outward unit normal vector(s) to the boundary $\partial\Omega_\mu$, as follows

$$\bar{A}_{i,k} = \sum_{\alpha \in \mathcal{F}^i_{net}} |\mathbf{n}_{i,k} \cdot \mathbf{a}^\alpha| A_\alpha \quad \text{for } i \in \mathcal{N}^\Gamma_{net}, k \in \{1, \ldots, k_i^{max}\}. \tag{21}$$

The geometrical interpretation can be found in Appendix A.2 where typical examples of joints are analysed in Fig. A.25 and equations therein.

To shorten notation let us introduce the *equivalent boundary area* and *normal* for a node over the boundary as

$$\bar{A}_i = \left\| \sum_{k=1}^{k_i^{max}} \bar{A}_{i,k} \mathbf{n}_{i,k} \right\|_2, \tag{22}$$

$$\mathbf{n}_i = \frac{1}{\bar{A}_i} \sum_{k=1}^{k_i^{max}} \bar{A}_{i,k} \mathbf{n}_{i,k}. \tag{23}$$

Now, let us define the *joint normal vector* $\mathbf{m}_i$ for every $i \in \mathcal{N}_{net}$ accounting for the surface integral of the normals for a given joint collapsed into its corresponding node. As explained in Appendix A, the surface considered is the internal solid surface, which means the intersection of the joint and fibres for internal nodes, added to the intersection between joint and RVE borders for boundary nodes. Using definitions (22) and (23) we can define $\mathbf{m}_i$ as:

$$\mathbf{m}_i = \begin{cases} -\displaystyle\sum_{\alpha \in \mathcal{F}^i_{net}} [\alpha, i] A_\alpha \mathbf{a}^\alpha & i \in \overset{\circ}{\mathcal{N}}_{net}, \\ \bar{A}_i \mathbf{n}_i - \displaystyle\sum_{\alpha \in \mathcal{F}^i_{net}} [\alpha, i] A_\alpha \mathbf{a}^\alpha & i \in \mathcal{N}^\Gamma_{net}. \end{cases} \tag{24}$$

Note that the negative sign and fibre-node signal brackets in the definition naturally accommodates the orientation of fibre unit vector to point outwards the joint domain as can be appreciated in Fig. 3.

In the present framework, the discrete structure of NET of an RVE is just admissible when the graph $(\mathcal{N}_{net}, \mathcal{F}_{net})$ is connected, that is, any two nodes of the network are connected by at least one path of fibres.

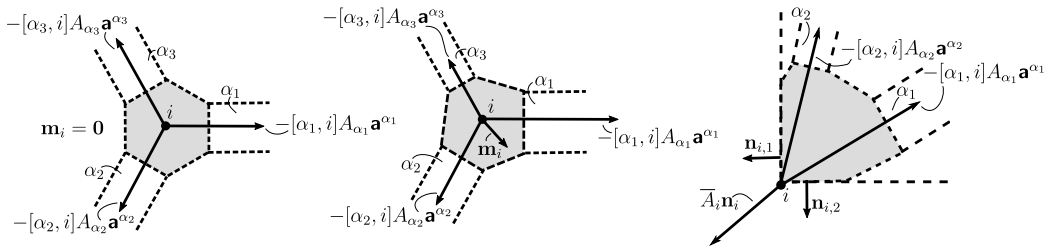

Fig. 3. Concept of joint normal vector in different situations. Left inset: regular hexagonally-shaped joint with $A_{\alpha_1} = A_{\alpha_2} = A_{\alpha_3}$, yielding $\mathbf{m}_i = \mathbf{0}$. Middle inset: arbitrary joint with $A_{\alpha_1} \neq A_{\alpha_2} \neq A_{\alpha_3}$ and so $\mathbf{m}_i \neq \mathbf{0}$. Right inset: Joint at a corner.

Remark 4. In order to facilitate the reading of the manuscript, we adopt different fonts to represent tensorial (including vectors) quantities associated to fibres and nodes, such as $\mathbf{a}^\alpha$ ($\alpha \in \mathcal{F}_{net}$) for fibre and $\mathbf{y}^i$ ($i \in \mathcal{N}_{net}$) for nodes. For n-tuples of tensors we consider Blackboard bold fonts, for example $\mathbb{A} = \{\mathbf{a}^\alpha\}_{\alpha\in\mathcal{F}_{net}}$, generally with the same letter to represent the n-tuple as well as its elements. This kind of notation will be extensively used in the forthcoming sections.

4.3. Micro-scale displacement space

Given a NET we are interested in describing the *displacement* experienced by material points in this *Network*. By material points we have the joints (nodes) and the points that compose the fibres (points of the straight lines).

The displacement at the nodes is an element of the following vector space

$$\mathscr{U}_\mu^N = \{\mathbb{U}_\mu^N = \{\mathbf{u}_\mu^i\}_{i\in\mathcal{N}_{net}};\ \mathbf{u}_\mu^i \in \mathbb{R}^{\mathrm{n_d}},\ i \in \mathcal{N}_{net}\}. \tag{25}$$

It consists of a $|\mathcal{N}_{net}|$-tuple of vectors ($|\mathcal{N}_{net}|$ the cardinality of $\mathcal{N}_{net}$) in the $\mathrm{n_d}$-dimensional space, each vector representing the displacement at each node of the *Network*, thus we denote $\mathbf{u}_\mu^i$ the displacement of node $i \in \mathcal{N}_{net}$.

For a given $\mathbb{U}_\mu^N \in \mathscr{U}_\mu^N$, the fibre displacements fields are in the vector functional space

$$\begin{aligned}\mathscr{U}_\mu^F := \{&\mathbb{U}_\mu^F = \{\mathbf{u}_\mu^\alpha\}_{\alpha\in\mathcal{F}_{net}};\ \mathbf{u}_\mu^\alpha : [0, L_\alpha] \to \mathbb{R}^{\mathrm{n_d}};\\ &\mathbf{u}_\mu^\alpha(s) = \big(1 - \frac{s}{L_\alpha}\big)\mathbf{u}_\mu^{i_\alpha} + \frac{s}{L_\alpha}\mathbf{u}_\mu^{j_\alpha},\ \alpha = (i_\alpha, j_\alpha) \in \mathcal{F}_{net})\},\end{aligned} \tag{26}$$

where the vector field $\mathbf{u}_\mu^\alpha$ associated to each fibre $\alpha \in \mathcal{F}_{net}$ represents the displacement field along the centreline of the fibre in the $\mathrm{n_d}$-dimensional space. Notice that, the space $\mathscr{U}_\mu^F$ is univocally established once $\mathbb{U}_\mu^N \in \mathscr{U}_\mu^N$ is specified. As a consequence, if two fibres share a node, the displacement at such node is the same, which is one of the hypotheses considered in this work.

Therefore, the displacement in the network is completely characterised by the space

$$\mathscr{U}_\mu := \{\mathbb{U}_\mu = (\mathbb{U}_\mu^N, \mathbb{U}_\mu^F) \in \mathscr{U}_\mu^N \times \mathscr{U}_\mu^F\}. \tag{27}$$

The operation of addition in $\mathscr{U}_\mu$ is such that for $\mathbb{W}_1, \mathbb{W}_2 \in \mathscr{U}_\mu$ yields $\mathbb{W}_3 = \mathbb{W}_1 + \mathbb{W}_2 \in \mathscr{U}_\mu$ with

$$\mathbf{w}_3^i = \mathbf{w}_1^i + \mathbf{w}_2^i \qquad \forall i \in \mathcal{N}_{net}, \tag{28}$$

$$\mathbf{w}_3^\alpha(s) = \mathbf{w}_1^\alpha(s) + \mathbf{w}_2^\alpha(s) \qquad \forall \alpha \in \mathcal{F}_{net},\ \forall s \in [0, L_\alpha], \tag{29}$$

where $\mathbb{W}_k = (\{\mathbf{w}_k^i\}_{i\in\mathcal{N}_{net}}, \{\{\mathbf{w}_k^\alpha\}_{\alpha\in\mathcal{F}_{net}}\})$, $k = 1, 2, 3$. The zero element in this space is denoted by $\mathbb{O}$ in such way that $\mathbb{W} + \mathbb{O} = \mathbb{W},\ \forall \mathbb{W} \in \mathscr{U}_\mu$, which means that $\mathbb{O}$ has zero-valued vectors for the nodes part and zero-valued constant vector functions for the fibre part. Analogous interpretation of addition is considered for any other space to be defined in terms of tuples in this manuscript.

Remark 5. From the definition of $\mathscr{U}_\mu^F$ in (26), it is easy to see that the space $\mathscr{U}_\mu$ has the same dimension than $\mathscr{U}_\mu^N$. In other words, an element $\mathbb{U}_\mu \in \mathscr{U}_\mu$ is uniquely determined by a choice of $\mathbb{U}_\mu^N \in \mathscr{U}_\mu^N$. We extensively use this property overall the manuscript by defining quantities exclusively in terms of $\mathbb{U}_\mu^N$.

4.4. Insertion operators

So far, the discrete kinematics groundwork has been established for a network of fibres. Now, it is necessary to define a mapping of the macro-scale kinematics at a given macro-scale point $\mathbf{x}$ into the micro-scale kinematics at the corresponding RVE. This amounts to define the so-called *insertion operators* that map the macro-scale displacement and gradient into the micro-scale description of the displacement. The same concept applies to mapping macro- and micro-scale virtual actions (variations).

The macro-scale displacement at point $\mathbf{x}$ is mapped into the micro-scale kinematics using the following operator

$$\begin{aligned} &\mathcal{J}_\mu^{\mathscr{U}} : \mathbb{R}^{\mathrm{n_d}} \to \mathscr{U}_\mu, \\ &\qquad \mathbf{u}|_{\mathbf{x}} \mapsto \mathcal{J}_\mu^{\mathscr{U}}(\mathbf{u}|_{\mathbf{x}}) = (\mathcal{J}_\mu^{\mathscr{U},N}(\mathbf{u}|_{\mathbf{x}}), \mathcal{J}_\mu^{\mathscr{U},F}(\mathbf{u}|_{\mathbf{x}})), \end{aligned} \tag{30}$$

defined by

$$[\mathcal{J}_\mu^{\mathscr{U},N}(\mathbf{u}|_{\mathbf{x}})]^i = \mathbf{u}|_{\mathbf{x}} \qquad i \in \mathcal{N}_{net}, \tag{31}$$

$$[\mathcal{J}_\mu^{\mathscr{U},F}(\mathbf{u}|_{\mathbf{x}})]^\alpha(s) = \mathbf{u}|_{\mathbf{x}} \qquad \alpha \in \mathcal{F}_{net}, s \in [0, L_\alpha], \tag{32}$$

i.e,. the macro-scale displacement at point $\mathbf{x}$ is inserted uniformly in the network (joints and trusses). The macro-scale gradient tensor at point $\mathbf{x}$ is mapped into the micro-scale kinematics through the following operator

$$\begin{aligned} &\mathcal{J}_\mu^{\mathscr{E}} : \mathbb{R}^{\mathrm{n_d}\times\mathrm{n_d}} \to \mathscr{U}_\mu, \\ &\qquad \mathbf{G}|_{\mathbf{x}} \mapsto \mathcal{J}_\mu^{\mathscr{E}}(\mathbf{G}|_{\mathbf{x}}) = (\mathcal{J}_\mu^{\mathscr{E},N}(\mathbf{G}|_{\mathbf{x}}), \mathcal{J}_\mu^{\mathscr{E},F}(\mathbf{G}|_{\mathbf{x}})), \end{aligned} \tag{33}$$

defined by

$$[\mathcal{J}_\mu^{\mathscr{E},N}(\mathbf{G}|_{\mathbf{x}})]^i = \mathbf{G}|_{\mathbf{x}}(\mathbf{y}^i - \mathbf{y}^G), \qquad i \in \mathcal{N}_{net}, \tag{34}$$

$$[\mathcal{J}_\mu^{\mathscr{E},F}(\mathbf{G}|_{\mathbf{x}})]^\alpha(s) = \mathbf{G}|_{\mathbf{x}}\left(\left(1 - \frac{s}{L_\alpha}\right)\mathbf{y}^{i\alpha} + \frac{s}{L_\alpha}\mathbf{y}^{j\alpha} - \mathbf{y}^G\right), \qquad \alpha \in \mathcal{F}_{net}, s \in [0, L_\alpha]. \tag{35}$$

where $\mathbf{y}^G$ is the geometric centre for the network of fibres, still to be defined in (46).

Remark 6. The macro-scale displacement and gradient are only inserted in the material domain, that is, in the locus of material particles at the micro-scale, specifically at nodes and in fibres. The empty space surrounding the network plays no role in the definition of the micro-scale kinematics.

The insertion operators $\mathcal{J}_\mu^{\mathscr{U}}$ and $\mathcal{J}_\mu^{\mathscr{E}}$ provide, for a macro-scale kinematics at point $\mathbf{x}$ fully characterised by the pair $(\mathbf{u}|_{\mathbf{x}}, \mathbf{G}|_{\mathbf{x}})$, an affine description of the micro-scale kinematics. In order to allow a nonaffine displacement in the *Network*, we introduce the so-called micro-scale displacement fluctuations $\tilde{\mathbb{U}}_\mu \in \mathscr{U}_\mu$ (see Remark 7) such that the micro-scale displacement (and its virtual variations) can be expressed through the following expansion

$$\mathbb{U}_\mu = \mathcal{J}_\mu^{\mathscr{U}}(\mathbf{u}|_{\mathbf{x}}) + \mathcal{J}_\mu^{\mathscr{E}}(\mathbf{G}|_{\mathbf{x}}) + \tilde{\mathbb{U}}_\mu, \tag{36}$$

which, in the nodal-wise sense results

$$\mathbf{u}_\mu^i = \mathbf{u}|_{\mathbf{x}} + \mathbf{G}|_{\mathbf{x}}(\mathbf{y}^i - \mathbf{y}^G) + \tilde{\mathbf{u}}_\mu^i \quad i \in \mathcal{N}_{net}, \tag{37}$$

where $\tilde{\mathbf{u}}_\mu^i$ is the displacement fluctuations of a node $i \in \mathcal{N}_{net}$ of the generalised fluctuation $\tilde{\mathbb{U}}_\mu$ (notation is as in (25)).

Remark 7. Fluctuations $\tilde{\mathbb{U}}_\mu$ is not an arbitrary element of $\mathscr{U}_\mu$ but it belongs to a specific space (subspace of $\mathscr{U}_\mu$), the so-called space of admissible displacement fluctuations, denoted by $\widetilde{\mathscr{U}}_\mu$. So far, it is only important to keep in mind that the different manners to define $\widetilde{\mathscr{U}}_\mu$ imply in more or less constrained kinematics, as illustrated in Fig. 4. The mathematical characterisation of this family of spaces is subject of Section 4.6.3.

Remark 8. From definition (36), the triple $(\mathbf{u}|_{\mathbf{x}}, \mathbf{G}|_{\mathbf{x}}, \tilde{\mathbb{U}}_\mu) \in \mathbb{R}^{\mathrm{n_d}} \times \mathbb{R}^{\mathrm{n_d}\times\mathrm{n_d}} \times \widetilde{\mathscr{U}}_\mu$ (see Remark 7) uniquely characterises the displacement $\mathbb{U}_\mu \in \mathscr{U}_\mu$. This connection is used in Section 4.5.

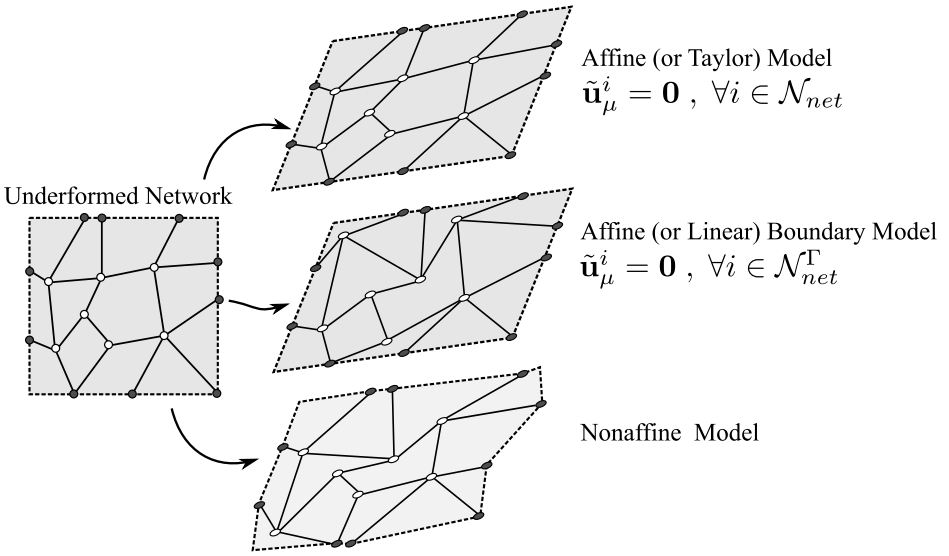

Fig. 4. Affine kinematics and nonaffine kinematics due to the existence of fluctuations.

4.5. Generalised micro-scale gradient operator

In this section we define the *generalised gradient* operation in the micro-scale reference configuration. This operator, similarly to the gradient in continuum mechanics, provides the measure of the first order variation of the displacement field defined in the network.

Associated to $\mathscr{U}_\mu$, we have the space of *generalised gradients* given by

$$\begin{aligned}\mathscr{E}_\mu = \{&\mathbb{G}_\mu = (\{\mathbf{G}^i_\mu\}_{i\in\mathcal{N}_{net}}, \{\mathbf{G}^\alpha_\mu\}_{\alpha\in\mathcal{F}_{net}});\\ &\mathbf{G}^i_\mu \in \mathbb{R}^{\mathrm{n_d}\times\mathrm{n_d}},\ i \in \mathcal{N}_{net}, \mathbf{G}^\alpha_\mu \in \mathbb{R}^{\mathrm{n_d}\times\mathrm{n_d}},\ \alpha \in \mathcal{F}_{net}\}.\end{aligned} \tag{38}$$

The addition in $\mathscr{E}_\mu$ is defined in the same sense as in (28)–(29).

For a given *NET-gradient* $\mathbb{G}_\mu \in \mathscr{E}_\mu$, we denote the *N-gradient* $\mathbf{G}^i_\mu$ a generalised gradient measure at node $i \in \mathcal{N}_{net}$ and the *F-gradient* $\mathbf{G}^\alpha_\mu$ a generalised gradient for fibre $\alpha \in \mathcal{F}_{net}$. The relation between node displacements and the generalised gradients in nodes and fibres is given through the *generalised micro-scale gradient operator*

$$\begin{aligned}&\mathcal{D}_\mu : \mathscr{U}_\mu \to \mathscr{E}_\mu,\\ &\qquad \mathbb{U}_\mu \mapsto \mathbb{G}_\mu = \mathcal{D}_\mu(\mathbb{U}_\mu),\end{aligned} \tag{39}$$

where $\mathbb{G}_\mu = (\{\mathbf{G}^i_\mu\}_{i\in\mathcal{N}_{net}}, \{\mathbf{G}^\alpha_\mu\}_{\alpha\in\mathcal{F}_{net}})$ is defined through

$$\mathbf{G}^i_\mu := \tilde{\mathbf{u}}^i_\mu \otimes \mathbf{m}_i \qquad \forall i \in \mathcal{N}_{net}, \tag{40}$$

$$\mathbf{G}^\alpha_\mu := \frac{1}{L_\alpha}\Delta^\alpha \mathbb{U}_\mu \otimes \mathbf{a}^\alpha \qquad \forall \alpha \in \mathcal{F}_{net}, \tag{41}$$

with $\mathbf{m}_i$ being the *joint normal vector* defined in (24). An alternative form to (41) is given by

$$\mathbf{G}^\alpha_\mu = \mathbf{G}|_{\mathbf{x}}\mathbf{a}^\alpha \otimes \mathbf{a}^\alpha + \frac{1}{L_\alpha}\Delta^\alpha \tilde{\mathbb{U}}_\mu \otimes \mathbf{a}^\alpha. \tag{42}$$

The definition of the *N-gradient*, given by (40), is reached by considering the integral of the gradient of the displacement field in the domain of a joint, as detailed in Appendix A.2. Hence, if we understand the gradient as a measure of the non-homogeneity of the displacement field, the *N-gradient* amounts to the total non-homogeneity lumped at a joint connecting a certain number of concurrent fibres. As can also be appreciated in Appendix A.2, it can be proved that only fluctuations play an important role in our model in which joints are idealised to be small.

Definition (41) can be regarded as the gradient of the displacement field in some fixed (global) coordinate frame of a straight truss. Remember that for the truss the only mechanically relevant kinematics is along its axial coordinate.

The alternative expression (42) is obtained by the replacing (36) into (41). For the interested reader, the full derivations in a continuum setting are exhibited in Appendix A.2. The physical meaning of the F-gradient in each fibre is such that the vector $(\mathbf{I}+\mathbf{G}_\mu^\alpha)\mathbf{a}^\alpha$[5] is pointed in the actual direction of the fibre and its euclidean norm is the stretch of the fibre (ratio between actual and original lengths).

It is important to remember that the *NET-gradient* $\mathbb{G}_\mu$ collects generalised gradients from two different kinds of components, i.e, nodes and fibres, being these, respectively, zero-dimensional and one-dimensional entities. Therefore, units are not homogeneous between *N-gradient* and *F-gradient*. Specifically in the case of *N-gradient*, it is not dimensionless, as classical gradients are, but it already has units of volume (this is actually a matter of convention). Although not classical, our special definition for $\mathbb{G}_\mu$ shows to be particularly suitable when we postulate the homogenisation for gradients in Section 4.6.2.

Remark 9. At this point, it is important to highlight that the RVE domain Ω_μ and the network of fibres NET are different concepts. Domain Ω_μ is understood as an observational window of the macro-scale point $\mathbf{x} \in \Omega$, while NET is the collection of material particles for which a minimum set of geometrical and topological information was endowed to adequately describe the discrete kinematical structure for the problem. The RVE domain Ω_μ contains the NET and empty space surrounding the NET. Hence, the NET provides the material substrate on top of which kinematical quantities and generalised gradient measures are defined.

Remark 10. Definition (39) is such that the insertion of a uniform displacement field yields null gradient. In other words, it is verified that $\mathcal{D}_\mu(\mathcal{J}_\mu^{\mathscr{U}}(\mathbf{u}|_{\mathbf{x}})) = \mathbf{O}$ (see proof in Appendix B).

Remark 11. Both definitions, (40) and (41), imply certain geometrical considerations. In the former, only the solid part of the joint boundary is considered as it comes from the definition of *joint normal vector* in (24). In the later, only the axial part of the gradient plays a role for the strain tensor as dictated by the one-dimensional character of fibres. As we will see in Section 4.6, these two model simplifications have to be taken into consideration when homogenisation operators are postulated.

4.6. Kinematic homogenisation operators

In this section we define the homogenisation operators which establish the kinematical connection between the kinematics at both scales, providing a sense of kinematic conservation in the multi-scale transfer. Furthermore, these operators clearly define the admissible kinematical restrictions to be satisfied by the displacement fluctuations in the network.

4.6.1. Homogenisation of displacements

First, consider the homogenisation operator for the displacement field (and for its virtual variations) defined as

$$\begin{aligned} &\mathcal{H}_\mu^{\mathscr{U}} : \mathscr{U}_\mu \to \mathbb{R}^{\mathrm{n_d}}, \\ &\mathbb{U}_\mu \mapsto \mathcal{H}_\mu^{\mathscr{U}}(\mathbb{U}_\mu) = \frac{1}{|\mathcal{F}_{net}|}\sum_{\alpha\in\mathcal{F}_{net}} \frac{V_\alpha}{2}(\mathbf{u}_\mu^{i_\alpha}+\mathbf{u}_\mu^{j_\alpha}). \end{aligned} \tag{43}$$

Note that, by construction, $\mathcal{H}_\mu^{\mathscr{U}}$ satisfies

$$\mathcal{H}_\mu^{\mathscr{U}}(\mathcal{J}_\mu^{\mathscr{U}}(\mathbf{u}|_{\mathbf{x}})) = \mathbf{u}|_{\mathbf{x}}. \tag{44}$$

We also require

$$\mathcal{H}_\mu^{\mathscr{U}}(\mathcal{J}_\mu^{\mathscr{E}}(\mathbf{G}|_{\mathbf{x}})) = \mathbf{0}, \tag{45}$$

that leads to

$$\mathbf{y}^G = \frac{1}{|\mathcal{F}_{net}|}\sum_{\alpha\in\mathcal{F}_{net}} \frac{V_\alpha}{2}(\mathbf{y}^{i_\alpha}+\mathbf{y}^{j_\alpha}), \tag{46}$$

[5] Instead of $\mathbf{G}_\mu^\alpha$ as primary generalised gradient variable, we can equivalently define $\mathbf{F}_\mu^\alpha = (\mathbf{I}+\mathbf{G}_\mu^\alpha)$ as the generalised deformation gradient associated to $\mathbf{G}_\mu^\alpha$, which leads to an equivalent formulation.

whose proof is given in Appendix B. Note that constraint (45) is needed for the homogenised displacement to be independent from the macro-scale gradient.

The macro-scale and micro-scale displacement fields (or its virtual variations) are constrained to satisfy the following

$$\mathcal{H}_\mu^{\mathscr{U}}(\mathbb{U}_\mu) = \mathbf{u}|_{\mathbf{x}}. \tag{47}$$

Since the operator is linear, this is equivalent to

$$\mathcal{H}_\mu^{\mathscr{U}}(\mathbb{U}_\mu) = \mathcal{H}_\mu^{\mathscr{U}}(\mathcal{J}_\mu^{\mathscr{U}}(\mathbf{u}|_{\mathbf{x}})) + \mathcal{H}_\mu^{\mathscr{U}}(\mathcal{J}_\mu^{\mathscr{E}}(\mathbf{G}|_{\mathbf{x}})) + \mathcal{H}_\mu^{\mathscr{U}}(\tilde{\mathbb{U}}_\mu) = \mathbf{u}|_{\mathbf{x}}, \tag{48}$$

which implies, from (44) and (45), that the fluctuation $\tilde{\mathbb{U}}_\mu$ must satisfy

$$\mathcal{H}_\mu^{\mathscr{U}}(\tilde{\mathbb{U}}_\mu) = \frac{1}{|\mathcal{F}_{net}|}\sum_{\alpha\in\mathcal{F}_{net}} \frac{V_\alpha}{2}(\tilde{\mathbf{u}}_\mu^{i_\alpha} + \tilde{\mathbf{u}}_\mu^{j_\alpha}) = \mathbf{0}. \tag{49}$$

Remark 12 (*Continuum Case*)**.** The definition in (43) is equivalent to taking the volumetric integral over the ensemble of fibres modelled as continuum as detailed in Appendix A.2. This homogenisation formula follows the same ideas from continuum media, for which $\mathbf{v}|_{\mathbf{x}} = \frac{1}{|B_\mu^s|}\int_{B_\mu^s}\mathbf{v}_\mu \mathrm{d}B_\mu$, where B_μ^s is the solid part of B_μ (RVE domain), $\mathbf{v}_\mu$ a micro-scale displacement field and $\mathbf{v}|_{\mathbf{x}}$ the displacement from the macro-scale. Thus, restriction (49) is analogous to the zero-mean integral for fluctuation, i.e, $\int_{B_\mu^s}\tilde{\mathbf{v}}_\mu \mathrm{d}B_\mu = \mathbf{0}$, in continuum multi-scale formulations (see Appendix A.1 for details).

4.6.2. *Homogenisation of generalised micro-scale gradient*

We propose the homogenisation operator for the generalised micro-scale gradient (and for its virtual variations)

$$\begin{aligned}\mathcal{H}_\mu^{\mathscr{E}} &: \mathscr{E}_\mu \to \mathbb{R}^{\mathrm{n_d}\times\mathrm{n_d}},\\ &\mathbb{G}_\mu \mapsto \mathcal{H}_\mu^{\mathscr{E}}(\mathbb{G}_\mu),\end{aligned} \tag{50}$$

defined by

$$\mathcal{H}_\mu^{\mathscr{E}}(\mathbb{G}_\mu) = \frac{1}{|\mathcal{F}_{net}|}\left(\sum_{\alpha\in\mathcal{F}_{net}} V_\alpha \mathbf{G}_\mu^\alpha + \sum_{i\in\mathcal{N}_{net}} \mathbf{G}_\mu^i - \sum_{i\in\mathcal{N}_{net}^\Gamma} \bar{A}_i \tilde{\mathbf{u}}_\mu^i \otimes \bar{\mathbf{n}}\right)\mathbf{B}^{-1}, \tag{51}$$

where $\mathbf{B}$ is an invertible second order tensor called *structural tensor* and $\bar{\mathbf{n}}$ is the *average normal vector*. These two geometric objects will be defined in (55) and (59), respectively. Note that (51) can be seen as a discrete counterpart of the integral of the gradient of the displacement field in the material domain plus the incorporation of additional terms that make the homogenisation consistent. The full justification, based on the kinematics of continua, is found in Appendix A.

Before proceeding with the definitions for $\mathbf{B}$ and $\bar{\mathbf{n}}$, let us first rewrite (51). Let us simplify the first two summations in (51), by using (40) and (42), as next

$$\begin{aligned}&\sum_{\alpha\in\mathcal{F}_{net}} V_\alpha \mathbf{G}_\mu^\alpha + \sum_{i\in\mathcal{N}_{net}} \mathbf{G}_\mu^i =\\ &\sum_{\alpha\in\mathcal{F}_{net}} V_\alpha\left(\mathbf{G}|_{\mathbf{x}}\mathbf{a}^\alpha\otimes\mathbf{a}^\alpha + \frac{1}{L_\alpha}\Delta^\alpha\tilde{\mathbb{U}}_\mu\otimes\mathbf{a}^\alpha\right) + \sum_{i\in\mathcal{N}_{net}}\tilde{\mathbf{u}}_\mu^i\otimes\mathbf{m}_i =\\ &\sum_{\alpha\in\mathcal{F}_{net}} V_\alpha\mathbf{G}|_{\mathbf{x}}\mathbf{a}^\alpha\otimes\mathbf{a}^\alpha + \sum_{i\in\mathcal{N}_{net}}\sum_{\alpha\in\mathcal{F}_{net}^i}[\alpha,i]A_\alpha\tilde{\mathbf{u}}_\mu^i\otimes\mathbf{a}^\alpha\\ &\quad+\sum_{i\in\overset{\circ}{\mathcal{N}}_{net}}\tilde{\mathbf{u}}_\mu^i\otimes\left(-\sum_{\alpha\in\mathcal{F}_{net}^i}[\alpha,i]A_\alpha\mathbf{a}^\alpha\right) + \sum_{i\in\mathcal{N}_{net}^\Gamma}\tilde{\mathbf{u}}_\mu^i\otimes\left(\bar{A}_i\mathbf{n}_i - \sum_{\alpha\in\mathcal{F}_{net}^i}[\alpha,i]A_\alpha\mathbf{a}^\alpha\right) =\\ &\sum_{\alpha\in\mathcal{F}_{net}} V_\alpha\mathbf{G}|_{\mathbf{x}}\mathbf{a}^\alpha\otimes\mathbf{a}^\alpha + \sum_{i\in\mathcal{N}_{net}^\Gamma}\bar{A}_i\tilde{\mathbf{u}}_\mu^i\otimes\mathbf{n}_i.\end{aligned} \tag{52}$$

Replacing the above expression into (51) we get the equivalent homogenisation relation below

$$\mathcal{H}^{\mathscr{E}}_{\mu}(\mathbb{G}_{\mu}) = \frac{1}{|\mathcal{F}_{net}|}\Bigg(\sum_{\alpha\in\mathcal{F}_{net}} V_{\alpha}\mathbf{G}|_{\mathbf{x}}\mathbf{a}^{\alpha}\otimes\mathbf{a}^{\alpha} + \sum_{i\in\mathcal{N}^{\Gamma}_{net}} \bar{A}_i\tilde{\mathbf{u}}^{i}_{\mu}\otimes(\mathbf{n}_i-\bar{\mathbf{n}})\Bigg)\mathbf{B}^{-1}. \tag{53}$$

The first fundamental requirement the operator $\mathcal{H}^{\mathscr{E}}_{\mu}(\cdot)$ must fulfil is that, for an affine model (i.e $\tilde{\mathbb{U}}_{\mu}=\mathbb{O}$) one has to retrieve the macro-scale gradient $\mathbf{G}|_{\mathbf{x}}$, that is

$$\mathcal{H}^{\mathscr{E}}_{\mu}(\mathbb{G}_{\mu}|_{\tilde{\mathbb{U}}_{\mu}=\mathbb{O}}) = \mathbf{G}|_{\mathbf{x}}, \tag{54}$$

then, from (53) we are led to the definition of $\mathbf{B}$

$$\mathbf{B} := \frac{1}{|\mathcal{F}_{net}|}\Bigg(\sum_{\alpha\in\mathcal{F}_{net}} V_{\alpha}\mathbf{a}^{\alpha}\otimes\mathbf{a}^{\alpha}\Bigg). \tag{55}$$

This tensor, named here as *structural tensor* (also called *orientation tensor*), is a concept which has also been found in the phenomenological modelling [4,33]. This theoretical connection can be regarded as a mathematical justification for the phenomenological importance of this tensor.

In turn, a second fundamental property of operator $\mathcal{H}^{\mathscr{E}}_{\mu}(\cdot)$ is that, for a uniform fluctuation field ($\tilde{\mathbb{U}}_{\mu}=\mathbb{C}$), we get the very same macro-scale gradient, this means

$$\mathcal{H}^{\mathscr{E}}_{\mu}(\mathbb{G}_{\mu}|_{\tilde{\mathbb{U}}_{\mu}=\mathbb{C}}) = \mathbf{G}|_{\mathbf{x}}, \tag{56}$$

Since $\mathcal{H}^{\mathscr{E}}_{\mu}$ is a linear operator, from (56) we obtain

$$\mathcal{H}^{\mathscr{E}}_{\mu}(\mathbb{G}_{\mu}|_{\tilde{\mathbb{U}}_{\mu}=\mathbb{C}}) = \mathcal{H}^{\mathscr{E}}_{\mu}(\mathbb{G}_{\mu}|_{\tilde{\mathbb{U}}_{\mu}=\mathbb{O}}) + \mathcal{H}^{\mathscr{E}}_{\mu}(\mathbb{G}_{\mu}|_{\mathbf{G}|_{\mathbf{x}}=\mathbf{O},\tilde{\mathbb{U}}_{\mu}=\mathbb{C}}) = \mathbf{G}|_{\mathbf{x}}, \tag{57}$$

which gives $\mathcal{H}^{\mathscr{E}}_{\mu}(\mathbb{G}_{\mu}|_{\mathbf{G}|_{\mathbf{x}}=\mathbf{O},\tilde{\mathbb{U}}_{\mu}=\mathbb{C}}) = \mathbf{O}$ by using (54). Finally, since

$$\mathcal{H}^{\mathscr{E}}_{\mu}(\mathbb{G}_{\mu}|_{\mathbf{G}|_{\mathbf{x}}=\mathbf{O},\tilde{\mathbb{U}}_{\mu}=\mathbb{C}}) = \frac{1}{|\mathcal{F}_{net}|}\Bigg(\sum_{i\in\mathcal{N}^{\Gamma}_{net}} \bar{A}_i\tilde{\mathbf{u}}^{i}_{\mu}\otimes(\mathbf{n}_i-\bar{\mathbf{n}})\Bigg)\mathbf{B}^{-1} = \mathbf{O}, \tag{58}$$

we obtain the definition for the vector $\bar{\mathbf{n}}$ as

$$\bar{\mathbf{n}} := \frac{1}{\sum_{i\in\mathcal{N}^{\Gamma}_{net}}\bar{A}_i}\Bigg(\sum_{i\in\mathcal{N}^{\Gamma}_{net}} \bar{A}_i\mathbf{n}_i\Bigg). \tag{59}$$

Remark 13. Note that the final expression for $\bar{\mathbf{n}}$ in (59) is simply the average normal over the solid boundary. The *average normal vector* is a measure of the geometric unbalance in the solid part of the RVE boundary and, as we will see, it plays a fundamental role in the minimally constrained kinematical model, and consequently in the characterisation of the dual entities.

Remark 14. Properties (54) and (56), which ensure the conservation of the deformation gradient and kinematical consistency of our model, naturally and univocally shape the tensor $\mathbf{B}$ and the vector $\bar{\mathbf{n}}$. In other words, the expressions (55) and (59) result from the homogenisation of gradient postulated in (51), which embodies the choice for the NET-gradient in (39), altogether with the considerations taken for the structural elements in the network (nodes and bars).

Analogously to (47), the micro-scale gradient measure is constrained to satisfy the following

$$\mathcal{H}^{\mathscr{E}}_{\mu}(\mathbb{G}_{\mu}) = \mathbf{G}|_{\mathbf{x}}, \tag{60}$$

which implies, by linearity, that the fluctuation must satisfy

$$\mathcal{H}^{\mathscr{E}}_{\mu}(\mathbb{G}_{\mu}|_{\mathbf{G}|_{\mathbf{x}}=\mathbf{O}}) = \mathbf{O}, \tag{61}$$

or, more explicitly, and by using (53), the fluctuation must be compliant with the following constraint

$$\mathcal{H}^{\mathscr{E}}_{\mu}(\mathbb{G}_{\mu}|_{\mathbf{G}|_{\mathbf{x}}=\mathbf{O}}) = \frac{1}{|\mathcal{F}_{net}|}\Bigg(\sum_{i\in\mathcal{N}^{\Gamma}_{net}} \bar{A}_i\tilde{\mathbf{u}}^{i}_{\mu}\otimes(\mathbf{n}_i-\bar{\mathbf{n}})\Bigg)\mathbf{B}^{-1} = \mathbf{O}. \tag{62}$$

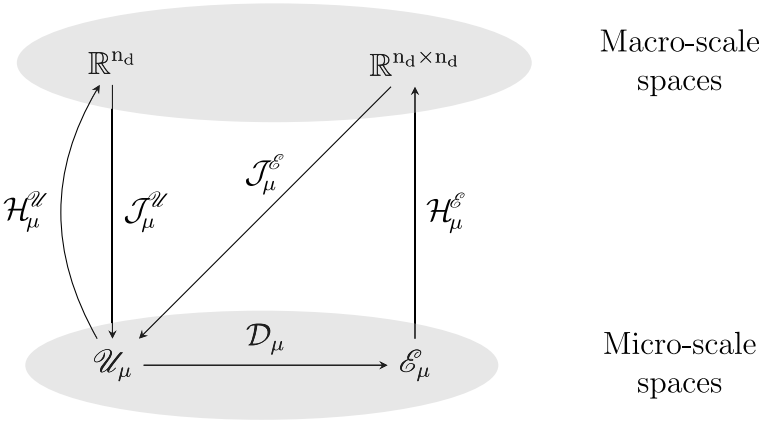

Fig. 5. Diagram of kinematics: relation between spaces and operators.

The fact that (62) solely depends on boundary data is reasonable as one should expect to be able to control the RVE deformation exclusively by using the displacement field defined over the material points of the RVE that reach the boundary.

Remark 15 (*Continuum Case*)**.** As the tensor $\mathbf{B}$ is assumed to be invertible, post-multiplication of (62) by $\mathbf{B}$ leads to the alternative restriction

$$\sum_{i \in \mathcal{N}^{\Gamma}_{net}} \bar{A}_i \tilde{\mathbf{u}}^i_\mu \otimes (\mathbf{n}_i - \bar{\mathbf{n}}) = \mathbf{O}. \tag{63}$$

This last expression has a clear parallel with that one encountered in multi-scale models with no voids reaching boundary $\int_{\partial B_\mu} \tilde{\mathbf{u}}_\mu \otimes \boldsymbol{\nu}\, \mathrm{d}\partial B_\mu = \mathbf{O}$, with B_μ being the RVE domain and ∂B_μ it is boundary for which the outward normal unit vector is $\boldsymbol{\nu}$ [30,39]. In our context, voids do reach the boundary (the empty space between fibres) and the above expression had to be generalised to an integral over $\partial B^s_\mu \cap \partial B_\mu$, where B^s_μ is the solid part of the RVE (see details in Appendix A.1), as consequence the *average normal vector* has arisen as a necessary adjusting term to generalise the classical constraint, while maintaining kinematical consistency.

In terms of relations between spaces and operators, the multi-scale kinematic setting can be summarised through the diagram of Fig. 5.

4.6.3. Space of admissible fluctuations

Using kinematical constraints given in (47) and (60), which ensure preservation of kinematical descriptors between macro and micro scales, we arrive respectively to the restrictions (49) and (63) for fluctuations. This allows us to define the largest space of kinematically admissible displacement fluctuations (and its virtual variations)

$$\widetilde{\mathscr{U}}^{\mathsf{M}}_\mu = \left\{ \tilde{\mathbb{U}}_\mu \in \mathscr{U}_\mu;\ \sum_{\alpha \in \mathcal{F}_{net}} \frac{V_\alpha}{2} (\tilde{\mathbf{u}}^{i_\alpha}_\mu + \tilde{\mathbf{u}}^{j_\alpha}_\mu) = \mathbf{0};\ \sum_{i \in \mathcal{N}^{\Gamma}_{net}} \bar{A}_i \tilde{\mathbf{u}}^i_\mu \otimes (\mathbf{n}_i - \bar{\mathbf{n}}) = \mathbf{O} \right\}. \tag{64}$$

The space $\widetilde{\mathscr{U}}^{\mathsf{M}}_\mu$ is a subspace of $\mathscr{U}_\mu$ whose elements satisfy the minimum set of constraints such that kinematic conservation is guaranteed. Hence, space $\widetilde{\mathscr{U}}^{\mathsf{M}}_\mu$ defines the *minimally constrained multi-scale model* (MCMM), also known in literature as *uniform traction model* for the reasons that will be clear in Section 7. Other more constrained models, defined by corresponding spaces $\widetilde{\mathscr{U}}^{*}_\mu$ are also possible, provided they satisfy $\widetilde{\mathscr{U}}^{*}_\mu \subset \widetilde{\mathscr{U}}^{\mathsf{M}}_\mu$. Three sub-models with theoretical and practical relevance are the following:

(i) Affine model (also called Taylor model or *rule of mixtures*): this model does not allow fluctuations neither in interior nodes neither on the boundary, being the most kinematically constrained scenario. Such model can be

obtained as sub-model of the MCMM proposed here by taking

$$\widetilde{\mathscr{U}}_\mu^{\mathsf{T}} = \{\tilde{\mathbb{U}}_\mu \in \mathscr{U}_\mu;\ \tilde{\mathbf{u}}_\mu^i = \mathbf{0},\ i \in \mathcal{N}_{net}\}. \tag{65}$$

(ii) Affine boundary model (also called linear boundary model): this model allows nonzero fluctuations only in interior nodes which renders this scenario be less constrained than the Affine model. Mathematically we have

$$\widetilde{\mathscr{U}}_\mu^{\mathsf{L}} = \{\tilde{\mathbb{U}}_\mu \in \mathscr{U}_\mu;\ \mathcal{H}_\mu^{\mathscr{U}}(\tilde{\mathbb{U}}_\mu) = \mathbf{0}, \tilde{\mathbf{u}}_\mu^i = \mathbf{0},\ i \in \mathcal{N}_{net}^\Gamma\}. \tag{66}$$

(iii) Periodic boundary model[6]: Still less constrained than the Affine boundary model, this model allows nonzero fluctuations over the RVE boundary such that

$$\begin{aligned}\widetilde{\mathscr{U}}_\mu^{\mathsf{P}} = \{&\tilde{\mathbb{U}}_\mu \in \mathscr{U}_\mu;\ \mathcal{H}_\mu^{\mathscr{U}}(\tilde{\mathbb{U}}_\mu) = \mathbf{0}, \tilde{\mathbf{u}}_\mu^{i_+} = \tilde{\mathbf{u}}_\mu^{i_-},\\ &(i_+, i_-) \in (\mathcal{N}_{net}^\Gamma)^+ \times (\mathcal{N}_{net}^\Gamma)^- \text{ is a periodic pair }\},\end{aligned} \tag{67}$$

where by periodic pair it is meant that $\bar{A}_{i_+,k_+} = \bar{A}_{i_-,k_-}$ and $\mathbf{n}_{i_+,k_+} = -\mathbf{n}_{i_-,k_-}$, given that $\{(\mathcal{N}_{net}^\Gamma)^+, (\mathcal{N}_{net}^\Gamma)^-\}$ is a partition of $\mathcal{N}_{net}^\Gamma$. Since $\bar{\mathbf{n}} = \mathbf{0}$ in this case, it is not difficult to see that $\widetilde{\mathscr{U}}_\mu^{\mathsf{P}} \subset \widetilde{\mathscr{U}}_\mu^{\mathsf{M}}$.

As already pointed out, the characterisation of the minimal set of kinematical constraints in the present context is a valuable aspect of the proposed model, because the space $\widetilde{\mathscr{U}}_\mu^{\mathsf{M}}$ established the admissible kinematical ground to derive other sub-models whose admissibility is guaranteed. An example of a non-classical subspace, not yet explored in the literature, is given by splitting the summation appearing in (63) and enforcing each of these parts to be zero.

Note that the aforementioned spaces satisfy the following hierarchy $\widetilde{\mathscr{U}}_\mu^{\mathsf{T}} \subset \widetilde{\mathscr{U}}_\mu^{\mathsf{L}} \subset \widetilde{\mathscr{U}}_\mu^{\mathsf{P}} \subset \widetilde{\mathscr{U}}_\mu^{\mathsf{M}}$. A helpful visualisation to show the transition from a more constrained model to a less constrained one is seen in Fig. 4. In particular, numerical examples presented in Section 9 address the effect of the choice of the fluctuation displacement spaces in the homogenised stress tensor at macro scale.

Finally, hereafter we denote $\widetilde{\mathscr{U}}_\mu$ to the space $\widetilde{\mathscr{U}}_\mu^{\mathsf{M}}$. In turn, the space of kinematically admissible virtual variations associated to $\widetilde{\mathscr{U}}_\mu$ is itself $\widetilde{\mathscr{U}}_\mu$, i.e, if $\hat{\tilde{\mathbb{U}}}_\mu = (\tilde{\mathbb{U}}_\mu)_1 - (\tilde{\mathbb{U}}_\mu)_2$ with $(\tilde{\mathbb{U}}_\mu)_1, (\tilde{\mathbb{U}}_\mu)_2 \in \widetilde{\mathscr{U}}_\mu$, hence $\hat{\tilde{\mathbb{U}}}_\mu \in \widetilde{\mathscr{U}}_\mu$.

5. Mathematical duality and virtual power

In this section the virtual power functionals at both scales are postulated according to the kinematical framework considered at each scale.

At the macro-scale, and in view of the model already presented in Section 3, we have that the internal virtual power exerted at a given point $\mathbf{x}$ in a volume $|\Omega_\mu|$ is characterised as follows[7]

$$\mathcal{P}_{M|\mathbf{x}}^{\text{int}}(\hat{\mathbf{G}}|_{\mathbf{x}}) = -|\Omega_\mu|\mathbf{P}|_{\mathbf{x}} \cdot \hat{\mathbf{G}}|_{\mathbf{x}}, \tag{68}$$

where $\mathbf{P}|_{\mathbf{x}}$ is the first Piola–Kirchhoff stress tensor at point $\mathbf{x}$, which is the stress measure power-conjugate to the virtual variation of the displacement gradient $\hat{\mathbf{G}}|_{\mathbf{x}}$. Here, $|\Omega_\mu|$ is the volume of the micro-scale domain where the internal power is considered to be exerted. Thus, this measure corresponds to the size of the RVE.

Regarding the micro-scale, and according to the micro-scale kinematical setting presented in Section 4.2, the internal virtual power is a linear functional of $\hat{\mathbb{G}}_\mu$. Then, by duality arguments it admits the following characterisation

$$\mathcal{P}_\mu^{\text{int},*}(\hat{\mathbb{G}}_\mu) = -\sum_{\alpha \in \mathcal{F}_{net}} V_\alpha \mathbf{S}_\mu^\alpha \cdot \hat{\mathbf{G}}_\mu^\alpha - \sum_{i \in \mathcal{N}_{net}} \mathbf{S}_\mu^i \cdot \hat{\mathbf{G}}_\mu^i, \tag{69}$$

where $\mathbf{S}_\mu^\alpha$ and $\mathbf{S}_\mu^i$ are generalised stresses for a fibre $\alpha \in \mathcal{F}_{net}$ and for a node $i \in \mathcal{N}_{net}$, respectively.

Hence, the model allows the N-gradient at each node to be different from zero as would be the case of torsional resistance at fibre connections because of fibre entanglement. However, as postulated earlier in this work, we admit that the generalised stress at nodes is zero, then (69) becomes

$$\mathcal{P}_\mu^{\text{int}}(\hat{\mathbb{G}}_\mu) = -\sum_{\alpha \in \mathcal{F}_{net}} V_\alpha \mathbf{S}_\mu^\alpha \cdot \hat{\mathbf{G}}_\mu^\alpha, \tag{70}$$

which is the final format for the micro-scale internal virtual power used in the following developments.

[6] It requires geometric periodicity of fibres reaching the boundary in terms of direction, area and position.

[7] The minus sign in the definition of internal virtual power is to keep the usual convention adopted for the internal virtual power.

According to (41), the stress tensor $\mathbf{S}_\mu^\alpha$ has the structure $\mathbf{S}_\mu^\alpha = \mathbf{s}_\mu^\alpha \otimes \mathbf{a}^\alpha$ with $\mathbf{s}_\mu^\alpha \in \mathbb{R}^{n_d}$. Then, the stress field in the entire network $\mathbb{S}_\mu^F$ is a field

$$\mathscr{S}_\mu = \{\mathbb{S}_\mu^F = \{\mathbf{S}_\mu^\alpha\}_{\alpha\in\mathcal{F}_{net}} : \mathcal{F}_{net} \to \mathbb{R}^{n_d\times n_d},\ \mathbf{S}_\mu^\alpha = \mathbf{s}_\mu^\alpha \otimes \mathbf{a}^\alpha,\ \mathbf{s}_\mu^\alpha \in \mathbb{R}^{n_d}\}. \tag{71}$$

Remark 16. Note that the micro-scale stress field is defined just in $\mathcal{F}_{net}$ and not in $\mathcal{N}_{net}\times\mathcal{F}_{net}$ as in $\mathscr{E}_\mu$ (see definition (38)). This is a primary consequence of (70) that led to the definition of the internal virtual power in the micro-scale, which neglects any virtual power exerted at the nodes in the network.

6. Principle of Multi-scale Virtual Power

In this section we postulate the principle of mechanical equilibrium between scales. To this aim, the Principle of Multi-scale Virtual Power (PMVP) and the virtual power functionals defined in Section 5 are invoked.

The PMVP in the present context can be understood as a generalised formulation of the Hill–Mandel Principle of Macrohomogeneity [47,48]. This principle states that the internal virtual power exerted by macro-scale entities at point $\mathbf{x}$ must equal the internal virtual power exerted in the corresponding micro-scale (the RVE) for all kinematically admissible fields. Mathematically, this is

$$\mathcal{P}^{\text{int}}_{M|\mathbf{x}}(\hat{\mathbf{G}}|_\mathbf{x}) = \mathcal{P}^{\text{int}}_\mu(\hat{\mathbb{G}}_\mu) \quad \forall(\hat{\mathbf{G}}|_\mathbf{x}, \hat{\mathbb{G}}_\mu) \text{ kinematically admissible}, \tag{72}$$

where $\hat{\mathbb{G}}_\mu = \hat{\mathbb{G}}_\mu(\hat{\mathbf{G}}|_\mathbf{x}, \hat{\tilde{\mathbb{U}}}_\mu)$. Using (68) and (70), and also (42) we formulate the PMVP as follows.

Problem 2 (*Principle of Multi-scale Virtual Power*)**.** Consider a point $\mathbf{x}$ in the macro-scale continuum, given the macro-scale gradient measure $\mathbf{G}|_\mathbf{x} \in \mathbb{R}^{n_d\times n_d}$, it is said that the macro-scale stress tensor at this point, $\mathbf{P}|_\mathbf{x}$, is in mechanical equilibrium with the network stress state, $\mathbb{S}_\mu^F = \{\mathbf{S}_\mu^\alpha\}_{\alpha\in\mathcal{F}_{net}}$, if the following variational equation is satisfied

$$\mathbf{P}|_\mathbf{x}\cdot\hat{\mathbf{G}}|_\mathbf{x} = \frac{1}{|\Omega_\mu|}\sum_{\alpha\in\mathcal{F}_{net}} V_\alpha \mathbf{S}_\mu^\alpha \cdot \left(\hat{\mathbf{G}}|_\mathbf{x}\mathbf{a}^\alpha \otimes \mathbf{a}^\alpha + \frac{1}{L_\alpha}\Delta^\alpha \hat{\tilde{\mathbb{U}}}_\mu \otimes \mathbf{a}^\alpha\right)$$
$$\forall(\hat{\mathbf{G}}|_\mathbf{x}, \hat{\tilde{\mathbb{U}}}_\mu) \in \mathbb{R}^{n_d\times n_d}\times\widetilde{\mathscr{U}}_\mu. \tag{73}$$

As natural consequences of the PMVP we have: (i) the homogenisation formula for $\mathbf{P}|_\mathbf{x}$ (see Section 6.1), and (ii) the variational problem that characterises the mechanical equilibrium at the micro-scale in terms of the fluctuations of the displacement field (see Section 6.2).

Remark 17. In variational equation (73), it is clear the distinction between the RVE domain, called Ω_μ, and the network NET, as already pointed by Remark 9. While the micro-scale virtual power is truly exerted in the trusses that form the NET, from the macro-scale point of view this corresponds to a subdomain of macro-continuum material whose size is defined to be $|\Omega_\mu|$. This RVE volume is partially filled by $|\mathcal{F}_{net}|$ plus the surrounding substance, as already discussed in Remark 1.

Remark 18 (*Incompressible Case*)**.** The PMVP in Problem 2 is easily cast into the incompressible case by appropriately defining submanifolds of $\mathbb{R}^{n_d\times n_d}$ where $\mathbf{G}|_\mathbf{x}$ and $\hat{\mathbf{G}}|_\mathbf{x}$ belong to. Following Remark 3, we have

$$\mathbf{G}|_\mathbf{x} \in \mathbb{M}_{\text{inc}} = \{\mathbf{A}\in\mathbb{R}^{n_d\times n_d};\ \det(\mathbf{I}+\mathbf{A}) = 1\}, \tag{74}$$

and

$$\hat{\mathbf{G}}|_\mathbf{x} \in \mathbb{T}_{\text{inc}} = \{\hat{\mathbf{A}}\in\mathbb{R}^{n_d\times n_d};\ \text{tr}\big(\hat{\mathbf{A}}(\mathbf{I}+\mathbf{G}|_\mathbf{x})^{-1}\big) = 0\}. \tag{75}$$

Moreover, the stress $\mathbf{P}|_\mathbf{x}$ is replaced by its isochoric component, namely $\mathbf{P}^{\text{iso}}|_\mathbf{x}$, whose derivation is shown in Remark 20.

6.1. Homogenisation formula for the stress-tensor

Let us take $\hat{\tilde{\mathbb{U}}}_\mu = \mathbb{O}$ in (73). We then derive the homogenisation formula for the stress tensor $\mathbf{P}$ at point $\mathbf{x}$ as follows

$$\mathbf{P}|_\mathbf{x}\cdot\hat{\mathbf{G}}|_\mathbf{x} = \frac{1}{|\Omega_\mu|}\sum_{\alpha\in\mathcal{F}_{net}} V_\alpha \mathbf{S}_\mu^\alpha \cdot (\hat{\mathbf{G}}|_\mathbf{x}\mathbf{a}^\alpha \otimes \mathbf{a}^\alpha) \quad \forall\hat{\mathbf{G}}|_\mathbf{x} \in \mathbb{R}^{n_d\times n_d}, \tag{76}$$

which yields

$$\left(\mathbf{P}|_{\mathbf{x}} - \frac{1}{|\Omega_\mu|}\sum_{\alpha\in\mathcal{F}_{net}} V_\alpha \mathbf{S}^\alpha_\mu \mathbf{a}^\alpha \otimes \mathbf{a}^\alpha\right)\cdot \hat{\mathbf{G}}|_{\mathbf{x}} = 0 \quad \forall \hat{\mathbf{G}}|_{\mathbf{x}} \in \mathbb{R}^{\mathrm{n_d}\times \mathrm{n_d}}. \tag{77}$$

Therefore, the homogenisation of the Piola–Kirchhoff stress tensor follows

$$\mathbf{P}|_{\mathbf{x}} = \frac{1}{|\Omega_\mu|}\sum_{\alpha\in\mathcal{F}_{net}} V_\alpha \mathbf{S}^\alpha_\mu \mathbf{a}^\alpha \otimes \mathbf{a}^\alpha. \tag{78}$$

Using the representation $\mathbf{S}^\alpha_\mu = \mathbf{s}^\alpha_\mu \otimes \mathbf{a}^\alpha$ (see (71)) we have

$$\mathbf{S}^\alpha_\mu \mathbf{a}^\alpha \otimes \mathbf{a}^\alpha = (\mathbf{s}^\alpha_\mu \otimes \mathbf{a}^\alpha)\mathbf{a}^\alpha \otimes \mathbf{a}^\alpha = \mathbf{s}^\alpha_\mu \otimes \mathbf{a}^\alpha = \mathbf{S}^\alpha_\mu, \tag{79}$$

and, so, the *Stress Homogenisation* operator results

$$\begin{aligned}\mathcal{H}_{\mathbf{P}} &: \mathscr{S}_\mu \to \mathbb{R}^{\mathrm{n_d}\times \mathrm{n_d}}\\ &\mathbb{S}^F_\mu \mapsto \mathcal{H}_{\mathbf{P}}(\mathbb{S}^F_\mu) := \frac{1}{|\Omega_\mu|}\sum_{\alpha\in\mathcal{F}_{net}} V_\alpha \mathbf{S}^\alpha_\mu = \frac{1}{|\Omega_\mu|}\sum_{\alpha\in\mathcal{F}_{net}} V_\alpha \mathbf{s}^\alpha_\mu \otimes \mathbf{a}^\alpha,\end{aligned} \tag{80}$$

in such way that $\mathbf{P}|_{\mathbf{x}} = \mathcal{H}_{\mathbf{P}}(\mathbb{S}^F_\mu)$.

It is also possible to derive a homogenisation formula completely equivalent to (80) but depending only on boundary data, i.e., on the stress state of fibres that reach the boundary (see Section 7).

Remark 19. Denoting $\boldsymbol{\sigma}_m = \frac{1}{\det \mathbf{F}}\mathbf{P}\mathbf{F}^T$ the material description of the Cauchy stress tensor, and noting that $\boldsymbol{\sigma}_m|_{\mathbf{x}} = \frac{1}{\det \mathbf{F}|_{\mathbf{x}}}\mathbf{P}|_{\mathbf{x}}\mathbf{F}^T|_{\mathbf{x}}$ is the evaluation of the Cauchy stress at the material point $\mathbf{x}$ from the macro-scale, expression (80) leads us to the homogenisation rule of the macro-scale Cauchy stress

$$\boldsymbol{\sigma}_m|_{\mathbf{x}} = \frac{1}{\det \mathbf{F}|_{\mathbf{x}}|\Omega_\mu|}\sum_{\alpha\in\mathcal{F}_{net}} V_\alpha(\mathbf{s}^\alpha_\mu \otimes \mathbf{F}|_{\mathbf{x}}\mathbf{a}^\alpha). \tag{81}$$

Remark 20 (*Incompressible Case*)**.** In this case, expressions (77) and (80) turn into

$$\left(\mathbf{P}^{\mathsf{iso}}|_{\mathbf{x}} - \mathcal{H}_{\mathbf{P}}(\mathbb{S}^F_\mu)\right)\cdot \hat{\mathbf{G}}|_{\mathbf{x}} = 0 \quad \forall \hat{\mathbf{G}}|_{\mathbf{x}} \in \mathbb{T}_{\mathsf{inc}}. \tag{82}$$

Using classical tensor identities[8] and noting that $\mathbf{F}|_{\mathbf{x}}$ is invertible, we have that condition (82) is equivalent to

$$\left(\mathbf{P}^{\mathsf{iso}}|_{\mathbf{x}} - \mathcal{H}_{\mathbf{P}}(\mathbb{S}^F_\mu)\right)\mathbf{F}^T|_{\mathbf{x}}\cdot \hat{\mathbf{G}}|_{\mathbf{x}}\mathbf{F}^{-1}|_{\mathbf{x}} = 0 \quad \forall \hat{\mathbf{G}}|_{\mathbf{x}} \in \mathbb{T}_{\mathsf{inc}}, \tag{83}$$

but, since $\mathrm{tr}(\hat{\mathbf{G}}|_{\mathbf{x}}\mathbf{F}^{-1}|_{\mathbf{x}}) = 0$, it results

$$\left(\mathbf{P}^{\mathsf{iso}}|_{\mathbf{x}} - \mathcal{H}_{\mathbf{P}}(\mathbb{S}^F_\mu)\right)\mathbf{F}^T|_{\mathbf{x}} = \beta\mathbf{I}, \tag{84}$$

with $\beta \in \mathbb{R}$. Hence $\mathbf{P}^{\mathsf{iso}}|_{\mathbf{x}}$ is of the form

$$\mathbf{P}^{\mathsf{iso}}|_{\mathbf{x}} = \mathcal{H}_{\mathbf{P}}(\mathbb{S}^F_\mu) + \beta\mathbf{F}^{-T}|_{\mathbf{x}}. \tag{85}$$

Taking β such that $\mathrm{tr}\left(\frac{1}{\det \mathbf{F}|_{\mathbf{x}}}\mathbf{P}^{\mathsf{iso}}|_{\mathbf{x}}\mathbf{F}^T|_{\mathbf{x}}\right) = 0$ (see Remark 19) we have

$$\beta = -\frac{1}{\mathrm{n_d}}\mathrm{tr}(\mathcal{H}_{\mathbf{P}}(\mathbb{S}^F_\mu)\mathbf{F}^T|_{\mathbf{x}}) = -\frac{1}{\mathrm{n_d}}\mathcal{H}_{\mathbf{P}}(\mathbb{S}^F_\mu)\cdot \mathbf{F}|_{\mathbf{x}}, \tag{86}$$

which replaced in (85) becomes

$$\begin{aligned}\mathbf{P}^{\mathsf{iso}}|_{\mathbf{x}} &= \mathcal{H}_{\mathbf{P}}(\mathbb{S}^F_\mu) - \frac{1}{\mathrm{n_d}}\left(\mathcal{H}_{\mathbf{P}}(\mathbb{S}^F_\mu)\cdot \mathbf{F}|_{\mathbf{x}}\right)\mathbf{F}^{-T}|_{\mathbf{x}}\\ &= \mathcal{H}_{\mathbf{P}}(\mathbb{S}^F_\mu) - \frac{1}{\mathrm{n_d}}(\mathbf{F}^{-T}|_{\mathbf{x}} \otimes \mathbf{F}|_{\mathbf{x}})\mathcal{H}_{\mathbf{P}}(\mathbb{S}^F_\mu).\end{aligned} \tag{87}$$

[8] For any $\mathbf{A}_1$, $\mathbf{A}_2$ and $\mathbf{A}_3$ second order tensors the following identity holds: $\mathbf{A}_1\cdot\mathbf{A}_2\mathbf{A}_3 = \mathbf{A}_1\mathbf{A}_3^T\cdot\mathbf{A}_2$.

Finally, defining the fourth order tensor

$$\mathbb{T}^{\mathsf{iso}}|_{\mathbf{x}} = \mathbb{I} - \frac{1}{\mathrm{n_d}}\mathbf{F}^{-T}|_{\mathbf{x}} \otimes \mathbf{F}|_{\mathbf{x}}, \tag{88}$$

with $\mathbb{I}$ being fourth-order identity tensor, we have the isochoric part of the stress given by

$$\mathbf{P}^{\mathsf{iso}}|_{\mathbf{x}} = \mathcal{H}^{\mathsf{iso}}_{\mathbf{P}}(\mathbb{S}^F_\mu) = \mathbb{T}^{\mathsf{iso}}|_{\mathbf{x}}\mathcal{H}_{\mathbf{P}}(\mathbb{S}^F_\mu). \tag{89}$$

We highlight that the only difference between (80) and (89) is the pre-multiplication of the projection isochoric tensor in the former homogenisation formula. Moreover, by construction the homogenised Piola–Kirchhoff macro-scale stress tensor in the incompressible case, transformed into the corresponding Cauchy stress, features null trace.

6.2. Micro-scale mechanical equilibrium problem

Now, taking $\hat{\mathbf{G}}|_{\mathbf{x}} = \mathbf{O}$ in (73) yields

$$\sum_{\alpha\in\mathcal{F}_{net}} V_\alpha \mathbf{S}^\alpha_\mu \cdot \left(\frac{1}{L_\alpha}\Delta^\alpha\hat{\tilde{\mathbb{U}}}_\mu \otimes \mathbf{a}^\alpha\right) = \sum_{\alpha\in\mathcal{F}_{net}} A_\alpha(\mathbf{S}^\alpha_\mu\mathbf{a}^\alpha)\cdot\Delta^\alpha\hat{\tilde{\mathbb{U}}}_\mu = \sum_{\alpha\in\mathcal{F}_{net}} A_\alpha\mathbf{s}^\alpha_\mu\cdot\Delta^\alpha\hat{\tilde{\mathbb{U}}}_\mu = 0 \quad \forall\hat{\tilde{\mathbb{U}}}_\mu \in \widetilde{\mathscr{U}}_\mu. \tag{90}$$

Consequently we have the following problem to be solved at the RVE.

Problem 3 (*Micro-scale Mechanical Equilibrium*)**.** Given $\mathbf{G}|_{\mathbf{x}} \in \mathbb{R}^{\mathrm{n_d}\times\mathrm{n_d}}$, find $\tilde{\mathbb{U}}_\mu \in \widetilde{\mathscr{U}}_\mu$ such that the stress vector $\{\mathbf{s}^\alpha_\mu\}_{\alpha\in\mathcal{F}_{net}}$ is such that the following variational equation holds

$$\sum_{\alpha\in\mathcal{F}_{net}} A_\alpha\mathbf{s}^\alpha_\mu\cdot\Delta^\alpha\hat{\tilde{\mathbb{U}}}_\mu = 0 \quad \forall\hat{\tilde{\mathbb{U}}}_\mu \in \widetilde{\mathscr{U}}_\mu, \tag{91}$$

where $\mathbf{s}^\alpha_\mu$ is related to $\mathbf{G}^\alpha_\mu = \mathbf{G}|_{\mathbf{x}}\mathbf{a}^\alpha\otimes\mathbf{a}^\alpha + \frac{1}{L_\alpha}\Delta^\alpha\tilde{\mathbb{U}}_\mu\otimes\mathbf{a}^\alpha$ through a micro-scale constitutive functional of the form $\mathbf{s}^\alpha_\mu = \mathscr{F}^\alpha_\mu(\mathbf{G}^\alpha_\mu)$.

Remark 21 (*Incompressible Case*)**.** It is the same that Problem 3 but with $\mathbf{G}|_{\mathbf{x}} \in \mathbb{M}_{\mathsf{inc}} \subset \mathbb{R}^{\mathrm{n_d}\times\mathrm{n_d}}$.

Once Problem 3 is solved, the evaluation of the micro-scale fibre stresses is straightforward, from which the homogenisation of the macro-scale Piola–Kirchhoff stress tensor follows directly using (80).

In practice, constitutive and geometrical nonlinearities present in variational equation (91) can be addressed using the classical Newton–Raphson linearisation strategy. We omit the details here for the sake of brevity.

The kinematical constraints in $\widetilde{\mathscr{U}}_\mu$ (see (47) and (60)) are imposed using the saddle point problem associated to (91) in which Lagrange multipliers are added to relax such constraints. This is detailed in Section 7.

Finally, in Section 8 we discuss physical and implementation aspects for the constitutive laws provided for the micro-scale problem.

Remark 22. The Variational formulation (91) for the micro-scale problem is the classical problem of nonlinear trusses connected at end points with the exception of the specific constraints in the spaces of admissible functions. A standard approach to this problem is presented in [49, Chapter 9], where elemental stiffness matrices and residual vectors are derived in a reference frame aligned with the truss, and then properly rotated to assemble them in the global system of equations. The present formulation is absolutely equivalent to such classical formulation (proof omitted for the sake of brevity). The difference is that in the present work a global reference frame has been employed, which is advantageous to deal more directly with the kinematical constraints imposed by the kinematic coupling between scales.

7. On the kinematical constraints and reactive forces

In this section we aim to rewrite Problem 3 relaxing the constrains in space $\widetilde{\mathscr{U}}_\mu$ through the introduction of Lagrange multipliers. So, we have the following problem.

Problem 4 (*Lagrange Multiplier Formulation for the RVE Problem*)**.** Given $\mathbf{G}|_{\mathbf{x}} \in \mathbb{R}^{\mathrm{n_d}\times\mathrm{n_d}}$, find $(\tilde{\mathbb{U}}_\mu, \boldsymbol{\Lambda}, \boldsymbol{\Theta}) \in \mathscr{U}_\mu \times \mathbb{R}^{\mathrm{n_d}\times\mathrm{n_d}} \times \mathbb{R}^{\mathrm{n_d}}$ such that

$$\begin{aligned}
&\sum_{\alpha\in\mathcal{F}_{net}} A_\alpha \mathbf{s}_\mu^\alpha \cdot \Delta^\alpha \hat{\tilde{\mathbb{U}}}_\mu - \boldsymbol{\Lambda}\cdot\left(\sum_{i\in\mathcal{N}_{net}^\Gamma} \bar{A}_i \hat{\tilde{\mathbf{u}}}_\mu^i \otimes (\mathbf{n}_i - \bar{\mathbf{n}})\right) - \hat{\boldsymbol{\Lambda}}\cdot\left(\sum_{i\in\mathcal{N}_{net}^\Gamma} \bar{A}_i \tilde{\mathbf{u}}_\mu^i \otimes (\mathbf{n}_i - \bar{\mathbf{n}})\right)\\
&\quad + \boldsymbol{\Theta}\cdot\left(\sum_{\alpha\in\mathcal{F}_{net}} \frac{V_\alpha}{2}(\hat{\tilde{\mathbf{u}}}_\mu^{i_\alpha} + \hat{\tilde{\mathbf{u}}}_\mu^{j_\alpha})\right) + \hat{\boldsymbol{\Theta}}\cdot\left(\sum_{\alpha\in\mathcal{F}_{net}} \frac{V_\alpha}{2}(\tilde{\mathbf{u}}_\mu^{i_\alpha} + \tilde{\mathbf{u}}_\mu^{j_\alpha})\right) = 0\\
&\quad \forall(\hat{\tilde{\mathbb{U}}}_\mu, \hat{\boldsymbol{\Lambda}}, \hat{\boldsymbol{\Theta}}) \in \mathscr{U}_\mu \times \mathbb{R}^{\mathrm{n_d}\times\mathrm{n_d}} \times \mathbb{R}^{\mathrm{n_d}},
\end{aligned} \tag{92}$$

where $\mathbf{s}_\mu^\alpha = \mathscr{F}_\mu^\alpha(\mathbf{G}_\mu^\alpha)$, with $\mathbf{G}_\mu^\alpha = \mathbf{G}|_{\mathbf{x}}\mathbf{a}^\alpha \otimes \mathbf{a}^\alpha + \frac{1}{L_\alpha}\Delta^\alpha\tilde{\mathbb{U}}_\mu \otimes \mathbf{a}^\alpha$.

First, taking $\hat{\tilde{\mathbb{U}}}_\mu = \mathbb{O}$ and $\hat{\boldsymbol{\Theta}} = \mathbf{0}$ in (92) we retrieve, now as a natural consequence of the variational equation, the kinematical restriction (63), which is equivalent to $\mathcal{H}_\mu^{\mathscr{E}}(\mathcal{D}_\mu(\tilde{\mathbb{U}}_\mu)) = \mathbf{O}$. Secondly, taking $\hat{\tilde{\mathbb{U}}}_\mu = \mathbb{O}$ and $\hat{\boldsymbol{\Lambda}} = \mathbf{O}$ we arrive to (49), i.e, $\mathcal{H}_\mu^{\mathscr{U}}(\tilde{\mathbb{U}}_\mu) = \mathbf{0}$. Thirdly, taking $\hat{\boldsymbol{\Lambda}} = \mathbf{O}$ and $\hat{\boldsymbol{\Theta}} = \mathbf{0}$, it results

$$\begin{aligned}
&\sum_{\alpha\in\mathcal{F}_{net}} A_\alpha \mathbf{s}_\mu^\alpha \cdot \Delta^\alpha \hat{\tilde{\mathbb{U}}}_\mu - \boldsymbol{\Lambda}\cdot\left(\sum_{i\in\mathcal{N}_{net}^\Gamma} \bar{A}_i \hat{\tilde{\mathbf{u}}}_\mu^i \otimes (\mathbf{n}_i - \bar{\mathbf{n}})\right)\\
&\quad + \boldsymbol{\Theta}\cdot\left(\sum_{\alpha\in\mathcal{F}_{net}} \frac{V_\alpha}{2}(\hat{\tilde{\mathbf{u}}}_\mu^{i_\alpha} + \hat{\tilde{\mathbf{u}}}_\mu^{j_\alpha})\right) = 0 \qquad \forall\hat{\tilde{\mathbb{U}}}_\mu \in \mathscr{U}_\mu.
\end{aligned} \tag{93}$$

In particular, expression (93) is valid for $\hat{\tilde{\mathbb{U}}}_\mu = \mathbb{C}$ (an uniform fluctuation field, i.e., $\hat{\tilde{\mathbf{u}}}_\mu^i = \mathbf{c}, \forall i \in \mathcal{N}_{net}$). After some manipulation we have

$$\left(-\boldsymbol{\Lambda}\left(\sum_{i\in\mathcal{N}_{net}^\Gamma} \bar{A}_i(\mathbf{n}_i - \bar{\mathbf{n}})\right) + |\mathcal{F}_{net}|\,\boldsymbol{\Theta}\right)\cdot\mathbf{c} = 0, \tag{94}$$

and by the fact that $\mathbf{c}$ is arbitrary and using the definition of $\bar{\mathbf{n}}$ in (59), we arrive at

$$\boldsymbol{\Theta} = \boldsymbol{\Lambda}\left(\frac{1}{|\mathcal{F}_{net}|}\sum_{i\in\mathcal{N}_{net}^\Gamma} \bar{A}_i(\mathbf{n}_i - \bar{\mathbf{n}})\right) = \mathbf{0}. \tag{95}$$

Remark 23. By construction of (95) the reactive force $\boldsymbol{\Theta}$ is zero. Therefore, from (98) the forces per unit area over the RVE boundary are self-equilibrated.

Finally, rewriting (93) by taking into account (19) and (95) and splitting summations into interior and boundary nodes we have

$$\begin{aligned}
&\sum_{i\in\mathcal{N}_{net}^\Gamma}\left(\left(\sum_{\alpha\in\mathcal{F}_{net}^i}[\alpha, i]A_\alpha\mathbf{s}_\mu^\alpha\right) - \bar{A}_i\boldsymbol{\Lambda}(\mathbf{n}_i - \bar{\mathbf{n}})\right)\cdot\hat{\tilde{\mathbf{u}}}_\mu^i +\\
&\quad\sum_{i\in\mathring{\mathcal{N}}_{net}}\left(\sum_{\alpha\in\mathcal{F}_{net}^i}[\alpha, i]A_\alpha\mathbf{s}_\mu^\alpha\right)\cdot\hat{\tilde{\mathbf{u}}}_\mu^i = 0 \quad \forall\hat{\tilde{\mathbb{U}}}_\mu \in \mathscr{U}_\mu.
\end{aligned} \tag{96}$$

This leads to the Euler–Lagrange equations

$$\sum_{\alpha\in\mathcal{F}_{net}^i}[\alpha, i]A_\alpha\mathbf{s}_\mu^\alpha = \mathbf{0} \qquad \forall i \in \mathring{\mathcal{N}}_{net}, \tag{97}$$

$$\sum_{\alpha\in\mathcal{F}_{net}^i}[\alpha, i]A_\alpha\mathbf{s}_\mu^\alpha = \bar{A}_i\boldsymbol{\Lambda}(\mathbf{n}_i - \bar{\mathbf{n}}) \qquad \forall i \in \mathcal{N}_{net}^\Gamma. \tag{98}$$

The first equation expresses the equilibrium of fibre forces at each interior node. The second equation stands for the equilibrium between forces at the nodes over the RVE boundary. This equilibrium is satisfied by the summation of

fibre forces $[\alpha, i]A_\alpha \mathbf{s}^\alpha_\mu$, $\alpha \in \mathcal{F}^i_{net}$, and by the reactive force $\bar{A}_i \boldsymbol{\Lambda}(\mathbf{n}_i - \bar{\mathbf{n}})$ (usually acknowledged as a uniform traction). This later expression also gives a first physical interpretation for the Lagrange multiplier $\boldsymbol{\Lambda}$.[9] In fact, the total force (traction $\mathbf{t}_i = \bar{A}_i \boldsymbol{\Lambda}(\mathbf{n}_i - \bar{\mathbf{n}})$) supported by the bars reaching the boundary node $i \in \mathcal{N}^\Gamma_{net}$ depends on the constant second-order tensor $\boldsymbol{\Lambda}$ and the difference between the unitary outward normal vector of the RVE and the average normal vector.

Remark 24 (*Continuum Case*)**.** We can understand the Euler–Lagrange equations (97)–(98) as discrete counterparts of the classical formulation in strong form (partial differential equations form) which read $\operatorname{div} \boldsymbol{\sigma} = \mathbf{0}$, in B and $\boldsymbol{\sigma}\mathbf{n} = \bar{\mathbf{t}}$ on ∂B_N, where $B \subset \mathbb{R}^{\mathrm{n_d}}$ is the body domain, $\boldsymbol{\sigma}$ is the Cauchy stress tensor and $\bar{\mathbf{t}}$ is a prescribed traction vector on the Neumann boundary ∂B_N.

7.1. Alternatives expressions for the stress homogenisation

We focus now on finding an alternative expression for the homogenisation of the stress tensor depending only on boundary data. As an additional consequence an alternative physical interpretation for the Lagrange Multiplier $\boldsymbol{\Lambda}$ will also be achieved.

As (98) is valid for all boundary nodes, let us call $\bar{A}_i \boldsymbol{\Lambda}(\mathbf{n}_i - \bar{\mathbf{n}}) = \mathbf{t}_i$ (traction) and consider the summation over $i \in \mathcal{N}^\Gamma_{net}$ as follows

$$
\begin{aligned}
&\sum_{i \in \mathcal{N}^\Gamma_{net}} \left(\bar{A}_i \boldsymbol{\Lambda}(\mathbf{n}_i - \bar{\mathbf{n}})\right) \otimes (\mathbf{y}^i - \mathbf{y}^G) = \sum_{i \in \mathcal{N}^\Gamma_{net}} \mathbf{t}_i \otimes (\mathbf{y}^i - \mathbf{y}^G) = \\
&\quad \sum_{i \in \mathcal{N}^\Gamma_{net}} \left(\sum_{\alpha \in \mathcal{F}^i_{net}} [\alpha, i] A_\alpha \mathbf{s}^\alpha_\mu \right) \otimes (\mathbf{y}^i - \mathbf{y}^G) + \\
&\quad \sum_{i \in \mathring{\mathcal{N}}_{net}} \underbrace{\left(\sum_{\alpha \in \mathcal{F}^i_{net}} [\alpha, i] A_\alpha \mathbf{s}^\alpha_\mu \right)}_{=\mathbf{0} \text{ from (97)}} \otimes (\mathbf{y}^i - \mathbf{y}^G) = \\
&\quad \sum_{i \in \mathcal{N}_{net}} \sum_{\alpha \in \mathcal{F}^i_{net}} [\alpha, i] A_\alpha \mathbf{s}^\alpha \otimes (\mathbf{y}^i - \mathbf{y}^G) = \\
&\quad \sum_{\alpha \in \mathcal{F}_{net}} A_\alpha \mathbf{s}^\alpha \otimes \Delta^\alpha \mathbf{y} = \sum_{\alpha \in \mathcal{F}_{net}} V_\alpha \mathbf{s}^\alpha \otimes \mathbf{a}^\alpha = |\Omega_\mu| \mathbf{P}|_{\mathbf{x}},
\end{aligned}
\tag{99}
$$

where we have also made use of (19) and (20). From the development in (99), before adding the summation over internal nodes, we have that $\mathbf{P}|_{\mathbf{x}}$ depends only on boundary information, that is

$$
\mathbf{P}|_{\mathbf{x}} = \frac{1}{|\Omega_\mu|} \sum_{i \in \mathcal{N}^\Gamma_{net}} \mathbf{t}_i \otimes (\mathbf{y}^i - \mathbf{y}^G). \tag{100}
$$

This is an alternative form of the homogenisation formula derived in (80). Now, define the auxiliary tensor

$$
\mathbf{B}^\Gamma := \frac{1}{|\Omega_\mu|} \sum_{i \in \mathcal{N}^\Gamma_{net}} \bar{A}_i (\mathbf{n}_i - \bar{\mathbf{n}}) \otimes (\mathbf{y}^i - \mathbf{y}^G). \tag{101}
$$

With (101) into (99), and since $\boldsymbol{\Lambda}$ is a constant tensor, we have

$$
|\Omega_\mu| \boldsymbol{\Lambda} \mathbf{B}^\Gamma = |\Omega_\mu| \mathbf{P}|_{\mathbf{x}}, \tag{102}
$$

which leads us to conclude that

$$
\boldsymbol{\Lambda} = \mathbf{P}|_{\mathbf{x}} (\mathbf{B}^\Gamma)^{-1}. \tag{103}
$$

This establishes that the reactive generalised force due to the imposition of the minimum kinematical constraint of the space $\widetilde{\mathscr{U}}^{\mathsf{M}}_\mu$ is in direct connection with the homogenised stress tensor.

[9] Connection between $\boldsymbol{\Lambda}$ and the homogenised stress tensor $\mathbf{P}$ is addressed in Section 7.1.

Remark 25 (*Continuum Case*)**.** The homogenisation for stress given by (100) is completely equivalent to that derived in (80). The former can be understood as the discrete counterpart of the well known homogenisation formula for stress based on boundary data in classical continuum mechanics that reads (see [39])

$$\mathbf{P}|_{\mathbf{x}} = \frac{1}{|B_\mu|}\int_{\partial B_\mu} \mathbf{t}\otimes(\mathbf{y}-\mathbf{y}_G)\,\mathrm{d}\partial B_\mu, \tag{104}$$

where B_μ is the RVE domain, with boundary ∂B_μ, and $\mathbf{t}$ is the traction vector over the boundary.

In turn, in the continuum limit and without pores on boundary, the tensor defined in (101) is

$$\frac{1}{|B_\mu|}\int_{\partial B_\mu} \mathbf{n}\otimes(\mathbf{y}-\mathbf{y}_G)\,\mathrm{d}\partial B_\mu = \frac{1}{|B_\mu|}\left(\int_{\partial B_\mu}\nabla(\mathbf{y}-\mathbf{y}_G)\,\mathrm{d}\partial B_\mu\right)^T = \mathbf{I}, \tag{105}$$

where the divergence theorem was used. This fact suggests that in such situation the Lagrange multiplier associated to the imposition of the minimum kinematical restriction has exactly the meaning of the first Piola–Kirchhoff stress tensor, i.e, expression (103) in the continuum becomes $\boldsymbol{\Lambda} = \mathbf{P}|_{\mathbf{x}}$.

Remark 26. From a purely geometrical perspective, the well-posedness of the present multi-scale formulation is inherently built upon the fact that $\mathbf{B}$ and $\mathbf{B}^\Gamma$, defined in (55) and (101) respectively, are non-singular second order tensors.

8. Constitutive equations

This section discusses the most relevant constitutive aspects of a *fibre* (more precisely, of a bundle of collagen fibres). For the sake of simplicity, dissipative effects such as damage or viscoelasticity are neglected. See [50,51] for the consideration of these phenomena.

It is well-known in the biomechanics field (e.g. [50,52] and references therein) that collagen molecules are packed in form of collagen fibrils, which, in turn, aggregate to form collagen fibres. Collagen fibres are arranged in distinct and parallel bundles (also called fascicles), which are, in general, wavily deposited in a load-free state. This scale can be visualised in Fig. 6 for a fibre bundle $\alpha \in \mathcal{F}_{net}$, where L_α is the length of an imaginary cylinder embracing fibres featuring similar waviness and directions. When this cylinder is stretched up to a length ℓ^a_α, the fibres align and start bearing axial load. This defines the *activation stretch* (also called *recruitment stretch*) as the ratio:

$$\lambda^a_\alpha = \frac{\ell^a_\alpha}{L_\alpha}. \tag{106}$$

The focus of the present contribution is at the scale of the network of fibre bundles, while the detailed description of smaller scales, ranging from collagen molecules up to bundle of fibres is out of scope of this contribution. In the present context, let us admit that for a given $\alpha \in \mathcal{F}_{net}$ the strain energy associated to the bundle can be characterised by an elastic parameter c^α_1 and the already defined λ^a_α as in [53][10]:

$$\Psi^\mu_\alpha(\lambda_\alpha) = \begin{cases} c^\alpha_1\left(\lambda^2_\alpha - (\lambda^a_\alpha)^2\right)^2 & \text{if } \lambda_\alpha > \lambda^a_\alpha, \\ 0 & \text{if } \lambda_\alpha \le \lambda^a_\alpha. \end{cases} \tag{107}$$

As usual, the stress $\mathbf{S}^\alpha_\mu$ is derived from strain energy as follows

$$\mathbf{S}^\alpha_\mu(\mathbf{G}^\alpha_\mu) = \frac{\partial\,\Psi^\mu_\alpha(\lambda_\alpha(\mathbf{G}^\alpha_\mu))}{\partial\mathbf{G}^\alpha_\mu}, \tag{108}$$

where the derivative can be determined by the chain rule, knowing that

$$\lambda^2_\alpha = [(\mathbf{I}+\mathbf{G}^\alpha_\mu)\mathbf{a}^\alpha]\cdot[(\mathbf{I}+\mathbf{G}^\alpha_\mu)\mathbf{a}^\alpha]. \tag{109}$$

Finally, for a standard Newton–Raphson linearisation procedure, we need to compute the tangent tensor as $\mathbb{D}^\alpha_\mu = \frac{\partial\mathbf{S}^\alpha_\mu}{\partial\mathbf{G}^\alpha_\mu}$.

At this point it is important to highlight that c^α_1 and λ^a_α have to be understood as homogenised quantities which arise from smaller spatial length scales. We also note that the stress derived from this energy function is non-linear

[10] The term $(\lambda^a_\alpha)^2$ is analogous to the invariant I_4 defined for transversally isotropic materials and the energy is equal to the first nonzero term of the Taylor expansion for the exponential model evaluated at $(\lambda_\alpha)^2 = (\lambda^a_\alpha)^2$ (see [1] for example).

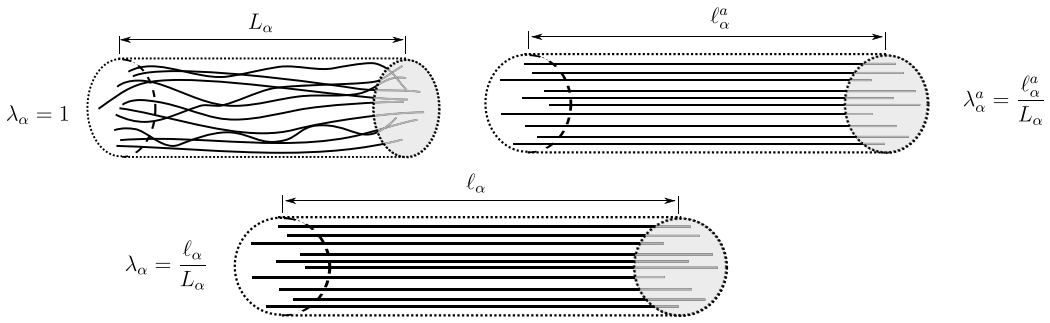

Fig. 6. Imaginary cylinder (truss) in different deformed configurations enclosing a bundle of collagen fibres.

with respect to the stretch λ_α (but it is less steep than exponential models [2]). It is believed that such nonlinearity, emerges from geometrical characteristic of collagen fibres (tortuosity) and from the fact that bending phenomena are neglected (see [54], where assuming a sinusoidal shape for the fibre leads to an analytical expression for the axial stress under tension). Another source of nonlinearity comes from the progressive fibre activations taking place within the bundle [50]. An analogous effect, but at the scale of the network, will be investigated in Section 9.1.3, where we will be able to reproduce a similar result as a consequence of the heterogeneities in the definition of λ^a_α among the fibres of the network.

Finally, it is important to mention that Chandran and Barocas [8] reported that the qualitative network behaviour is largely independent from the constitutive equation assigned to individual fibres. Furthermore in physiological ranges of stretches caused by arterial pressure, most of fibre bundles act on tension [12]. Thus, it is expected that even when picking a relatively simple constitutive model for individual fibres several important features of the multi-scale model are manifested.

9. Numerical experiments

In this section we investigate the constitutive behaviour of fibrous specimens as predicted by the proposed multi-scale model particularly in the presence of heterogeneities along the network. We report simulations in two-dimensional and three-dimensional settings, in Sections 9.1 and 9.2, respectively.

9.1. Simulations in a two-dimensional setting

More precisely in the two-dimensional context, by heterogeneities we mean any kind of deviation from a homogeneous network (as in Fig. 7). In a homogeneous network, fibres associated to the same family set have the same properties, i.e. (i) the same fibre orientation θ (associated to $\mathbf{a}^\alpha$), (ii) the same length, (iii) the same area, A, and (iv) the same activation stretch λ^a.[11] In particular we will term *X-heterogeneous network*, the fibrous RVE, obtained from a homogeneous network, whenever property X has lost its homogeneity character, where $X \in \{\theta, A, \lambda^a\}$. Cases in which two properties become heterogeneous the notation becomes *X_1X_2-heterogeneous network*, with $X_1, X_2 \in \{\theta, A, \lambda^a\}$.

It is important to note that, in the field of materials science, any network of fibres is naturally a heterogeneous media, and particularly anisotropic due to the intrinsic preferred directional distribution of the properties in the RVE domain. Therefore, the characterisation employed here for a network as homogeneous (heterogeneous) must not be confused with the classical concept of homogeneous (heterogeneous) material.

In this context, several realisations of fibrous RVEs are generated and compared for different spaces of kinematically admissible fluctuation fields, specifically for the minimally constrained space $\widetilde{\mathscr{U}}^{\mathsf{M}}_\mu$ (see (64)) and for the linear displacement space $\widetilde{\mathscr{U}}^{\mathsf{L}}_\mu$ (see (66)).

[11] For sake of simplicity, λ^a is the only source of heterogeneity in the constitutive response of individual fibres since c_1 is kept constant in the strain energy (107) for all fibres.

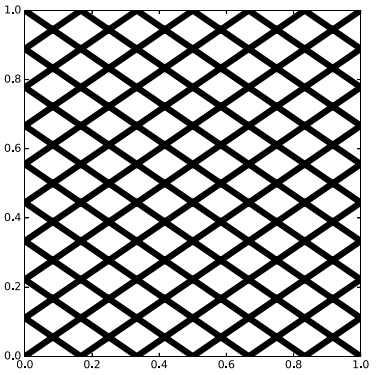

Fig. 7. Example of homogeneous network.

The generation of the fibrous networks, together with the definition of the properties is outlined in Section 9.1.1. As it will be seen, the aim of this kind of study is to analyse the sensitivity of the constitutive response to such heterogeneities as well as the sensitivity to the choice of boundary conditions for the RVE.

In order to quantify the impact of topological and material RVE heterogeneities in the solution of the micro-scale equilibrium problem, a measure of the non-affinity of the fluctuation field is proposed, called *non-affinity index*, as follows

$$I_{\mathrm{NA}} := \frac{1}{|\mathcal{F}_{net}|} \sum_{\alpha \in \mathcal{F}_{net}} \frac{V_\alpha}{2} (\|\tilde{\mathbf{u}}_\mu^{i_\alpha}\| + \|\tilde{\mathbf{u}}_\mu^{j_\alpha}\|), \tag{110}$$

where V_α is the volume of fibre α and $|\mathcal{F}_{net}|$ is the volume of all fibres.

9.1.1. Random generation of fibrous networks

The network of fibres is computationally generated by providing a set of target properties. Initially, for a given average fibre orientation, say θ, (measured from x-axis) and for a certain number of fibres n_{fib}, a homogeneous network is generated containing two families of fibres symmetrically oriented, as in the example shown in Fig. 7. As already said, crossing-points are junctions, which are the extremes of computational fibres.

In a second stage, the position of each node is individually perturbed in a random magnitude and direction. The maximum perturbation is limited by a given number $\delta_{\max}$. As outcome, we obtain the networks illustrated in Fig. 8 (second row) for two different values of $\delta_{\max}$. This kind of alteration in the network will render the irregularities in the fibre orientations and lengths. Since orientations are relatively more affected than fibre lengths, in what follows we simply refer to it as θ-heterogeneity.

The two other sources of geometrical and material heterogeneities are in the choice of fibre areas and activation stretches, also called A-heterogeneity and λ^a-heterogeneity respectively. These values are taken from probability distributions with mean value m_A (m_{λ^a}) and standard deviation s_A (s_{λ^a}) for fibre area (activation stretch). Specifically, for the case of heterogeneous activation stretches, the deviation from the unit value was assumed to follow a Gamma-distribution,[12] as suggested experimentally by the work of Hill et al. [56]. In turn, the fibre area is assumed to be normally distributed with negative values disregarded.

For convenience, let us recall the most important parameters that define the characteristics of a certain realisation of a network (i.e. a random generation of the network). The set of parameters is: θ, n_{fib}, $\delta_{\max}$, m_A, s_A, m_{λ^a}, s_{λ^a}, and will be defined for all the examples presented below.

When referring to numerical examples, the characteristics that govern the randomness of the network generation, such as $\delta_{\max}$ or s_A, for example, are denoted by $p^{l,k}$ meaning that the kth realisation of the network was generated with level l for the property p. The k value acts as a label of the initialisation of the pseudo-random number generator. That is, we may have different values of k for the same level l, which means that different realisations were taken from the

[12] From [55] the pdf of the Gamma-distribution is defined as $f_{\alpha,\beta}(x) = (\beta^\alpha/\Gamma(\alpha))x^{\alpha-1}e^{-\beta x}$ for $x > 0$ (zero otherwise), with expected value and variance only function of the two parameters $\alpha > 0$ and $\beta > 0$. Given the values of m_{λ^a} and s_{λ^a} we have $\alpha = (m_{\lambda^a}/s_{\lambda^a})^2$ and $\beta = m_{\lambda^a}/(s_{\lambda^a})^2$.

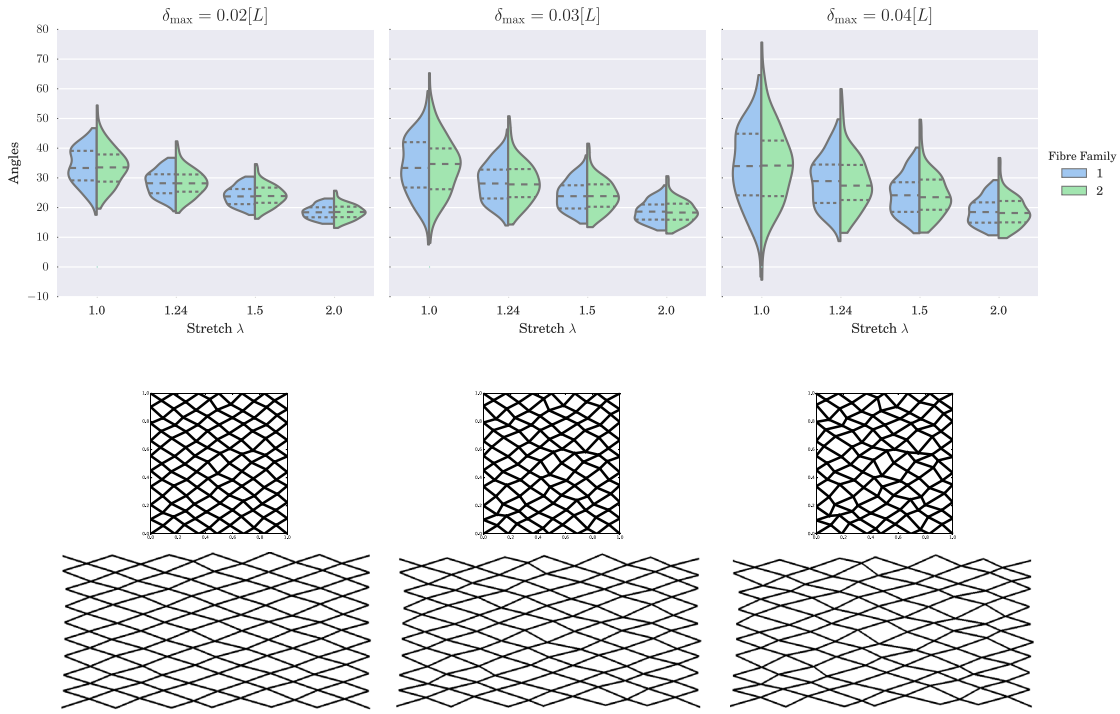

Fig. 8. Reorientation of fibre families considering different fibre orientation angles due to three different node perturbations (realisations for a fixed random seed value). Angle distribution as a function of the macro-scale stretch (top row) and disposition of fibres in the original (mid row) and deformed network at the maximum level of stretch $\lambda = 2.0$ (bottom row).

Table 1
Network parameters to study the effect of fibre area and orientation.

All Realisations	θ 33.69°	n_{fib} 216	m_{λ^a} 1.0	s_{λ^a} 0.0
Levels[a] $s_A[L^2]$	l_1 0.002	l_2 0.004	l_3 0.006	$\delta_{max} = 0.0[L]$
Levels[a] $\delta_{max}[L]$	l_1 0.002	l_2 0.004	l_3 0.006	$s_A = 0.0[L^2]$

[a] For each level, 3 realisations are considered.

same value of property. In addition, it is possible to have different levels l for the kth realisation, which means that the deviations are magnified but the random pattern remains the same.

9.1.2. Effect of fibre area and fibre orientation

In this section we test the effect of two sources of heterogeneities separately, namely: fibre area and fibre orientation. In order to assess the impact of each parameter, 18 network realisations were generated by the procedure described in Section 9.1.1. Within this set, 9 networks feature heterogeneous fibre area and have a homogeneous fibre orientation, similar to Fig. 7. The remaining 9 networks have heterogeneous fibre orientation, and constant fibre area, for which some realisations representing different levels of node perturbation are found in Fig. 8 (second row). Parameters that control the heterogeneities are the area standard deviation s_A and the node perturbation δ_{max}, which where equal to three different levels with 3 realisations each, as summarised in Table 1.

The constitutive behaviour of single fibres at the micro-scale is characterised by the strain energy function (107), with parameter $c_1^{\alpha} = 900[F/L^2]$ constant for all fibres. A progressive stretch in the horizontal direction was applied

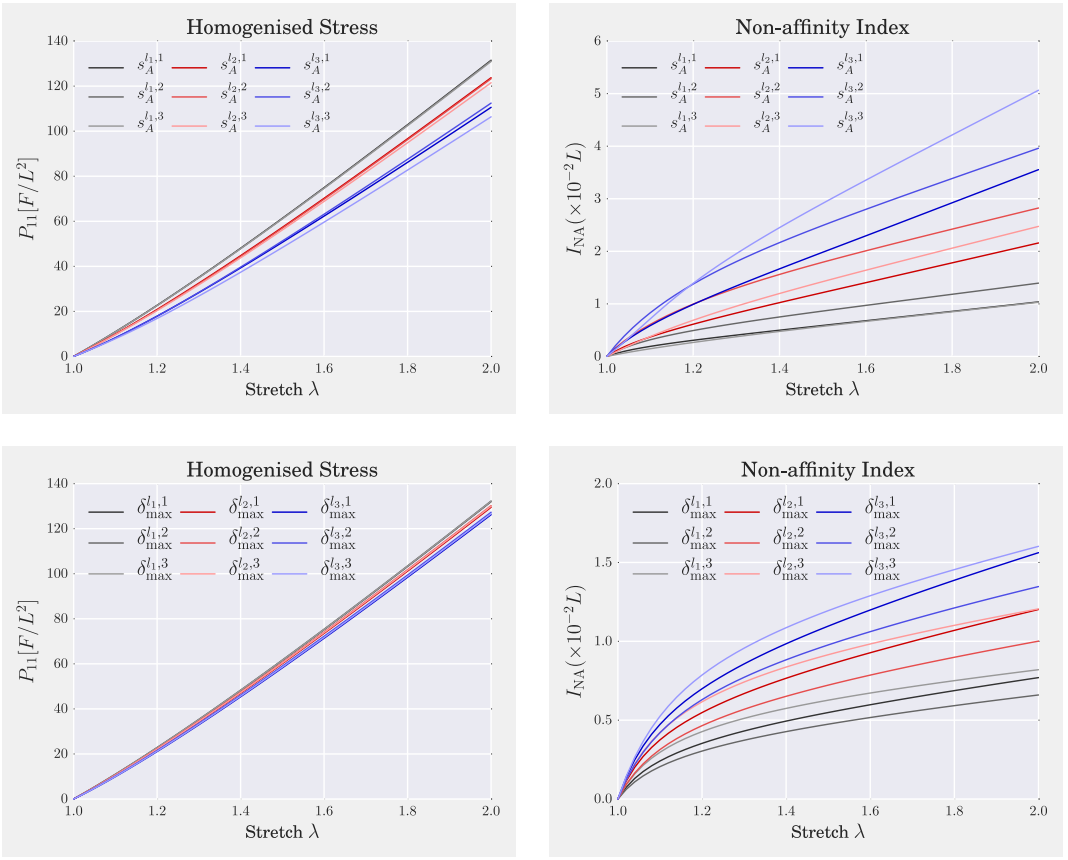

Fig. 9. Homogenised constitutive response (left column) and non-affinity index (right column) considering fibre area variation (top row) and fibre orientation (bottom row).

with macro-scale gradient given by

$$\mathbf{G}_t = \begin{bmatrix} t & 0 \\ 0 & 0 \end{bmatrix}, \tag{111}$$

where t is a parameter in the range [0, 1] that increases linearly and monotonically through 50 load steps.

Fig. 9, on the left column, shows the dominant component of the first Piola–Kirchhoff stress tensor (P_{11}, from $\mathbf{P} = \left(\begin{smallmatrix} P_{11} & P_{12} \\ P_{21} & P_{22} \end{smallmatrix}\right)$) homogenised according to the proposed multi-scale methodology as a function of the macro-scale stretch λ, i.e. $\lambda = t + 1$, for the different sets of parameters. To better understand the role of the displacement fluctuations in the constitutive response, the right column in the same figure displays the non-affinity index I_{NA} (see (110)) which measures the magnitude of the fluctuation field. In both cases (A-heterogeneity or θ-heterogeneity) it is observed that the smaller the dispersion, the stiffer the constitutive response. Specifically, for the proposed scenarios, the mechanical response is more sensitive to the definition of fibre area than to the fibre orientation.

Note that, when the fibre area is heterogeneous (see levels l_2 and l_3), the index I_{NA} doubles that obtained when the fibre orientation is heterogeneous. Therefore, we conclude that the determination of fibre areas is a sensitive aspect in the conformation of a fibrous network, even more than the definition of fibre orientation angles.

From this study, it is also possible to analyse the reorientation of fibre families and the resulting angle dispersion in the RVE as the deformation takes place. This is reported in Fig. 8 (top row), where it is seen that the fibre dispersion diminishes as the macro-scale stretch increases, providing a sense of fibre orientation around an average value. As expected, such average fibre angle reduces with the increasing stretch. Also, the examples of the network realisations for $\delta^{l_1,1}_{\max}$, $\delta^{l_2,1}_{\max}$, $\delta^{l_3,1}_{\max}$ are illustrated in Fig. 8 (bottom and mid rows).

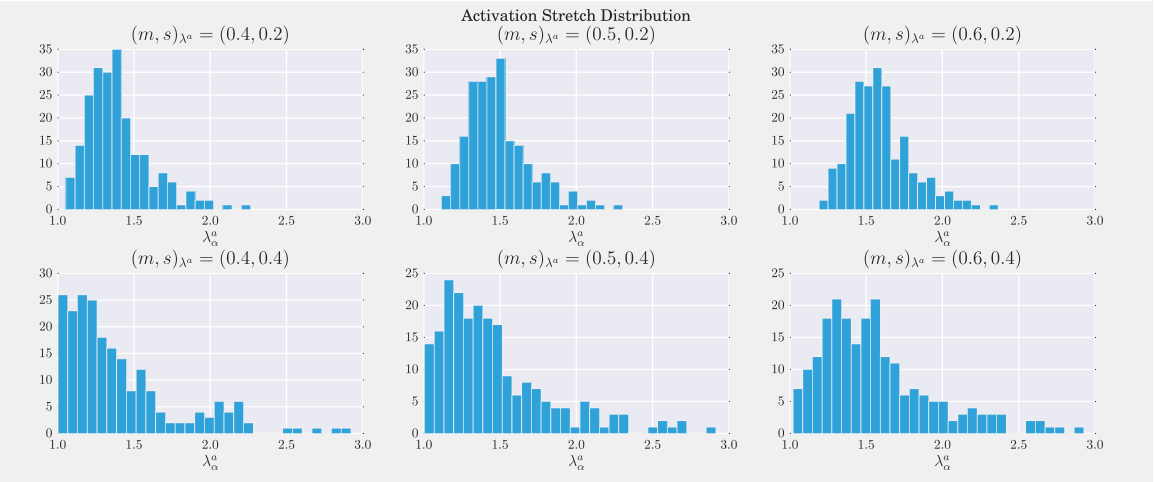

Fig. 10. Histogram of the activation stretch following a Gamma-distribution for the different realisations defined in terms of the pair $(m, s)_{\lambda^a}$.

Table 2
Network parameters to study the effect of fibre activation stretch.

All Realisations		θ 33.69°	n_{fib} 216	$\delta_{\max}[L]$ 0.03	$m_A[L^2]$ 0.01	$s_A[L^2]$ 0.001
Realisation	1	2	3	4	5	6
m_{λ^a}	0.4	0.4	0.5	0.5	0.6	0.6
s_{λ^a}	0.2	0.4	0.2	0.4	0.2	0.4

9.1.3. Effect of the activation stretch

In this section, we study the impact of potential heterogeneities in the definition of the fibre activation stretch parameter throughout the network. To this end, we consider 6 random network realisations parameterised as described in Table 2. Each realisation corresponds to a pair $(m_{\lambda^a}, s_{\lambda^a})$, equivalently denoted by $(m, s)_{\lambda^a}$, which aims to control the activation stretch of fibres in the network. Since the definition of the activation stretches does not affect the network configuration (position of nodes, connectivity, etc.), the topology is fixed for all realisations (same seed is used in the pseudo-random algorithm). Fig. 10 presents the distribution of the activation stretch as a function of the pair $(m, s)_{\lambda^a}$.

The macro-scale gradient applied to the specimens is that given by (111), and the constitutive equation of individuals fibres follows (107). In this specific case, at early stretching stages the RVE may be highly unstable because of the lack of fibre activation. To circumvent this phase, a neo-hookean material 10^{-3} times softer than the fibre material is considered to be a ground substance. Clearly, this is a pure numerical strategy necessary to stabilise the problem in cases where just few (or even none) fibres are bearing load, but which introduces no artificial ingredients in the constitutive response once the fibres activate start to be activates, as will be seen next.

Fig. 11 displays the homogenised P_{11} Piola–Kirchhoff stress tensor component for the 6 realisations. In general, the stress curves are right-shifted towards the value determined by m_{λ^a}, while the lower the standard deviation s_{λ^a} the more pronounced the uprise in the stress value. More specifically, three regions can be distinguished in each curve: toe-region, transition and linear regime. For instance, for the realisation $(m, s)_{\lambda^a} = (0.4, 0.2)$, these regions correspond approximately to the stretch intervals [1.0, 1.3], [1.3, 1.6] and [1.6, 2.0], respectively. In order to quantify the fibres that are effectively bearing load, Fig. 12(a) features the relative number of fibres whose stretch exceeds the activation stretch for all the realisations.[13] Clearly, the three regions referred to before are unveiled. The toe region has none-to-few activated fibres, while most of the fibres are engaged in the transition region, leading to the recruitment of almost all fibres in the linear regime. Such mechanism is described in the specialised literature, see for example [56]. From a phenomenological point of view, this is modelled at the macro-scale either using exponential strain energy function or a linear strain energy function convoluted with a probability density function.

[13] A schematic representation of activated fibres in deformed networks is presented in the next numerical experiment, specifically in Figs. 15 and 16.

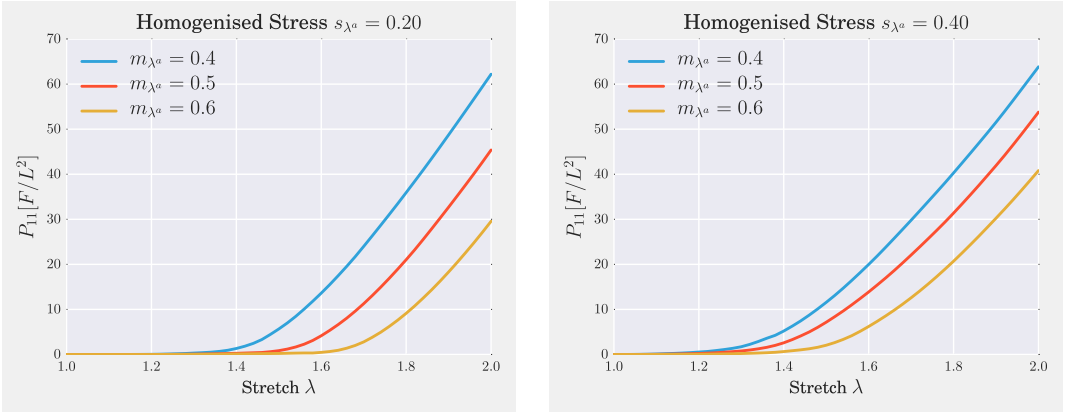

Fig. 11. Homogenised constitutive response for different distributions of the activation stretch parameter.

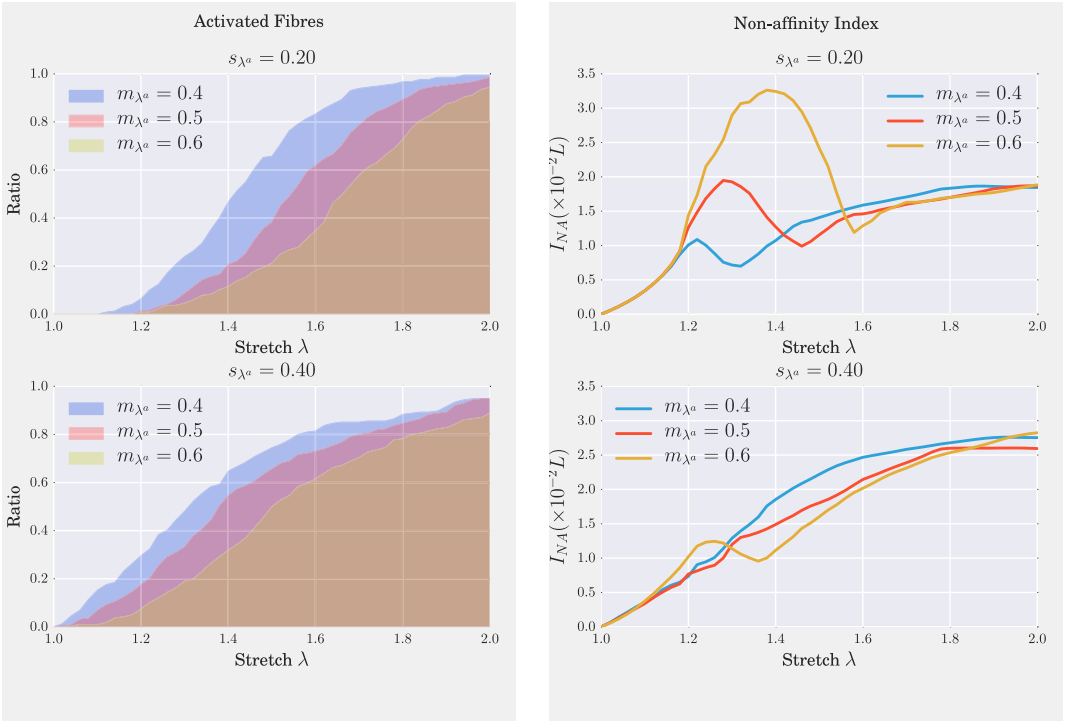

(a) Ratio of activated fibres. (b) Non-affinity index

Fig. 12. λ^a-heterogeneity in the RVE for the different realisations: impact on the non-affinity and overall activation ratio.

The heterogeneity in the fibre activation stretch leads to a complex pattern of fibre engagement, which in turn affects the magnitude of the fluctuating component of the displacement field in the network. This is manifested through the non-affinity index I_{NA}, as appreciated in Fig. 12(b). While I_{NA} is almost monotonously increasing with respect to the stretch for wide activation stretch distributions (e.g. for $s_{\lambda^a} = 0.4$), it features a non-monotonic behaviour when the distribution is sharp ($s_{\lambda^a} = 0.2$), and the magnitude of the fluctuation field becomes significantly bigger in the transition region. However, for both cases, at late loading stages, the fluctuations accommodate to a certain value, which suggests that the mechanical response has reached a stable regime.

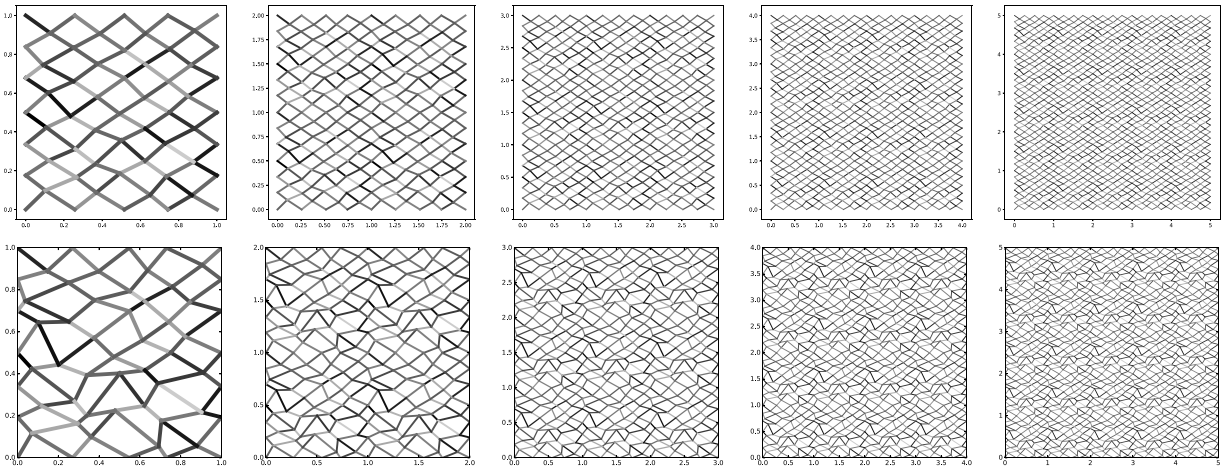

Fig. 13. Network of fibres generation through the replication of a basic unit pattern (multiplication factor from 1 to 5, i.e. left to right panels). Perturbation level l_1 in top row, and perturbation level l_2 in the bottom row. Grey colour stands for the fibre transversal area values (the more obscure the larger the area).

Table 3
Network parameters for the study of boundary conditions related to $\widetilde{\mathscr{U}}_{\mu}^{\mathsf{L}}$ and $\widetilde{\mathscr{U}}_{\mu}^{\mathsf{M}}$.

$\widetilde{\mathscr{U}}_{\mu}^{\mathsf{M}}$ and $\widetilde{\mathscr{U}}_{\mu}^{\mathsf{L}}$	θ	n_{fib}	$m_A[L^2]$	m_{λ^a}	s_{λ^a}
	33.69°	96	0.02	1.366	0.2
Levels	l_1		l_2		
$s_A[L^2]$	0.025		0.075		
$\delta_{\max}[L]$	0.025		0.075		

9.1.4. On the choice of boundary conditions

In this last section, we aim to investigate the sensitivity of the constitutive response with respect to the fibres network size, considering different sub-models from Section 4.6.3. This raises a sense of convergence as the network size is increased and the homogenised solution becomes independent from the choice of boundary conditions. Specifically, two choices are analysed, the Affine Boundary Model, $\widetilde{\mathscr{U}}_{\mu}^{\mathsf{L}}$ (see (66)), and the Minimally Constrained Model, $\widetilde{\mathscr{U}}_{\mu}^{\mathsf{M}}$ (see (64)). In the present case, the fibrous specimens to be analysed feature heterogeneities of different kinds (fibre area, orientation and activation stretch).

Firstly, two levels of perturbations were considered for the heterogeneities as detailed in Table 3. These parameters were used to generate corresponding fibres networks which have been replicated horizontally and vertically by a multiplication factor of 2, 3, 4 and 5. The value for m_{λ^a} is such that all fibres are activated when 50% of axial stretch is reached. The resulting networks are shown in Fig. 13.

As in the previous section, the loading protocol is defined by the macro-scale gradient. Also as before, the single fibre constitutive response is as in (107). Two strain paths were considered with pseudo-time $t \in [0, 1]$ sampled in 50 equally spaced increments for both cases:

1. Axial stretch (pure axial test): Identically to experiments from previous sections, and repeated here for convenience:
$$\mathbf{G}_t = \begin{bmatrix} t & 0 \\ 0 & 0 \end{bmatrix}. \tag{112}$$
2. Early axial stretch and late shear-like distortion (combined axial–shear test): In this case the macro-scale gradient is
$$\mathbf{G}_t = \begin{bmatrix} \min(t, t_0) & \max(0, t - t_0) \\ 0 & 0 \end{bmatrix}, \tag{113}$$

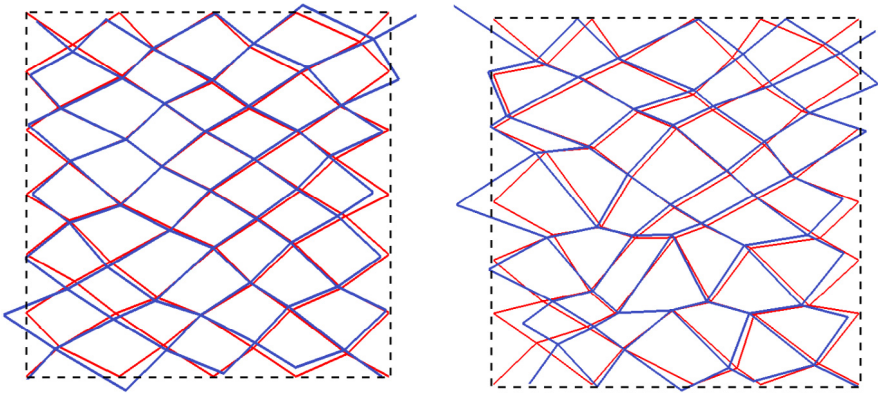

(a) Perturbation l_1 . (b) Perturbation l_2 .

Fig. 14. Impact of boundary conditions in the displacement fluctuation field. Networks warped with the displacement fluctuation for models $\widetilde{\mathscr{U}}_\mu^{\mathsf{L}}$ (red) and $\widetilde{\mathscr{U}}_\mu^{\mathsf{M}}$ (blue) at the last pseudotime in the pure axial test. (For interpretation of the references to colour in this figure legend, the reader is referred to the web version of this article.)

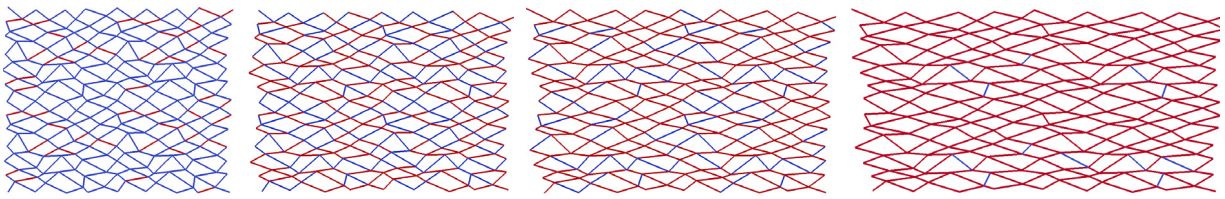

(a) $t = 0.2$ (b) $t = 0.4$ (c) $t = 0.6$ (d) $t = 1.0$

Fig. 15. Total deformed configuration of the RVE along the pseudotime showing activated fibres (in red) for the $\widetilde{\mathscr{U}}_\mu^{\mathsf{M}}$ model, at the perturbation level l_2, and for the pure axial test. (For interpretation of the references to colour in this figure legend, the reader is referred to the web version of this article.)

where $t_0 = 0.5$ for the reported numerical examples. Observe that $(\mathbf{G}_t)_{11}$ increases linearly for $t < t_0$, when this component saturates, whilst the shear component $(\mathbf{G}_t)_{12}$ only assumes non-zeros values for $t > t_0$. Around the maximum level of axial stretch ($t = t_0$), we have a minimum number of fibres activated necessary to make the network stable during shear loading stage.

Fig. 14 displays the unit networks warped with the displacement fluctuation field, where we can clearly appreciate how the selection of specific boundary conditions affects the mechanical equilibrium in the RVE. As expected, the fluctuation displacement field is larger in the $\widetilde{\mathscr{U}}_\mu^{\mathsf{M}}$ model, because it is not constrained to be null over the boundary as in the $\widetilde{\mathscr{U}}_\mu^{\mathsf{L}}$ model. This reflects the expected less stiff response of the $\widetilde{\mathscr{U}}_\mu^{\mathsf{M}}$ model.

Concerning the activation of fibres, Figs. 15 and 16 illustrate, for the pure axial and the combined axial–shear tests respectively, the progression of activated fibres along the pseudotime. For the sake of simplicity, only perturbation level l_2 is reported in Fig. 15 and just level l_1 is presented in Fig. 16, both for the $\widetilde{\mathscr{U}}_\mu^{\mathsf{M}}$ model. In the pure axial test the ratio of activation fibres increases monotonically and there is no clear tendency concerning the spatial distribution of activation fibres. On the other hand, in the combined axial–shear test and when distortion becomes increasingly important, some fibres even deactivate along one preferred family, maintaining an activation trend in the other family.

In Fig. 17, the dependence of the homogenised Piola–Kirchhoff stress tensor, $\mathbf{P} = \left(\begin{smallmatrix} P_{11} & P_{12} \\ P_{21} & P_{22} \end{smallmatrix}\right)$, on the RVE size is shown for the two perturbation levels l_1 and l_2, and for the two tests. Such plot was constructed considering $t = 1$ in the definition of the macro-scale gradient. This figure provides a sense of convergence of the RVE constitutive response as the RVE size is enlarged, which makes the solution less sensitive to the choice of boundary conditions. We observe that in most of the situations the relative differences between the $\widetilde{\mathscr{U}}_\mu^{\mathsf{L}}$ and the $\widetilde{\mathscr{U}}_\mu^{\mathsf{M}}$ are rather small, hence yielding sharp bounds, at least under the hypotheses considered, for the constitutive response of these fibrous specimens.

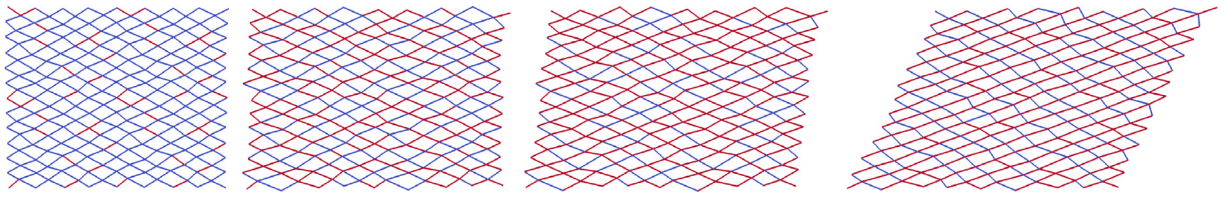

(a) $t = 0.2$ (b) $t = 0.4$ (c) $t = 0.6$ (d) $t = 1.0$

Fig. 16. Total deformed configuration of the RVE along the pseudotime showing activated fibres (in red) for the $\widetilde{\mathscr{U}}_{\mu}^{\mathsf{M}}$ model, at the perturbation level l_1, and for the combined axial–shear test. (For interpretation of the references to colour in this figure legend, the reader is referred to the web version of this article.)

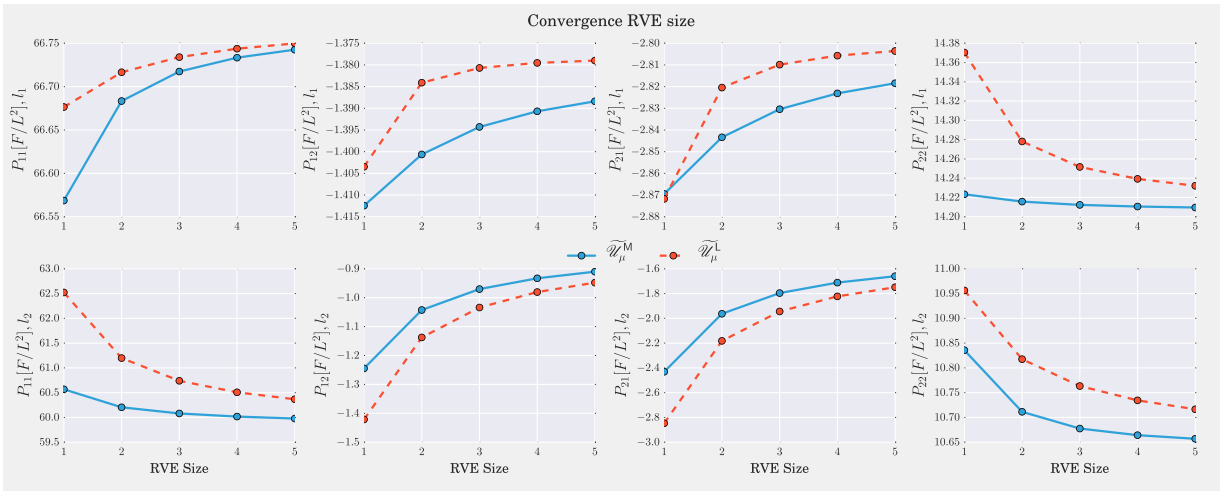

(a) Pure axial test for heterogeneity levels l_1 and l_2.

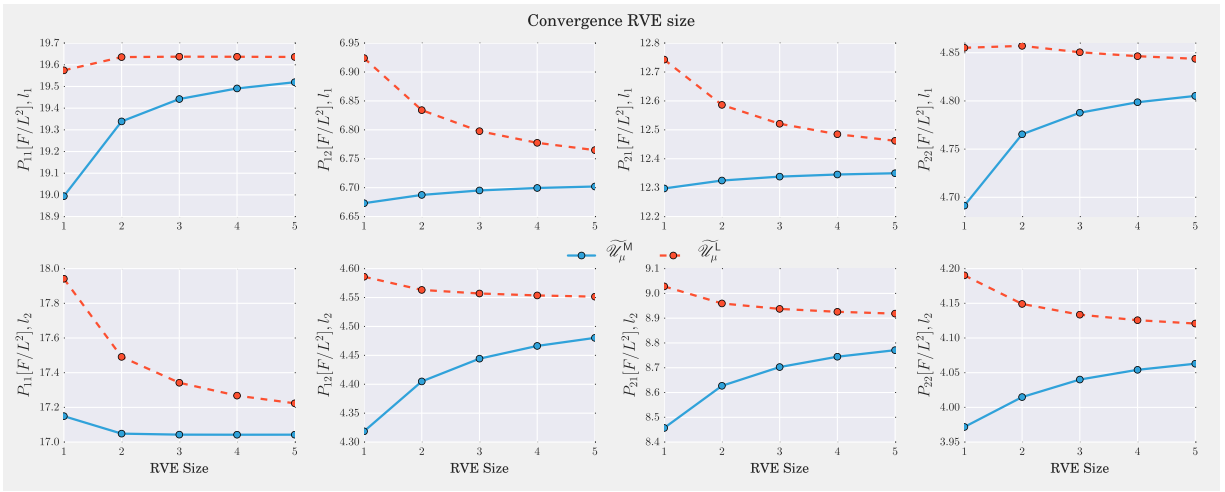

(b) Combined axial-shear test for heterogeneity levels l_1 and l_2.

Fig. 17. Convergence of the homogenised stress response with respect to the RVE size for the $\widetilde{\mathscr{U}}_{\mu}^{\mathsf{L}}$ (red dashed line) and $\widetilde{\mathscr{U}}_{\mu}^{\mathsf{M}}$ (blue solid line) models.

Going into the details, for a more homogeneous RVE and pure axial test (see top row in Fig. 17(a)), the $\widetilde{\mathscr{U}}_\mu^{\mathsf{L}}$ model is less sensitive to the RVE size (see components P_{11}, P_{12} and P_{21}). In contrast, when the heterogeneities in the RVE are more pronounced (see bottom panels of Fig. 17(b)) the $\widetilde{\mathscr{U}}_\mu^{\mathsf{M}}$ model performs better, with the dominant stress components (see P_{11} and P_{22}) being less sensitive to the RVE size.

Similar features are seen for the combined axial–shear test in Fig. 17(b). For the less perturbed state, the non-diagonal components, which are not negligible in this case, found with the $\widetilde{\mathscr{U}}_\mu^{\mathsf{M}}$ model are less sensitive to the RVE size. The opposite happens for the diagonal components. In the second perturbation level, P_{11} computed with the $\widetilde{\mathscr{U}}_\mu^{\mathsf{M}}$ model is much less sensitive to the RVE size, while for the other components the sensitivity of both models is comparable.

Note that a number of convergence patterns are found in Fig. 17 (see the behaviour of red and blue lines). For instance, at the bottom right plot of Fig. 17(b) we have the red curve decreasing, while the blue curve is increasing. In turn, in the top left plot of Fig. 17(a), both curves are increasing, with the linear model being stiffer than the minimally constrained model. The explanation for the different patterns are twofold: (i) some stress components have negligible order of magnitudes with respect to others, thus in general we should regard them according to their importance; and (ii) the large levels of variability in the parameters, specially the activation stretch. It is important to keep in mind that for the dominant stress components, the linear model is always stiffer than the minimally constrained one for the same RVE size. Importantly, by increasing the RVE size, both models feature a convergent trend.

Using a different criterion to measure convergence with respect to the RVE size, Fig. 18(a) and (c) show the convergence study with respect to the total averaged strain energy in the RVE, i.e,

$$\Psi := \frac{1}{|\Omega_\mu|} \sum_{\alpha \in \mathcal{F}_{net}} V_\alpha \, \Psi_\alpha^\mu(\lambda_\alpha), \tag{114}$$

evaluated at the equilibrium point when reaching the last loading step. In this case we have a very similar convergence pattern for all cases. Again, the linear model yields a stiffer behaviour than the minimally constrained model. Evidently, in cases where the mechanical problem can be understood as a minimisation problem (in the case of hyperelasticity), the total energy is necessarily smaller for the larger admissible space (i.e. the minimally constrained model).

Another interesting analysis consists in measuring the role played by the fluctuations in terms of energy. To this end, we propose the fluctuation energy ratio, defined as

$$\tilde{\Psi}_{rel} := \frac{|\Psi - \overline{\Psi}|}{\Psi}, \tag{115}$$

where $\overline{\Psi} := \Psi|_{\tilde{\mathbb{U}}_\mu = \mathbb{O}}$ is the averaged energy due to the linear part of displacements, i.e, vanishing displacement fluctuation. We remark that $\Psi < \overline{\Psi}$ always holds since $\tilde{\mathbb{U}}_\mu = \mathbb{O}$ represents the Taylor model, which renders a higher level of energy. For the simulations reported in this section, the behaviour of this index is observed in Fig. 18(b) and (d). As expected, the fluctuation energy ratio is always larger for the minimally constrained model. In addition, such contribution of energy becomes more important as the heterogeneities are higher as well as we move towards to a shear dominated regime.

Such results point out the importance of an adequate minimally constrained multi-scale model, as proposed in this work, in order to provide consistent and sharp bounds for the constitutive response. Even if the differences observed are in some cases negligible (notice in some cases the stress scale in the plots is really small), the correct formulation of the $\widetilde{\mathscr{U}}_\mu^{\mathsf{M}}$ allowed us to quantify the impact of the choice of boundary conditions in the homogenised response in a wide variety of scenarios. Being more specific, the minimally constrained model is a lower bound for the homogenised stress, and the affine boundary model is an upper,[14] bound of these curves. From Fig. 17 it is clear that this observation is always true, save for few cases where for relatively small values of the off-diagonal components these bounds are actually inverted.

To gain more insight into the complex behaviour the homogenised stress may render, Fig. 19 provides the stress components along the evolution of the pseudotime and for all the twenty cases ($\widetilde{\mathscr{U}}_\mu^{\mathsf{L}}$ and $\widetilde{\mathscr{U}}_\mu^{\mathsf{M}}$ with 5 RVE sizes each for pure axial and combined axial–shear tests). The convergence of the solution in the dominant stress components P_{11}

[14] Naturally, the Taylor submodel provides a stiffer response than the affine boundary model. Thus, we restrict the term "upper bound" to boundary-like constraints, excluding the Taylor model from the analysis.

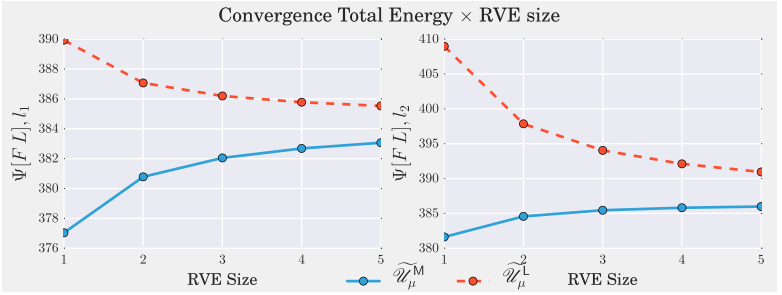

(a) Total strain energy for pure axial test.

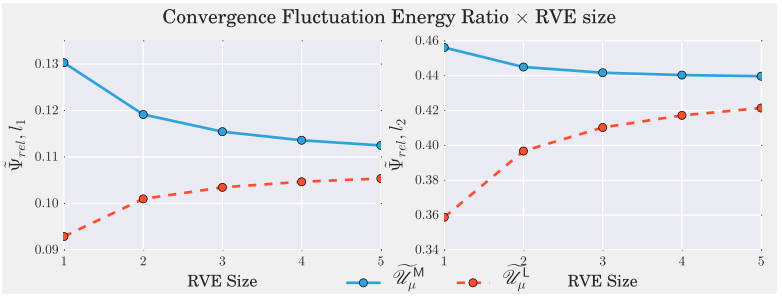

(b) Fluctuation energy ratio for pure axial test.

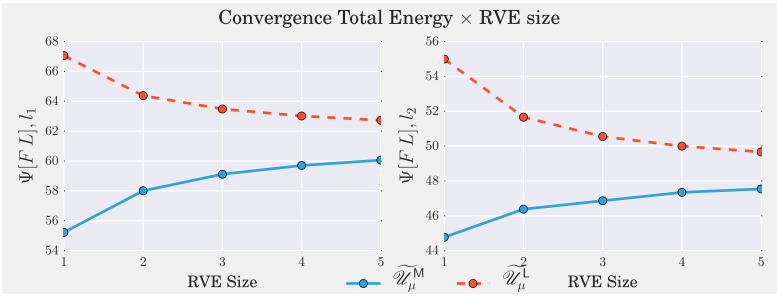

(c) Total strain energy for combined axial-shear test.

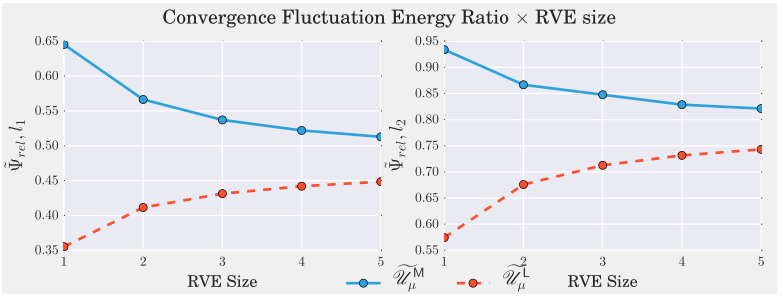

(d) Fluctuation energy ratio for combined axial-shear test.

Fig. 18. Convergence analyses with respect to the RVE size for the $\widetilde{\mathscr{U}}_\mu^{\mathsf{L}}$ (red dashed line) and $\widetilde{\mathscr{U}}_\mu^{\mathsf{M}}$ (blue solid line) models. Heterogeneity levels l_1 (left) and l_2 (right).

and P_{22} always takes place as expected (see the insets in the corresponding panels), with the $\widetilde{\mathscr{U}}_\mu^{\mathsf{L}}$ model being an upper bound and the $\widetilde{\mathscr{U}}_\mu^{\mathsf{M}}$ model behaving as a lower bound. Remarkably, for the pure axial test and for components P_{12} and

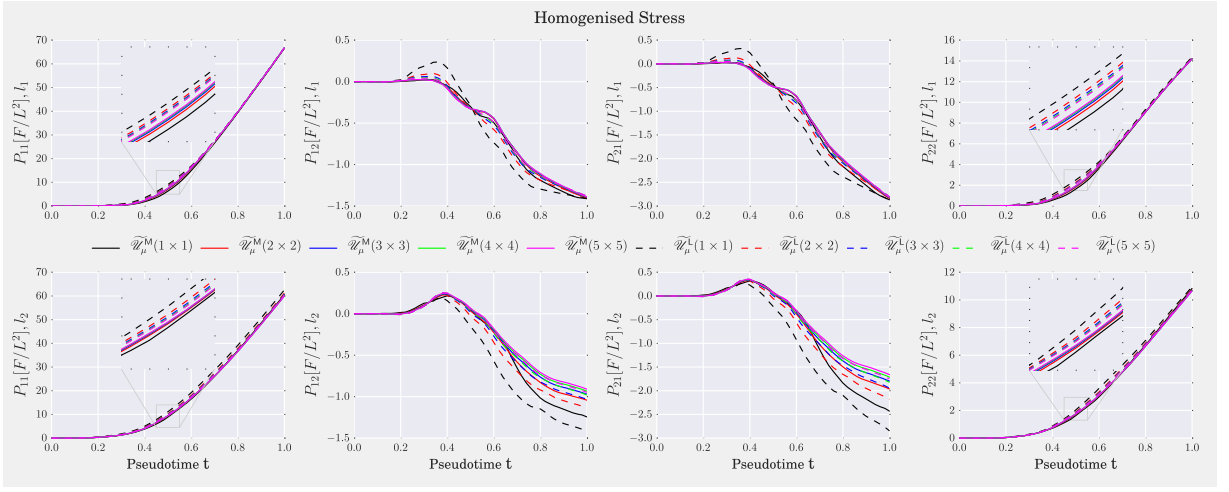

(a) Pure axial test for heterogeneity levels l_1 and l_2.

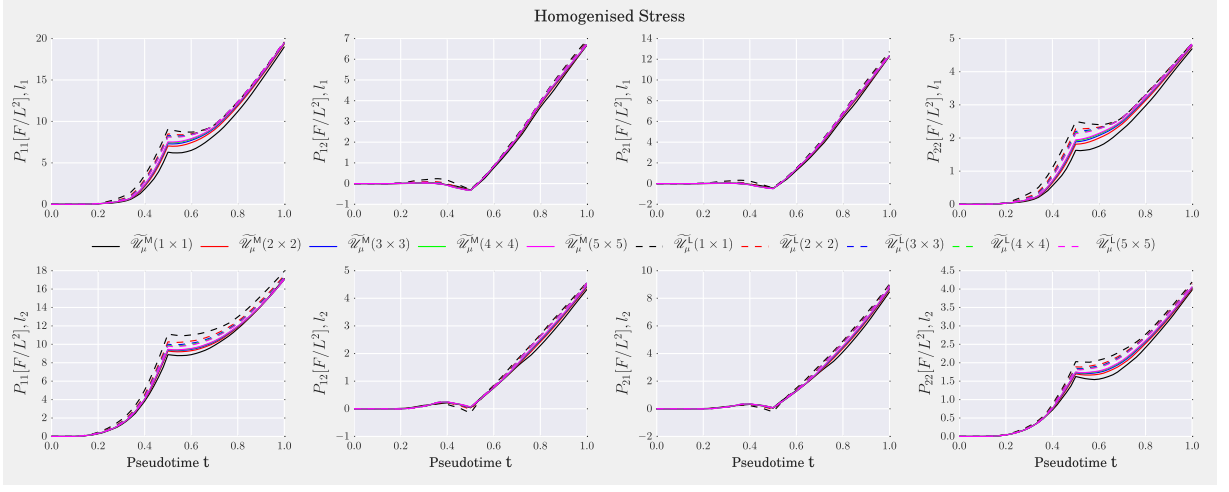

(b) Combined axial-shear test for heterogeneity levels l_1 and l_2.

Fig. 19. Homogenised stress for different boundary conditions. Stress components during pseudotime for the $\widetilde{\mathscr{U}}_\mu^{\mathsf{L}}$ (dashed lines) and $\widetilde{\mathscr{U}}_\mu^{\mathsf{M}}$ (solid lines) models.

P_{21}, the response delivered by the $\widetilde{\mathscr{U}}_\mu^{\mathsf{L}}$ model is much more sensitive to the RVE size than the corresponding to the $\widetilde{\mathscr{U}}_\mu^{\mathsf{M}}$ model. This effect is reduced when off-diagonal stress components gain importance as in Fig. 19(b). Observe that exactly at the point of axial phase becoming shear distortion the stress curves are less similar, but the trend remains similar to the cases discussed before.

9.2. Simulations in a three-dimensional setting

9.2.1. Generation of the network

Network generation of the three-dimensional random fibre network was based on Voronoi tessellations. For this task, the open source library *Voro++* [57] and its wrapper for Python *pyvoro*[15] have been employed. First, a certain number of points are chosen at random positions, and maintaining a certain distance among them. These points are

[15] URL: https://pypi.org/project/pyvoro/1.3.1/.

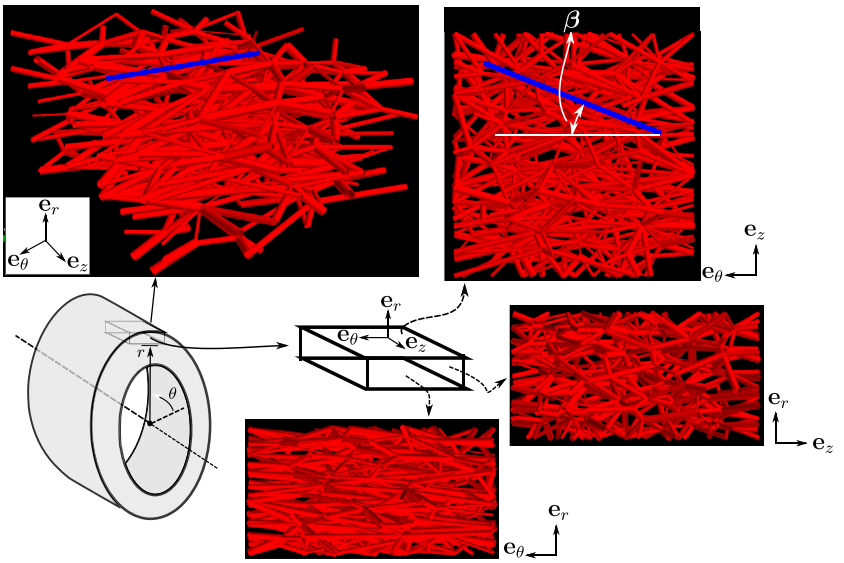

Fig. 20. Three-dimensional RVE from a piece of an adventitia layer and projections on the coordinate planes.

used as barycentric of cells that form a partition of a rectangular parallelepiped whose dimensions are also inputs to the algorithm. Then, a fibre is considered over cell edges (transversal area and activation stretch are randomly assigned following a given distribution). Edges lying on the RVE boundary are removed. A preference direction is emulated by considering a preliminary network which is scaled differently in the different directions. An example of network resulting from this pipeline is shown in Fig. 20. The RVE is considered to be a representative piece of adventia layer (mainly composed by collagen) in a model of an arterial vessel. The initial network was generated in $0.5 \times 1.0 \times 1.0L^3$ (sizes in the directions $\mathbf{e}_\theta$, $\mathbf{e}_z$ and $\mathbf{e}_r$, respectively) and then mapped to a size of $1.0 \times 1.0 \times 0.5L^3$. The effect of this scaling procedure is translated in the, say, circumferential angle denoted by β (assumed positive but equally valid for negative value), as observed in Fig. 20. In this case $\beta < 45°$ as the initial block was scaled in $\mathbf{e}_\theta$ direction, whereas $\beta = 45°$ when no scaling is involved.

9.2.2. Effect of circumferential angle

In this example we study the sensitivity in the mechanical response with respect to differences in the circumferential angle β. To this end, we generated 6 networks, 3 for each of the 2 cases as the following procedure:

1. Map from $1/2 \times 1.0 \times 1.0$ to $1.0 \times 1.0 \times 0.5$: $\beta_1 = \arctan(1/2) = 26.57°$.
2. Map from $1/3 \times 1.0 \times 1.0$ to $1.0 \times 1.0 \times 0.5$: $\beta_2 = \arctan(1/3) = 18.43°$.

In all cases 200 random points (centres of the Voronoi cells) were uniformly picked inside the brick domain. This resulted in networks with approximately 750 fibres.[16] In addition, fibre areas were taken randomly from a normal distribution with mean $0.01L^2$ and standard deviation of $0.0005L^2$. Fibre constitutive model was assumed to be the same than for the examples from Section 9.1, with unitary uniform activation stretch for all fibres, and axial load applied along the circumferential direction. The macro-scale applied strain program is characterised by the gradient $\mathbf{G}_t = t\mathbf{e}_\theta \otimes \mathbf{e}_\theta$, with $t \in [0.0, 0.7]$ divided into 20 equally spaced pseudo-time steps. The realisations are denoted $(\beta_a)_b$, $a \in \{1, 2\}$, $b \in \{i, ii, iii\}$ and some examples of undeformed meshes can be seen in Fig. 22(a) and (b), the later displaying a smaller circumferential angle. To verify the preferred direction numerically we compute the structural tensors (see definition (55)) for the different cases

$$\mathbf{B}_{(\beta_1)_i} = \begin{bmatrix} \mathbf{0.69740} & -0.00513 & 0.00450 \\ -0.00513 & \mathbf{0.23118} & 0.00033 \\ 0.00450 & 0.00033 & \mathbf{0.07142} \end{bmatrix},$$

[16] A certain number of Voronoi cells does not yield the same certain number of fibres.

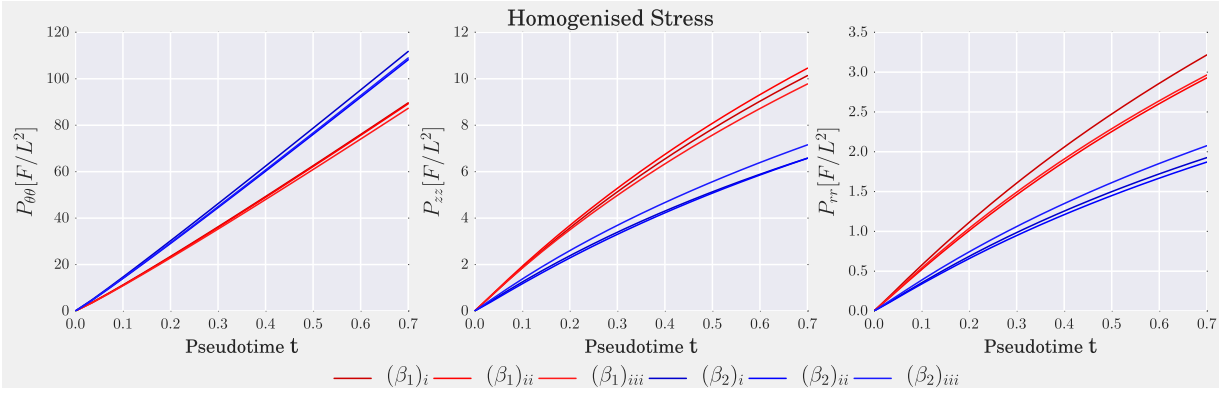

Fig. 21. Homogenised stress tensor components along the loading program for the different circumferential angles.

$$\mathbf{B}_{(\beta_2)_i} = \begin{bmatrix} \mathbf{0.82643} & -0.01320 & -0.00275 \\ -0.01320 & \mathbf{0.13334} & 0.00398 \\ -0.00275 & 0.00398 & \mathbf{0.04024} \end{bmatrix},$$

where the basis considered is $\{\mathbf{e}_\theta, \mathbf{e}_z, \mathbf{e}_r\}$ (in this order). Regarding the first value of the diagonal (related with the circumferential direction), we confirm the graphical suggestion, in general fibres are more aligned with $\mathbf{e}_\theta$ in the case $(\beta_2)_i$ than in case $(\beta_1)_i$.

Fig. 21 reports the components of the homogenised stress tensor for all three normal realisations and for both circumferential angles. As expected, the realisations with a smaller circumferential angle (group β_2) feature a stiffer response in the circumferential stress component, while for the axial and radial components, RVEs in group β_1 are stiffer.

10. Discussion

10.1. On model predictions

Based on the reported numerical experiments using the proposed novel multi-scale model for fibrous materials, we can highlight the following features:

1. The mechanical response is sensitive to non-homogeneities in network parameters, such as fibre orientation, fibre area or activation stretches. In fact, different RVE realisations lead to different stress curves (see Fig. 9 left column).
2. Moreover, the more structured and homogeneous the RVE, the stiffer the constitutive response (see also Fig. 9 left column). This goes along with a larger non-affinity in the network kinematics, as measures by the index I_{NA} (see Fig. 9 right column).
3. Concerning the dispersion of fibre orientations it is observed that its variability and mechanical effect becomes less evident when RVE is stretched (see Fig. 8). Such fibre alignment reduces the rate of the non-affinity at late stretching stages (see Fig. 9 bottom right column panel).
4. Concerning the dependence upon the activation stretch distribution, it is observed that the homogenised mechanical response of an RVE, resulting from the intermingling of progressively activated fibres (as noticed in Fig. 12(a)), assumes a very distinct shape than the constitutive model adopted for a single fibre. In our particular case, an exponential-shaped stress curve (see Fig. 11) is retrieved by using simple linear (quadratic strain energy) constitutive laws for the micro-scale constituents, i.e, the fibres.
5. Finally, the comparison between two boundary conditions have resulted in two different scenarios. On the one hand, the more homogeneous, and then stiffer, the network, the more suitable results the Affine Boundary Model in terms of the solution delivered by small RVE sizes. On the other hand, for highly heterogeneous networks, the use of the Minimally Constrained Model proposed in the present work yields better results in terms of the

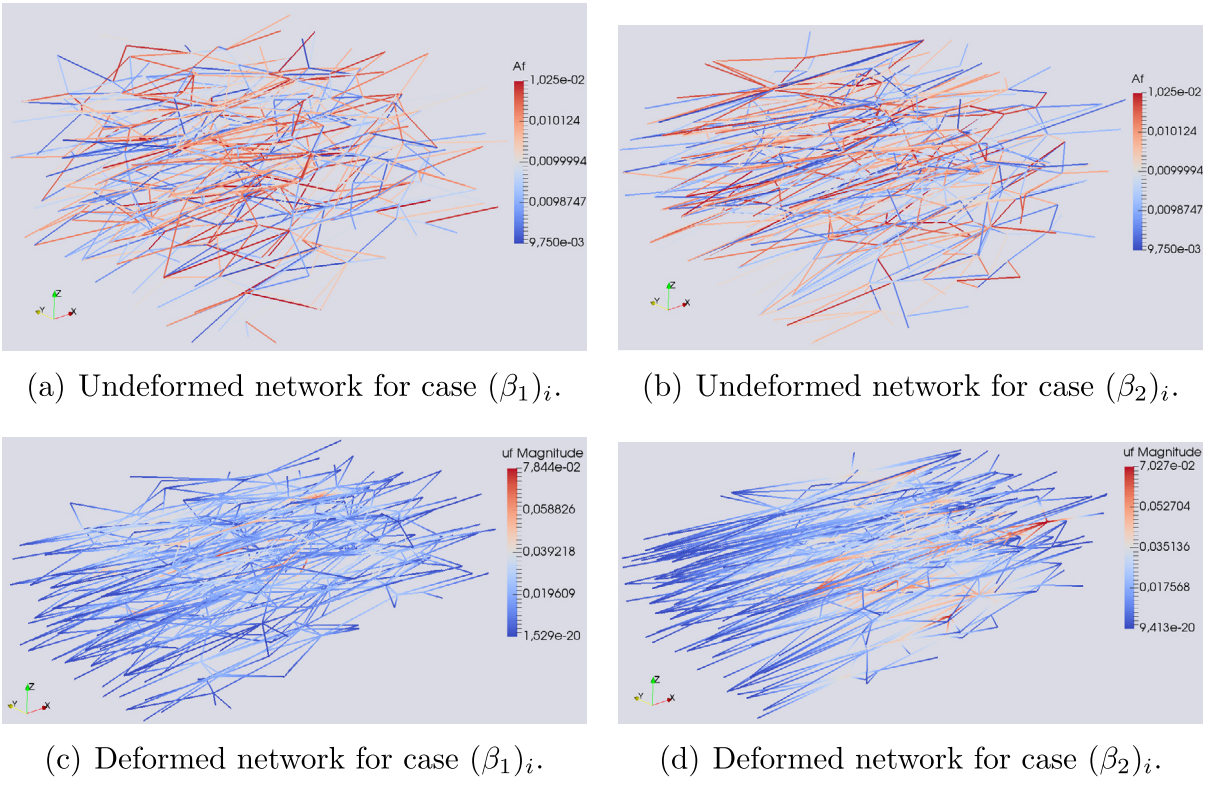

(a) Undeformed network for case $(\beta_1)_i$.

(b) Undeformed network for case $(\beta_2)_i$.

(c) Deformed network for case $(\beta_1)_i$.

(d) Deformed network for case $(\beta_2)_i$.

Fig. 22. Reference and deformed configurations of 3D networks. Colours represent fibre area at the beginning of the loading program (first row) and the fluctuation magnitude for the last loading step (second row). (For interpretation of the references to colour in this figure legend, the reader is referred to the web version of this article.)

solution delivered by small RVE sizes. In any case, the two tested boundary conditions, which lead to two multi-scale models, determine proper bounds (without considering Taylor submodel) for the constitutive response of fibrous micro-structures. In this sense, we highlight that the proposed model constitutes an unprecedented lower bound for this kind of analyses.

Based on the results reported in this work, the relevance of a proper multi-scale model for fibrous tissues is larger as the network heterogeneities are more pronounced, and this holds for any of the sources of heterogeneities studied in this work. Some recent phenomenological models even include specific parameters to account for the effect of dispersion in the fibre orientation [4]. However, as seen in this work, this is not enough to effectively predict the constitutive behaviour of fibrous networks with more accentuated heterogeneities. Moreover, up to the authors' knowledge, dispersion in fibre properties such as area and activation stretch have been overlooked in most of phenomenological, or even histologically-inspired constitutive models. It is worth mentioning that these data can also be extracted from images by using proper image processing techniques already available in the literature.

10.2. Limitations

In the construction of the micro-scale kinematics, we have neglected phenomena related to some deformation modes the fibres may be subjected to. Bending and torsion are two examples as well as the interaction among fibres at junctions. Particularly, interfibre sliding, and torsional resistance of junctions as a consequence of fibre interactions are two examples which could provide an even more heterogeneous micro-mechanical phenomenology. Particularly, inter-fibre sliding mechanisms have been modelled in El Nady and Ganghoffer [19] by using auxiliary beams in the contact. Bending phenomena and torsional resistance of junctions have been partially addressed in Stylianopoulos and Barocas [12]. Nevertheless, in such work it has been shown that for physiological ranges of stretches, fibre stretching

continued to play the most important role in the constitutive response. Based on this, the proposed model is suitable for biomedical application, and, moreover, it constitutes a general and consistent multi-scale formalism which enables more kinematical complexities to be incorporated in order to test further hypotheses. In contrast, Berkache et al. [17] introduce a parameter representing the ratio between bending and axial stiffnesses to establish a transition where the response is dominated by bending or by axial tension.

Considering the theoretical suitability of the multi-scale approach, we highlight that the present work focused on the coupling between a fibrous network and a standard continuum. When the hypothesis of scale separation is questionable, and size-effects are important, the model must be improved in order to capture a more complex phenomenology [58,59]. However, even in the context of higher order continua, or fracture mechanics, the MMPV has proven to be a suitable tool for the development of effective multi-scale models [40,43], by providing the characterisation of the minimally constrained kinematically admissible space in which the generalised Hill–Mandel principle has to be regarded. These issues have been addressed in fibrous materials by the works of El Nady and Ganghoffer [19], Berkache et al. [17].

From the numerical point of view, whenever the use coupled multi-scale simulations (also called computational homogenisation or FE^2) are to be conducted in the context of finite element procedures, the computational cost involved poses a challenge to be addressed. In fact, the application of the present multi-scale approach requires, for each Newton iteration at the macro-scale equilibrium problem, the determination of the stress and the tangent operator at each Gauss point. Thus, the development of discrete mechanical models for representing the micro-scale phenomenology is fundamental given its considerably cheaper computing burden when compared to continuum approaches to the same problem. Another essential issue, that requires a statistically more rigorous attention, is the correction determination of the minimum RVE size, in which an effective methodology was introduced by Kanit et al. [60]. Notwithstanding the micro-scale problem is considered an embarrassingly parallel assembly process, it requires an efficient management of the computational resources at hand for an effective implementation. Currently, this is only possible if high performance computing facilities are available. One possible approach, specifically in the context of load history independent material behaviour, is the off-line construction of an atlas of constitutive responses (stress and tangent operator) for a certain representative range of potential load settings. The atlas could then be stored and accessed during on-line computations. Another approach consists in the exploitation of the micro-scale model as an in-silico mechanical testing machinery to fit the material parameters of a macro-scale strain energy function. Finally, more sophisticated approaches relying on the concept of dimensionality reduction can be applied [61].

10.3. About modelling perspectives

A real motivation for the development of this kind of multi-scale model is the modelling of fibre damage processes. Clearly, loading of fibrous specimens featuring damage yields more intricate mechanical interactions, which makes even more complex the constitutive analysis because of the highly heterogeneous strain patterns nature of the fibre network. In essence, the consideration of degradation processes weakens some parts of the networks as a consequence of the fibre geometry, orientation, history of loadings, etc. This is known in the continuum mechanics realm as strain localisation phenomena and results in the softening of the overall constitutive response. It has already been experimentally shown that in biological fibrous tissues the unstable part of the constitutive response is characterised by a series of bumps in the stress–stretch response, that is a series of softening and hardening stages. Classical phenomenological damage modelling usually associates a single damage parameter for each fibre family [51,62], which seems not to be enough to precisely model such complex interplay involving deactivation–activation–reorientation–degradation of fibres. In this direction, we oversee a great applicability of the proposed theoretical multi-scale model.

In the present context, the consideration of the novel Minimally Constrained Model is an important springboard to perform multi-scale analyses and comparisons with existing models which exploit the Affine Boundary Model, as well as other mixed stress–displacement RVE boundary conditions. Moreover, an important characteristic of the aforementioned damage process is propagation of strain localisation band throughout the network of fibres, therefore a more flexible kinematics on boundary is specially mandatory in order not to preclude these deformation modes from unfolding.

At last but not least, the proposed multi-scale approach was straightforwardly implemented to 3D RVEs, which makes it an excellent candidate for also guiding the construction of general constitutive laws capable of accounting for all the heterogeneities studied in this work.

11. Concluding remarks

In this work, a multi-scale model for microscopic fibre networks has been developed in order to retrieve a continuum-like constitutive response. Although the focus has been on modelling arterial tissue, the theory is general and can be applied to any fibrous material. The main contributions of the present work is a rigorous and general derivation of the micro-mechanical equilibrium problem as well as of the homogenisation formula for the dual stress entity from a minimum set of basic kinematical hypotheses and through the use of the Principle of Multiscale Virtual Power [30,31]. Furthermore, intrinsic to the proposed multi-scale formulation is the construction of the so-called minimally constrained model, resulting in a lower bound for the homogenised mechanical response, of great theoretical and practical interest. As a sub-product of the proposed variational setting, a specific homogenisation formula for incompressible materials has also been established. In addition, we have also shown that the proposed minimally constraining boundary condition is equivalent to setting a uniform traction model, and an alternative formulation of practical interest has been reported resorting to the theory of Lagrange Multipliers.

Finally, through several numerical experiments, different key aspects of the theory have been demonstrated, with special emphasis in the study of the sensitivity of the homogenised constitutive in terms of different kinds of heterogeneities in the fibrous network architecture and with respect to the choice of kinematically admissible boundary conditions for the micro-mechanical equilibrium problem.

Acknowledgements

This work was supported by the Brazilian agencies CNPq (grant 140767/2015-0), FAPERJ (grant E-26/200.186/2017) and CAPES/PDSE — 88881.132604/2016-01. The support of these agencies is gratefully acknowledged. P.J. Sánchez acknowledges the financial support from CONICET (grant PIP 2013–2015 631) and ANPCyT (grant PICT 2015–2017 3372). We are also deeply thankful to some fruitful and inspiring discussions, held in early stages of this work, with Prof. Eduardo de Souza Neto (Swansea University) and Prof. Anne Robertson (University of Pittsburgh).

Appendix A. From continuum to discrete description of networks

In this section our aim is to succinctly review concepts of multi-scale modelling for standard continuum media using the MMVP (Method of Multi-scale Virtual Power) proposed in [30,31]. Specially, in Appendix A.1 we analyse the case of a continuous RVE with voids reaching the boundary, something that could be understood as the groundwork for our model of a fibre networks, to be derived in Appendix A.2.

It should be mentioned that the formulation presented here is not classical in multi-scale theory. Particularly, this is because displacements fields are not well defined in the absence of material points, that is, in the void (empty) domain. This particularity has already been noticed in the literature, e.g., [63,64]. However, up to the authors' knowledge, the impact of this fact to the derivation of admissible boundary condition in RVEs with random voids reaching boundary (not periodic), has not yet been established in literature.

A.1. Continuum RVE model with voids reaching the boundary

Let Ω_μ^s (Ω_μ^v) and $\partial\Omega_\mu^s$ ($\partial\Omega_\mu^v$) be the solid (void) domain and its boundary respectively, as described in Fig. A.23. Also, consider that the RVE is associated to point $\mathbf{x}$ from the macro-scale and its domain is denoted by

$$\Omega_\mu = \overline{\Omega_\mu^s \cup \Omega_\mu^v}, \tag{A.1}$$

where $\partial\Omega_\mu$ is the boundary. We also set

$$\partial\Omega_\mu^{s,b} = \partial\Omega_\mu^s \cap \partial\Omega_\mu \ , \ \partial\Omega_\mu^{v,b} = \partial\Omega_\mu^v \cap \partial\Omega_\mu \ , \ \partial\Omega_\mu^{s,v} = \partial\Omega_\mu^s \cap \partial\Omega_\mu^v. \tag{A.2}$$

Then, it is verified that $\partial\Omega_\mu = \partial\Omega_\mu^{s,b} \cup \partial\Omega_\mu^{v,b}$. By convention, a normal vector of $\partial\Omega_\mu^{s,b}$, denoted by $\mathbf{n}$, always points from the solid towards the void domain. Now, following [30] and for given $\mathbf{u}|_\mathbf{x}$ and $\mathbf{G}|_\mathbf{x}$ macro-scale displacement vector and macro-scale gradient of displacement tensor, respectively, we concisely present the main points of the theory next.

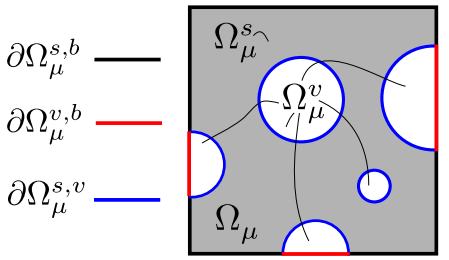

Fig. A.23. Example of RVE with voids reaching the boundary.

- **Displacement in the solid domain**
  The micro-scale displacement field $\mathbf{u}_\mu : \Omega_\mu^s \to \mathbb{R}^{\mathrm{n_d}}$ is entirely characterised by $\mathbf{u}|_{\mathbf{x}}$, $\mathbf{G}|_{\mathbf{x}}$ and by the fluctuation field $\widetilde{\mathbf{u}}_\mu : \Omega_\mu^s \to \mathbb{R}^{\mathrm{n_d}}$ as follows

$$\mathbf{u}_\mu(\mathbf{y}) = \overbrace{\mathbf{u}|_{\mathbf{x}} + \mathbf{G}|_{\mathbf{x}}(\mathbf{y}-\mathbf{y}_G)}^{\bar{\mathbf{u}}_\mu} + \widetilde{\mathbf{u}}_\mu(\mathbf{y}), \quad \mathbf{y} \in \Omega_\mu^s, \tag{A.3}$$

  where $\bar{\mathbf{u}}_\mu$ corresponds to the insertion of the displacement and gradient from the macro-scale into the micro-scale.
- **Gradient in the solid domain**
  Applying the gradient operator on (A.3) yields

$$\nabla_{\mathbf{y}}\mathbf{u}_\mu(\mathbf{y}) = \mathbf{G}|_{\mathbf{x}} + \nabla_{\mathbf{y}}\widetilde{\mathbf{u}}_\mu(\mathbf{y}), \quad \mathbf{y} \in \Omega_\mu^s. \tag{A.4}$$

- **Homogenisation of displacement field**
  Regarding the conservation of the displacement field, we postulate

$$\mathbf{u}|_{\mathbf{x}} = \frac{1}{|\Omega_\mu^s|}\int_{\Omega_\mu^s} \mathbf{u}_\mu \,\mathrm{d}V_\mu. \tag{A.5}$$

  This homogenisation formula together with the admissibility kinematical constraint $\frac{1}{|\Omega_\mu^s|}\int_{\Omega_\mu^s} \bar{\mathbf{u}}_\mu \,\mathrm{d}V_\mu = \mathbf{u}|_{\mathbf{x}}$ renders

$$\mathbf{y}_G = \frac{1}{|\Omega_\mu^s|}\int_{\Omega_\mu^s} \mathbf{y} \,\mathrm{d}V_\mu, \tag{A.6}$$

  and, therefore, it leads to

$$\int_{\Omega_\mu^s} \widetilde{\mathbf{u}}_\mu \,\mathrm{d}V_\mu = \mathbf{0}. \tag{A.7}$$

- **Homogenisation of gradient field**
  As for the conservation of the displacement gradient field, we postulate

$$\mathbf{G}|_{\mathbf{x}} = \frac{1}{|\Omega_\mu^s|}\Bigg[\int_{\Omega_\mu^s} \nabla_{\mathbf{y}}\mathbf{u}_\mu(\mathbf{y}) \,\mathrm{d}V_\mu - \int_{\partial\Omega_\mu^{v,s}} \widetilde{\mathbf{u}}_\mu \otimes \mathbf{n} \,\mathrm{d}S_\mu - \int_{\partial\Omega_\mu^{s,b}} \widetilde{\mathbf{u}}_\mu \otimes \bar{\mathbf{n}} \,\mathrm{d}S_\mu\Bigg], \tag{A.8}$$

  where $\mathbf{n}$ is the outward unit normal vector to $\partial\Omega_\mu^s$ and $\bar{\mathbf{n}}$ a vector to be defined at a later stage. Again, this homogenisation together with the kinematical constraint $\frac{1}{|\Omega_\mu^s|}\int_{\Omega_\mu^s} \nabla_{\mathbf{y}}\bar{\mathbf{u}}_\mu(\mathbf{y}) \,\mathrm{d}V_\mu = \mathbf{G}|_{\mathbf{x}}$ results in

$$\int_{\Omega_\mu^s} \nabla_{\mathbf{y}}\widetilde{\mathbf{u}}_\mu \,\mathrm{d}V_\mu - \int_{\partial\Omega_\mu^{v,s}} \widetilde{\mathbf{u}}_\mu \otimes \mathbf{n} \,\mathrm{d}S_\mu - \int_{\partial\Omega_\mu^{s,b}} \widetilde{\mathbf{u}}_\mu \otimes \bar{\mathbf{n}} \,\mathrm{d}S_\mu =$$

$$\sum_{e\in\{v,b\}}\int_{\partial\Omega_\mu^{s,e}}\widetilde{\mathbf{u}}_\mu\otimes\mathbf{n}\,\mathrm{d}S_\mu-\int_{\partial\Omega_\mu^{v,s}}\widetilde{\mathbf{u}}_\mu\otimes\mathbf{n}\,\mathrm{d}S_\mu-\int_{\partial\Omega_\mu^{s,b}}\widetilde{\mathbf{u}}_\mu\otimes\bar{\mathbf{n}}\,\mathrm{d}S_\mu=$$
$$\int_{\partial\Omega_\mu^{s,b}}\widetilde{\mathbf{u}}_\mu\otimes(\mathbf{n}-\bar{\mathbf{n}})\,\mathrm{d}S_\mu=\mathbf{O}. \tag{A.9}$$

Now we impose that constraint (A.9) is valid for trivial case where $\tilde{\mathbf{u}}_\mu(\mathbf{y})=\mathbf{c}$, $\forall\mathbf{y}\in\Omega_\mu^s$. Thus, $\bar{\mathbf{n}}$ is defined as:

$$\bar{\mathbf{n}}=\frac{1}{|\partial\Omega_\mu^{s,b}|}\int_{\partial\Omega_\mu^{s,b}}\mathbf{n}(\mathbf{y})\,\mathrm{d}\mathcal{S}_\mu. \tag{A.10}$$

Remark 27. It is worth discussing some non-classical aspects of the above homogenisation postulations. Firstly, a standard volume average has been considered for the displacement field in (A.5), with the main difference lying in the fact that only the solid part of the domain has been considered. This is natural since the kinematics is not even defined outside the solid part (see Remarks 9 and 12). Secondly, the homogenisation of the gradient has been established in (A.8) using exclusively the solid part of the RVE domain. Additionally to the integral over the volume, this definition gives rise to some terms appearing in the form of boundary integrals. For the boundary void-solid integral, only fluctuations are required in order to be consistent with the insertion restricted to the solid part as already commented. Finally, the integral over the solid boundary featuring also the average normal vector is included to remove the spurious macro-scale gradient induced by a constant fluctuation field. This is a particularity found specially in fibrous material modelling, in which one has random voids reaching the boundary. When the voids reach the boundary in a periodic manner, the average normal term vanishes.

A.2. Transition from continuum to discrete network

Now, consider in the model developed in Appendix A.1 that the voids grow sufficiently so that the solid part can be portioned in a number of slender parts (each one representing a bundle of fibres) and in their intersections (joints) as in Fig. A.24. The domain Ω_μ^α denotes the volume occupied by a fibre $\alpha\in\mathcal{F}_{net}$ and Ω_μ^i is the domain of a joint $i\in\mathcal{N}_{net}$. Also, let us define the following auxiliary notations

$$\begin{aligned}
&\Omega_\mu^F=\bigcup_{\alpha\in\mathcal{F}_{net}}\Omega_\mu^\alpha\ ,\ \Omega_\mu^N=\bigcup_{i\in\mathcal{N}_{net}}\Omega_\mu^i\ ,\ \Omega_\mu^s=\overline{\Omega_\mu^F\cup\Omega_\mu^N},\\
&\partial\Omega_\mu^{\alpha,v}=\partial\Omega_\mu^\alpha\cap\partial\Omega_\mu^v\ ,\ \partial\Omega_\mu^{i,v}=\partial\Omega_\mu^i\cap\partial\Omega_\mu^v\ ,\ \partial\Omega_\mu^{i,b}=\partial\Omega_\mu^i\cap\partial\Omega_\mu,\\
&\partial\Omega_\mu^{F,N}=\partial\Omega_\mu^F\cap\partial\Omega_\mu^N\ ,\ \partial\Omega_\mu^{\alpha,N}=\partial\Omega_\mu^\alpha\cap\partial\Omega_\mu^N\ ,\ \partial\Omega_\mu^{i,F}=\partial\Omega_\mu^i\cap\partial\Omega_\mu^F.
\end{aligned} \tag{A.11}$$

Further, note that $\partial\Omega_\mu^{s,b}=\cup_{i\in\mathcal{N}_{net}}\partial\Omega_\mu^{i,b}$, i.e, the fibres are assumed to be always connected to the boundary through a boundary joint. By convention, a normal vector $\mathbf{n}$ of a surface $\partial\Omega^{r,t}$, always points from Ω_μ^r to Ω_μ^t, where $r,t\in\{\alpha,i,F,N,s,v\}$ as above in (A.11).

It is important to remark here that in the following developments we will maintain the same kinematics as described in Appendix A.1, however now we will introduce what we call the *Hypothesis of Small Joints* (HSJ) and *Hypothesis of truss* (HT) which relies on the assumptions.

(HSJ.A1) For a given integrable function φ defined in Ω_μ^s of any type value (scalar, vector, tensor value), with reasonable same order of magnitude in Ω_μ^s, the approximation

$$\sum_{\alpha\in\mathcal{F}_{net}}\int_{\Omega_\mu^\alpha}\varphi\,\mathrm{d}\Omega_\mu^\alpha\gg\sum_{i\in\mathcal{N}_{net}}\int_{\Omega_\mu^i}\varphi\,\mathrm{d}\Omega_\mu^i, \tag{A.12}$$

holds. One first corollary is that

$$|\Omega_\mu^s|=\sum_{\alpha\in\mathcal{F}_{net}}|\Omega_\mu^\alpha|+\sum_{i\in\mathcal{N}_{net}}|\Omega_\mu^i|\approx\sum_{\alpha\in\mathcal{F}_{net}}|\Omega_\mu^\alpha|=|\mathcal{F}_{net}|, \tag{A.13}$$

which is obtained by taking $\varphi=1$.

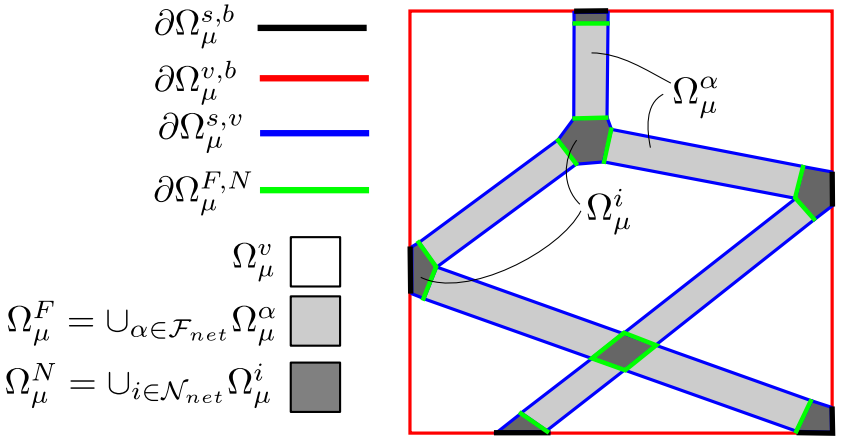

Fig. A.24. Example of a porous RVE featuring connected slender structural components.

(HSJ.A2) The joints are so small that material points $\mathbf{y} \in \Omega_\mu^i$ can be approximated by the point $\mathbf{y}_i$ characterising the joint $i \in \mathcal{N}_{net}$. Provided that $\mathbf{y} \approx \mathbf{y}_i$, by the continuity of the displacement fluctuation we have

$$\tilde{\mathbf{u}}_\mu(\mathbf{y}) \approx \tilde{\mathbf{u}}_\mu(\mathbf{y}_i) = \tilde{\mathbf{u}}_\mu^i, \quad \forall \mathbf{y} \in \Omega_\mu^i. \tag{A.14}$$

Hence, the above assumption together with HSJ.A1 and (A.3) justify the adoption of the expression (37) for the displacement at the joint $i \in \mathcal{N}_{net}$ in our discrete model for Networks.

(HT) The slender parts of the solid are so slender that allow us to be modelled as straight trusses with constant cross sections, denoted $A_\alpha, \alpha \in \mathcal{F}_{net}$. Since, the displacement at each bar $\alpha \in \mathcal{F}_{net}$ must be constant in the cross section of the bar and equal to the displacement at the centre of this section which is given by the linear interpolation between the displacement at initial, $\bar{\mathbf{y}}_{i_\alpha} \in \partial\Omega_\mu^\alpha \cap \partial\Omega_\mu^i$, and end, $\bar{\mathbf{y}}_{j_\alpha} \in \partial\Omega_\mu^\alpha \cap \partial\Omega_\mu^j$, points of the centreline of the bar. Again, the above considerations justify in our Network model the adoption of expression (26) recalled here below

$$\mathbf{u}_\mu^\alpha(s) = \left(1 - \frac{s}{L_\alpha}\right)\mathbf{u}_\mu(\bar{\mathbf{y}}_{i_\alpha}) + \frac{s}{L_\alpha}\mathbf{u}_\mu(\bar{\mathbf{y}}_{j_\alpha}), \quad s \in [0, L_\alpha]. \tag{A.15}$$

By using HSJ.A2 and (37)

$$\begin{aligned}\mathbf{u}_\mu^\alpha(s) \approx \left(1 - \frac{s}{L_\alpha}\right)\mathbf{u}_\mu^{i_\alpha} + \frac{s}{L_\alpha}\mathbf{u}_\mu^{j_\alpha} = \\ \left(1 - \frac{s}{L_\alpha}\right)[\mathbf{u}|_{\mathbf{x}} + \mathbf{G}|_{\mathbf{x}}(\mathbf{y}_{i_\alpha} - \mathbf{y}_G) + \tilde{\mathbf{u}}_\mu^{i_\alpha}] + \\ \frac{s}{L_\alpha}[\mathbf{u}|_{\mathbf{x}} + \mathbf{G}|_{\mathbf{x}}(\mathbf{y}_{j_\alpha} - \mathbf{y}_G) + \tilde{\mathbf{u}}_\mu^{j_\alpha}], \ s \in [0, L_\alpha],\end{aligned} \tag{A.16}$$

where $\mathbf{y}_{i_\alpha}$ and $\mathbf{y}_{j_\alpha}$ are points characterising the nodes $i_\alpha, j_\alpha \in \mathcal{N}_{net}$, respectively. As a straightforward corollary of this assumption is that the non null part of $\nabla_{\mathbf{y}}\mathbf{u}_\mu$ in Ω_μ^α is given by $\frac{\mathrm{d}}{\mathrm{d}s}(\mathbf{u}_\mu^\alpha) \otimes \mathbf{a}^\alpha$, i.e.

$$\begin{aligned}\nabla_{\mathbf{y}}\mathbf{u}_\mu|_{\Omega_\mu^\alpha} = \frac{\mathrm{d}}{\mathrm{d}s}\mathbf{u}_\mu^\alpha(s) \otimes \mathbf{a}^\alpha = \\ \mathbf{G}|_{\mathbf{x}}\mathbf{a}^\alpha \otimes \mathbf{a}^\alpha + \frac{1}{L_\alpha}(\tilde{\mathbf{u}}_\mu^{j_\alpha} - \tilde{\mathbf{u}}_\mu^{i_\alpha}) \otimes \mathbf{a}^\alpha, \quad \alpha \in \mathcal{F}_{net}.\end{aligned} \tag{A.17}$$

A.2.1. Discrete version of displacement homogenisation formula

Now, let us investigate the impact of the HSJ.A1 in the expression of the homogenisation of displacement field given by (A.5) and its consequences, (A.6) and (A.7), due to the admissibility kinematical constraints. In the case of

(A.5) it is obtained

$$\mathbf{u}|_{\mathbf{x}} = \frac{1}{|\Omega^s_\mu|}\int_{\Omega^s_\mu}\mathbf{u}_\mu \mathrm{d}V_\mu = \frac{1}{|\Omega^s_\mu|}\Bigg(\sum_{\alpha\in\mathcal{F}_{net}}\int_{\Omega^\alpha_\mu}\mathbf{u}_\mu\,\mathrm{d}V_\mu + \sum_{i\in\mathcal{N}_{net}}\int_{\Omega^i_\mu}\mathbf{u}_\mu\,\mathrm{d}V_\mu\Bigg)$$
$$\approx \frac{1}{|\mathcal{F}_{net}|}\sum_{\alpha\in\mathcal{F}_{net}}\int_{\Omega^\alpha_\mu}\mathbf{u}_\mu\,\mathrm{d}V_\mu. \tag{A.18}$$

The result above leads to specialised versions of (A.6) and (A.7) respectively

$$\mathbf{y}_G = \frac{1}{|\mathcal{F}_{net}|}\sum_{\alpha\in\mathcal{F}_{net}}\int_{\Omega^\alpha_\mu}\mathbf{y}\,\mathrm{d}V_\mu, \qquad \frac{1}{|\mathcal{F}_{net}|}\sum_{\alpha\in\mathcal{F}_{net}}\int_{\Omega^\alpha_\mu}\tilde{\mathbf{u}}_\mu\,\mathrm{d}V_\mu = \mathbf{0}. \tag{A.19}$$

The above expressions can be further simplified by using the HT. Using (A.16) into (A.18) and formulas in (A.19) we have respectively

$$\begin{aligned}
\mathbf{u}|_{\mathbf{x}} &= \frac{1}{|\mathcal{F}_{net}|}\sum_{\alpha\in\mathcal{F}_{net}}\frac{V_\alpha}{2}(\mathbf{u}^{i_\alpha}_\mu + \mathbf{u}^{j_\alpha}_\mu),\\
\mathbf{y}_G &= \frac{1}{|\mathcal{F}_{net}|}\sum_{\alpha\in\mathcal{F}_{net}}\frac{V_\alpha}{2}(\mathbf{y}_{i_\alpha} + \mathbf{y}_{j_\alpha}),\\
&\frac{1}{|\mathcal{F}_{net}|}\sum_{\alpha\in\mathcal{F}_{net}}\frac{V_\alpha}{2}(\tilde{\mathbf{u}}^{i_\alpha}_\mu + \tilde{\mathbf{u}}^{j_\alpha}_\mu) = \mathbf{0},
\end{aligned} \tag{A.20}$$

which have been postulated in (43), and derived in (46) and (49) respectively.

A.2.2. *Discrete version of gradient homogenisation formula*

We will now investigate the impact of the HSJ.A1 in the expression of the homogenisation of the gradient field given by (A.8). Firstly, working with the first two integrals of (A.8) we have

$$\begin{aligned}
&\int_{\Omega^s_\mu}\nabla_{\mathbf{y}}\mathbf{u}_\mu\,\mathrm{d}V_\mu - \int_{\partial\Omega^{s,v}_\mu}\tilde{\mathbf{u}}_\mu\otimes\mathbf{n}\,\mathrm{d}S_\mu =\\
&\sum_{i\in\mathcal{N}_{net}}\Bigg(\int_{\Omega^i_\mu}\nabla_{\mathbf{y}}\mathbf{u}_\mu\,\mathrm{d}V_\mu - \int_{\partial\Omega^{i,v}_\mu}\tilde{\mathbf{u}}_\mu\otimes\mathbf{n}\,\mathrm{d}S_\mu\Bigg)\\
&+\sum_{\alpha\in\mathcal{F}_{net}}\Bigg(\int_{\Omega^\alpha_\mu}\nabla_{\mathbf{y}}\mathbf{u}_\mu\,\mathrm{d}V_\mu - \int_{\partial\Omega^{\alpha,v}_\mu}\tilde{\mathbf{u}}_\mu\otimes\mathbf{n}\,\mathrm{d}S_\mu\Bigg)\\
&\approx\sum_{i\in\mathcal{N}_{net}}\Bigg(\int_{\partial\Omega^{i,F}_\mu}\tilde{\mathbf{u}}_\mu\otimes\mathbf{n}\,\mathrm{d}S_\mu + \int_{\partial\Omega^{i,b}_\mu}\tilde{\mathbf{u}}_\mu\otimes\mathbf{n}\,\mathrm{d}S_\mu\Bigg) +\\
&+\sum_{\alpha\in\mathcal{F}_{net}}\Bigg(\int_{\Omega^\alpha_\mu}\nabla_{\mathbf{y}}\mathbf{u}_\mu\,\mathrm{d}V_\mu - \int_{\partial\Omega^{\alpha,v}_\mu}\tilde{\mathbf{u}}_\mu\otimes\mathbf{n}\,\mathrm{d}S_\mu\Bigg).
\end{aligned} \tag{A.21}$$

The expression above in (A.21) can be still rephrased by taking into account HSJ.A2 yielding

$$\begin{aligned}
&\sum_{i\in\mathcal{N}_{net}}\Bigg(\int_{\partial\Omega^{i,F}_\mu}\tilde{\mathbf{u}}^i_\mu\otimes\mathbf{n}\,\mathrm{d}S_\mu + \int_{\partial\Omega^{i,b}_\mu}\tilde{\mathbf{u}}^i_\mu\otimes\mathbf{n}\,\mathrm{d}S_\mu\Bigg) +\\
&+\sum_{\alpha\in\mathcal{F}_{net}}\Bigg(\int_{\Omega^\alpha_\mu}\nabla_{\mathbf{y}}\mathbf{u}_\mu\,\mathrm{d}V_\mu - \int_{\partial\Omega^{\alpha,v}_\mu}\tilde{\mathbf{u}}_\mu\otimes\mathbf{n}\,\mathrm{d}S_\mu\Bigg).
\end{aligned} \tag{A.22}$$

Now, introducing HT and (A.17) into (A.22) and recalling the definitions of *fibre-node brackets* (see (17)) and *equivalent boundary area* and *normal* (see (22) and (23) and text therein) we obtain

$$-\sum_{i\in\mathcal{N}_{net}}\Bigg(\sum_{\alpha\in\mathcal{F}^i_{net}}[\alpha,i]A_\alpha\tilde{\mathbf{u}}^i_\mu\otimes\mathbf{a}^\alpha\Bigg) + \sum_{i\in\mathcal{N}^\Gamma_{net}}\bar{A}_i\tilde{\mathbf{u}}^i_\mu\otimes\mathbf{n}^i$$

$$+\sum_{\alpha\in\mathcal{F}_{net}} V_\alpha\left(\mathbf{G}|_{\mathbf{x}}\mathbf{a}^\alpha\otimes\mathbf{a}^\alpha+\frac{1}{L_\alpha}(\tilde{\mathbf{u}}_\mu^{j_\alpha}-\tilde{\mathbf{u}}_\mu^{i_\alpha})\otimes\mathbf{a}^\alpha\right)=$$
$$\sum_{i\in\mathcal{N}_{net}}\mathbf{G}_\mu^i+\sum_{\alpha\in\mathcal{F}_{net}} V_\alpha\mathbf{G}_\mu^\alpha, \tag{A.23}$$

where the previously defined expressions for generalised *N-gradient* and *F-gradient* (recall (40) and (42) respectively) have been used to shorten notation.

Now let us simplify the third integral in (A.8). Using HSJ.A2 we have.[17]

$$\int_{\partial\Omega_\mu^{s,b}}\tilde{\mathbf{u}}_\mu\otimes\bar{\mathbf{n}}\,\mathrm{d}S_\mu=\sum_{i\in\mathcal{N}_{net}^\Gamma}\int_{\Omega_\mu^{i,b}}\tilde{\mathbf{u}}_\mu\otimes\bar{\mathbf{n}}\,\mathrm{d}S_\mu\approx\sum_{i\in\mathcal{N}_{net}^\Gamma}\bar{A}^i\tilde{\mathbf{u}}_\mu^i\otimes\bar{\mathbf{n}}. \tag{A.24}$$

Finally, replacing (A.23) and (A.24) in (A.8), noticing that $|\Omega_\mu^s|\approx|\mathcal{F}_{net}|$ by HSJ.A1 and post-multiplying by $\mathbf{B}^{-1}$ (recall definition in (55)) we have

$$\mathbf{G}|_{\mathbf{x}}=\frac{1}{|\mathcal{F}_{net}|}\left(\sum_{i\in\mathcal{N}_{net}}\mathbf{G}_\mu^i+\sum_{\alpha\in\mathcal{F}_{net}}V_\alpha\mathbf{G}_\mu^\alpha-\sum_{i\in\mathcal{N}_{net}^\Gamma}\bar{A}_i\tilde{\mathbf{u}}_\mu^i\otimes\bar{\mathbf{n}}\right)\mathbf{B}^{-1}, \tag{A.25}$$

which is the formula postulated in (51), now justified. Note that $\mathbf{B}^{-1}$, originally not present in (A.8), is necessary in order to enable the homogenisation formula to recover the macro-scale gradient for zero fluctuations. The need for its inclusion lies in the approximations explained in this section.

A.2.3. Comment on equivalent areas of boundary nodes

Finally, the boundary areas are computed by projecting the fibre areas arriving at a certain node over the corresponding normal vector. For example, for the case of Fig. A.25(a) we have just one boundary surface, then

$$\bar{A}_{i,1}=|\mathbf{n}_{i,1}\cdot\mathbf{a}|A+|\mathbf{n}_{i,1}\cdot\mathbf{a}'|A', \tag{A.26}$$

where A and A' are the areas related to the fibres with unit vector $\mathbf{a}$ and $\mathbf{a}'$, respectively. For the case of Fig. A.25(a) we have two boundary surfaces, then

$$\bar{A}_{j,1}=|\mathbf{n}_{j,1}\cdot\mathbf{a}^*|A^*, \tag{A.27}$$
$$\bar{A}_{j,2}=|\mathbf{n}_{j,2}\cdot\mathbf{a}^*|A^*, \tag{A.28}$$

where A^* is the area associated to fibre whose unit vector is $\mathbf{a}^*$. These ideas are of easy generalisation as defined in (21). Equivalent areas and normals are obtained using (22) and (23), respectively. In the case of Fig. A.25(a), these expressions trivially lead to $\bar{A}_i=\bar{A}_{i,1}$ and $\mathbf{n}_i=\mathbf{n}_{i,1}$. For the case of Fig. A.25(b), it is easy to verify that $\bar{A}_j=A^*$ and $\mathbf{n}_j=-\mathbf{a}^*$.

Appendix B. Proofs of the restrictions above the operators

In the original paper [30] it was seen that the functional form of the insertion, deformation and homogenisation operators can be arbitrarily defined provided they keep some relation between them. These relations were emphasised during the text, but in some cases the proof was skipped. This section aims to present the rigorous justifications (not necessarily proofs) for all necessary relations between operators proposed in this work, confirming that the formulation proposed is consistent with abstract framework constructed in [30].

First, consider the operators $\mathcal{J}_\mu^{\mathscr{U}}$, $\mathcal{J}_\mu^{\mathscr{E}}$, $\mathcal{D}_\mu$, $\mathcal{H}_\mu^{\mathscr{U}}$, $\mathcal{H}_\mu^{\mathscr{E}}$ as defined in (30), (33), (39), (43) and (50), respectively. Given $\mathbf{u}|_{\mathbf{x}}\in\mathbb{R}^{\mathrm{n_d}}$, $\mathbf{G}|_{\mathbf{x}}\in\mathbb{R}^{\mathrm{n_d}\times\mathrm{n_d}}$ and $\tilde{\mathbb{U}}_\mu\in\tilde{\mathscr{U}}_\mu$ the following relations are satisfied

1. $\mathcal{D}_\mu(\mathcal{J}_\mu^{\mathscr{U}}(\mathbf{u}|_{\mathbf{x}}))=\mathbf{O}$.
2. $\mathcal{H}_\mu^{\mathscr{U}}(\mathcal{J}_\mu^{\mathscr{U}}(\mathbf{u}|_{\mathbf{x}}))=\mathbf{u}|_{\mathbf{x}}$.
3. $\mathcal{H}_\mu^{\mathscr{E}}(\mathcal{D}_\mu(\mathcal{J}_\mu^{\mathscr{E}}(\mathbf{G}|_{\mathbf{x}})))=\mathbf{G}|_{\mathbf{x}}$.
4. $\mathcal{H}_\mu^{\mathscr{U}}(\mathcal{J}_\mu^{\mathscr{E}}(\mathbf{G}|_{\mathbf{x}}))=\mathbf{0}$.

[17] Naturally, consider the discrete definition for $\bar{\mathbf{n}}$ (in (59)) instead of the original one in the continuum as in (A.10).

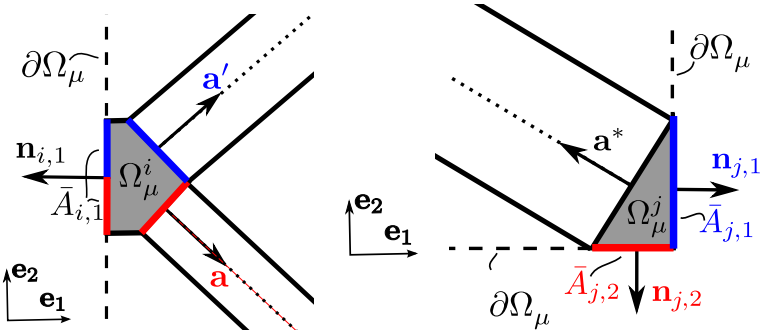

(a) On an RVE side. (b) At an RVE corner.

Fig. A.25. Typical joints reaching the RVE boundary.

5. $\mathcal{H}^{\mathscr{U}}_\mu(\tilde{\mathbb{U}}_\mu) = \mathbf{0}$.
6. $\mathcal{H}^{\mathscr{E}}_\mu(\mathcal{D}_\mu(\tilde{\mathbb{U}}_\mu)) = \mathbf{O}$.

Below, the proofs for these propositions follow.

Proof.

1. From the definitions of the operators, for any $\alpha \in \mathcal{F}_{net}$ we have
$$\big[\mathcal{D}_\mu(\mathcal{J}^{\mathscr{U}}_\mu(\mathbf{u}|_{\mathbf{x}}))\big]^\alpha = \frac{1}{L_\alpha}\Delta^\alpha \mathcal{J}^{\mathscr{U}}_\mu(\mathbf{u}|_{\mathbf{x}}) \otimes \mathbf{a}^\alpha = \frac{1}{L_\alpha}(\mathbf{u}|_{\mathbf{x}} - \mathbf{u}|_{\mathbf{x}}) \otimes \mathbf{a}^\alpha = \mathbf{O}.$$
Recalling that joint gradients only depend on the fluctuations, for any $i \in \mathcal{N}_{net}$ we have
$$\big[\mathcal{D}_\mu(\mathcal{J}^{\mathscr{U}}_\mu(\mathbf{u}|_{\mathbf{x}}))\big]^i = \mathbf{O}.$$
Finally we conclude that $\mathcal{D}_\mu(\mathcal{J}^{\mathscr{U}}_\mu(\mathbf{u}|_{\mathbf{x}})) = \mathbf{O}$.
2. Take
$$\mathcal{H}^{\mathscr{U}}_\mu(\mathcal{J}^{\mathscr{U}}_\mu(\mathbf{u}|_{\mathbf{x}})) = \frac{1}{|\mathcal{F}_{net}|}\sum_{\alpha\in\mathcal{F}_{net}} \frac{V_\alpha}{2}([\mathcal{J}^{\mathscr{U}}_\mu(\mathbf{u}|_{\mathbf{x}})]^{i_\alpha} + [\mathcal{J}^{\mathscr{U}}_\mu(\mathbf{u}|_{\mathbf{x}})]^{j_\alpha}) =$$
$$\frac{1}{|\mathcal{F}_{net}|}\sum_{\alpha\in\mathcal{F}_{net}} \frac{V_\alpha}{2}(\mathbf{u}|_{\mathbf{x}} + \mathbf{u}|_{\mathbf{x}}) = \frac{1}{|\mathcal{F}_{net}|}\Big(\sum_{\alpha\in\mathcal{F}_{net}} V_\alpha\Big)\mathbf{u}|_{\mathbf{x}} = \mathbf{u}|_{\mathbf{x}},$$
so, the result follows.
3. First recalling that joint gradients only depend on the fluctuations we have
$$\mathcal{H}^{\mathscr{E}}_\mu(\mathcal{D}_\mu(\mathcal{J}^{\mathscr{E}}_\mu(\mathbf{G}|_{\mathbf{x}}))) = \frac{1}{|\mathcal{F}_{net}|}\Big(\sum_{\alpha\in\mathcal{F}_{net}} V_\alpha\big[\mathcal{D}_\mu(\mathcal{J}^{\mathscr{E}}_\mu(\mathbf{G}|_{\mathbf{x}}))\big]^\alpha\Big)\mathbf{B}^{-1} =$$
$$\frac{1}{|\mathcal{F}_{net}|}\Big(\sum_{\alpha\in\mathcal{F}_{net}} V_\alpha \mathbf{G}|_{\mathbf{x}}\mathbf{a}^\alpha \otimes \mathbf{a}^\alpha\Big)\mathbf{B}^{-1} =$$
$$\mathbf{G}|_{\mathbf{x}} \underbrace{\frac{1}{|\mathcal{F}_{net}|}\Big(\sum_{\alpha\in\mathcal{F}_{net}} V_\alpha \mathbf{a}^\alpha \otimes \mathbf{a}^\alpha\Big)}_{=\mathbf{B}\text{ from (55)}}\mathbf{B}^{-1} = \mathbf{G}|_{\mathbf{x}},$$
and the result is verified.
4. Take now
$$\mathcal{H}^{\mathscr{U}}_\mu(\mathcal{J}^{\mathscr{E}}_\mu(\mathbf{G}|_{\mathbf{x}})) = \frac{1}{|\mathcal{F}_{net}|}\sum_{\alpha\in\mathcal{F}_{net}} \frac{V_\alpha}{2}([\mathcal{J}^{\mathscr{E}}_\mu(\mathbf{G}|_{\mathbf{x}})]^{i_\alpha} + [\mathcal{J}^{\mathscr{E}}_\mu(\mathbf{G}|_{\mathbf{x}})]^{j_\alpha}) =$$

$$\frac{1}{|\mathcal{F}_{net}|}\sum_{\alpha\in\mathcal{F}_{net}}\frac{V_\alpha}{2}\mathbf{G}|_{\mathbf{x}}(\mathbf{y}_{i_\alpha}+\mathbf{y}_{j_\alpha}-2\mathbf{y}_G)=$$
$$\mathbf{G}|_{\mathbf{x}}\Bigg(\underbrace{\frac{1}{|\mathcal{F}_{net}|}\sum_{\alpha\in\mathcal{F}_{net}}\frac{V_\alpha}{2}(\mathbf{y}_{i_\alpha}+\mathbf{y}_{j_\alpha})}_{=\mathbf{y}_G \text{ from (46)}}-\frac{1}{|\mathcal{F}_{net}|}\Big(\sum_{\alpha\in\mathcal{F}_{net}}V_\alpha\Big)\mathbf{y}_G\Bigg)=\mathbf{0},$$

so the statement holds.

5. This restriction is directly taken into account in the definition of the space $\widetilde{\mathscr{U}}_\mu$ (see (64)).
6. Also, this restriction is also directly enforced in the space $\widetilde{\mathscr{U}}_\mu$. ■

References

[1] G. Holzapfel, R. Ogden, Constitutive modelling of arteries, Proc. R. Soc. Lond. Ser. A Math. Phys. Eng. Sci. 466 (2118) (2010) 1551–1597.
[2] G. Holzapfel, T. Gasser, R. Ogden, A new constitutive framework for arterial wall mechanics and a comparative study of material models, J. Elasticity 61 (1–3) (2000) 1–48.
[3] H. Weisbecker, M.J. Unterberger, G.A. Holzapfel, Constitutive modelling of arteries considering fibre recruitment and three-dimensional fibre distribution., J. R. Soc. Interface 12 (105) (2015) 20150111.
[4] T. Gasser, R. Ogden, G. Holzapfel, Hyperelastic modelling of arterial layers with distributed collagen fibre orientations, J. R. Soc. Interface 3 (6) (2006) 15–35.
[5] A. Robertson, P. Watton, Mechanobiology of the arterial wall, in: A. Kuznetsov, S. Becker (Eds.), Transport in Biological Media, Elsevier, 2013.
[6] A.M. Stein, D.A. Vader, D.A. Weitz, L.M. Sander, The micromechanics of three-dimensional collagen-i gels, Complexity 16 (4) (2011) 22–28.
[7] A. Kabla, L. Mahadevan, Nonlinear mechanics of soft fibrous networks, J. R. Soc. Interface 4 (12) (2007) 99–106.
[8] P.L. Chandran, V.H. Barocas, Deterministic material-based averaging theory model of collagen gel micromechanics, J. Biomech. Eng. 129 (2) (2007) 137–147.
[9] H. Hatami-Marbini, R.C. Picu, Effect of fiber orientation on the non-affine deformation of random fiber networks, Acta Mech. 205 (1–4) (2009) 77–84.
[10] R.H. Pritchard, Y.Y.S. Huang, E.M. Terentjev, Mechanics of biological networks: from the cell cytoskeleton to connective tissue, Soft Matter 10 (12) (2014) 1864–1884.
[11] D.C.D. Speirs, E.A. de Souza Neto, D. Peri, An approach to the mechanical constitutive modelling of arterial tissue based on homogenization and optimization, J. Biomech. 41 (12) (2008) 2673–2680.
[12] T. Stylianopoulos, V.H. Barocas, Modeling for the elastic mechanical behavior of arterial, J. Biomech. Eng. 129 (August) (2007) 611–618.
[13] T. Stylianopoulos, V.H. Barocas, Volume-averaging theory for the study of the mechanics of collagen networks, Comput. Methods Appl. Mech. Engrg. 196 (31–32) (2007) 2981–2990.
[14] J.R. Thunes, S. Pal, R.N. Fortunato, J.A. Phillippi, T.G. Gleason, D.A. Vorp, S. Maiti, A structural finite element model for lamellar unit of aortic media indicates heterogeneous stress field after collagen recruitment, J. Biomech. 49 (9) (2016) 1562–1569.
[15] J.R. Thunes, J.A. Phillippi, T.G. Gleason, D.A. Vorp, S. Maiti, Structural modeling reveals microstructure-strength relationship for human ascending thoracic aorta, J. Biomech. (2018) 1–10.
[16] A. Witthoft, A. Yazdani, Z. Peng, C. Bellini, J.D. Humphrey, G.E. Karniadakis, G.E. Karniadakis, A discrete mesoscopic particle model of the mechanics of a multi-constituent arterial wall, J. R. Soc. Interface (2016).
[17] K. Berkache, S. Deogekar, I. Goda, R.C. Picu, J.F. Ganghoffer, Construction of second gradient continuum models for random fibrous networks and analysis of size effects, Compos. Struct. 181 (2017) 347–357.
[18] K. El Nady, I. Goda, J.F. Ganghoffer, Computation of the effective nonlinear mechanical response of lattice materials considering geometrical nonlinearities, Comput. Mech. 58 (6) (2016) 957–979.
[19] K. El Nady, J.F. Ganghoffer, Computation of the effective mechanical response of biological networks accounting for large configuration changes, J. Mech. Behav. Biomed. Mater. 58 (2016) 28–44.
[20] D. Caillerie, A. Mourad, A. Raoult, Cell-to-muscle homogenization. application to a constitutive law for the myocardium, ESAIM Math. Model. Numer. Anal. 37 (4) (2003) 681–698.
[21] W.E. Warren, E. Byskov, Three-fold symmetry restrictions on two-dimensional micropolar materials, Eur. J. Mech. A Solids 21 (5) (2002) 779–792.
[22] A.S. Shahsavari, R.C. Picu, Size effect on mechanical behavior of random fiber networks, Int. J. Solids Struct. 50 (20–21) (2013) 3332–3338.
[23] C. Miehe, J. Dettmar, A framework for micro-macro transitions in periodic particle aggregates of granular materials, Comput. Methods Appl. Mech. Engrg. 193 (3–5) (2004) 225–256.
[24] C. Miehe, J. Dettmar, D. Zah, Homogenization and two-scale simulations of granular materials for different microstructural constraints, Internat. J. Numer. Methods Engrg. (2010) arXiv:1010.1724.
[25] D. Davydov, J.P. Pelteret, P. Steinmann, Comparison of several staggered atomistic-to-continuum concurrent coupling strategies, Comput. Methods Appl. Mech. Engrg. 277 (2014) 260–280.
[26] P. Steinmann, S. Ricker, E. Aifantis, Unconstrained and Cauchy-Born-constrained atomistic systems: Deformational and configurational mechanics, Arch. Appl. Mech. 81 (5) (2011) 669–684.

[27] X. Li, W. E, Multiscale modeling of the dynamics of solids at finite temperature, J. Mech. Phys. Solids 53 (7) (2005) 1650–1685.
[28] S. Li, S. Urata, An atomistic-to-continuum molecular dynamics: theory, algorithm, and applications, Comput. Methods Appl. Mech. Engrg. 306 (2016) 452–478.
[29] E. Bosco, R.H.J. Peerlings, B.A.G. Lomans, C.G. van der Sman, M.G.D. Geers, On the role of moisture in triggering out-of-plane displacement in paper: From the network level to the macroscopic scale, Int. J. Solids Struct. (2017).
[30] P.J. Blanco, P.J. Sánchez, E.A. de Souza Neto, R.A. Feijóo, Variational foundations and generalized unified theory of RVE-based multiscale models, Arch. Comput. Methods Eng. 23 (2016) 191–253.
[31] P.J. Blanco, P.J. Sánchez, E.A. de Souza Neto, R.A. Feijóo, Variational foundations of rve-based multiscale models, LNCC Research and Development Internal Report, 2014.
[32] P.L. Chandran, Affine versus non-affine fibril kinematics in collagen networks: theoretical studies of network behavior, J. Biomech. Eng. 128 (2) (2005) 259.
[33] L. Zhang, S.P. Lake, V.K. Lai, C.R. Picu, V.H. Barocas, M.S. Shephard, A coupled fiber-matrix model demonstrates highly inhomogeneous microstructural interactions in soft tissues under tensile load, J. Biomech. Eng. 135 (1) (2012) 011008.
[34] M.F. Hadi, V.H. Barocas, Microscale fiber network alignment affects macroscale failure behavior in simulated collagen tissue analogs., J. Biomech. Eng. 135 (2) (2013) 021026.
[35] C. Heussinger, E. Frey, Stiff polymers, foams, and fiber networks, Phys. Rev. Lett. 96 (1) (2006) 1–4.
[36] A.M. Stein, D.A. Vader, D.A. Weitz, L.M. Sander, An algorithm for extracting the network geometry of three-dimensional collagen gels, J. Microcospy 232 (May) (2008) 463–475.
[37] C.J. Cyron, K.W. Müller, A.R. Bausch, W.A. Wall, Micromechanical simulations of biopolymer networks with finite elements, J. Comput. Phys. 244 (2013) 236–251.
[38] C. Meier, M.J. Grill, W.A. Wall, A. Popp, Geometrically exact beam elements and smooth contact schemes for the modeling of fiber-based materials and structures, Int. J. Solids Struct. (2017) 1–23 arXiv:1611.06436.
[39] E. de Souza Neto, P. Blanco, P. Sánchez, R. Feijóo, An RVE-based mutiscale theory of solids with micro-scale inertia and body force effects, Mech. Mater. 80 (2015) 136–144.
[40] P. Blanco, P. Sánchez, E. De Souza Neto, R. Feijóo, The method of multiscale virtual power for the derivation of a second order mechanical model, Mech. Mater. 99 (2016) 53–67.
[41] P. Blanco, A. Clausse, R. Feijóo, Homogenization of the Navier-Stokes equations by means of the Multi-scale Virtual Power Principle, Comput. Methods Appl. Mech. Engrg. 315 (2017) 760–779.
[42] P.J. Blanco, S.M. Giusti, Thermomechanical multiscale constitutive modeling: Accounting for microstructural thermal effects, J. Elasticity 115 (1) (2014) 27–46.
[43] P. Sánchez, P. Blanco, A. Huespe, R. Feijóo, Failure-oriented multi-scale variational formulation: micro-structures with nucleation and evolution of softening bands, Comput. Methods Appl. Mech. Engrg. 257 (2013) 221–247.
[44] S. Toro, P.J. Sánchez, A.E. Huespe, S.M. Giusti, P.J. Blanco, R.A. Feijóo, A two-scale failure model for heterogeneous materials : numerical implementation based on the finite element method, Internat. J. Numer. Methods Engrg. 97 (2014) 313–351.
[45] S. Toro, P. Sánchez, P. Blanco, E. de Souza Neto, A. Huespe, R. Feijóo, Multiscale formulation for material failure accounting for cohesive cracks at the macro and micro scales, Int. J. Plast. 76 (2016) 75–110.
[46] S. Toro, P.J. Sánchez, J.M. Podestá, P.J. Blanco, A.E. Huespe, R.A. Feijóo, Cohesive surface model for fracture based on a two-scale formulation: computational implementation aspects, Comput. Mech. 58 (4) (2016) 549–585.
[47] R. Hill, A self-consistent mechanics of composite materials, J. Mech. Phys. Solids 13 (4) (1965) 213–222.
[48] J. Mandel, Plasticité Classique Et Viscoplasticité, Springer-Verlag, 1972.
[49] P. Wriggers, Nonlinear Finite Element Methods, Springer-Verlag, Berlin, 2008.
[50] R. De Vita, Structural Constitutive Models for Knee Ligaments, University of Pittsburgh, 2005, p. 73.
[51] D. Balzani, S. Brinkhues, G.A. Holzapfel, Constitutive framework for the modeling of damage in collagenous soft tissues with application to arterial walls, Comput. Methods Appl. Mech. Engrg. 213–216 (2012) 139–151.
[52] F.M. Davis, R. De Vita, A nonlinear constitutive model for stress relaxation in ligaments and tendons, Ann. Biomed. Eng. 40 (12) (2012) 2541–2550.
[53] K. Li, R.W. Ogden, G.A. Holzapfel, Computational method for excluding fibers under compression in modeling soft fibrous solids, Eur. J. Mech. A Solids 57 (May) (2016) 178–193.
[54] M. Comninou, I.V. Yannas, Dependence of stress-strain nonlinearity of connective tissues on the geometry of collagen fibres, J. Biomech. 9 (7) (1976) 427–433.
[55] M. DeGroot, M. Schervish, Probability and Statistics, Addison-Wesley, 2012.
[56] M. Hill, X. Duan, G. Gibson, S. Watkins, A. Robertson, A theoretical and non-destructive experimental approach for direct inclusion of measured collagen orientation and recruitment into mechanical models of the artery wall, J. Biomech. 45 (5) (2012) 762–771.
[57] C.H. Rycroft, VORO++: A three-dimensional Voronoi cell library in C++, Chaos 19 (4) (2009) 1–16.
[58] S. Forest, D.K. Trinh, Generalized continua and non-homogeneous boundary conditions in homogenisation methods, Z. Angew. Math. Mech. 91 (2) (2011) 90–109.
[59] D.K. Trinh, R. Janicke, N. Auffray, S. Diebels, S. Forest, Evaluation of generalized continuum substitution models for heterogeneous materials, Int. J. Multiscale Comput. Eng. 10 (6) (2012) 527–549.
[60] T. Kanit, S. Forest, I. Galliet, V. Mounoury, D. Jeulin, Determination of the size of the representative volume element for random composites: statistical and numerical approach, Int. J. Solids Struct. 40 (13) (2003) 3647–3679.
[61] J. Oliver, M. Caicedo, A.E. Huespe, J.A. Hernandez, E. Roubin, Reduced order modeling strategies for computational multiscale fracture, Comput. Methods Appl. Mech. Engrg. 313 (2017) 560–595.

[62] D. Li, A.M. Robertson, A structural multi-mechanism constitutive equation for cerebral arterial tissue, Int. J. Solids Struct. 46 (14–15) (2009) 2920–2928.
[63] N. Ohno, K. Ikenoya, D. Okumura, T. Matsuda, Homogenized elastic-viscoplastic behavior of anisotropic open-porous bodies with pore pressure, Int. J. Solids Struct. 49 (19–20) (2012) 2799–2806.
[64] J.C. Michel, H. Moulinec, P. Suquet, Effective properties of composite materials with periodic microstructure: a computational approach, Comput. Methods Appl. Mech. Engrg. 172 (14) (1999) 109–143.